WL-TR-96-4020

CERAMIC BEARING TECHNOLOGY PROGRAM

VOLUME 1   FINAL REPORT

R. KOMANDURI   J. LANGE

J. WICKSTED   J. KRASINSKI

OKLAHOMA STATE UNIVERSITY

STILLWATER OK

JULY 1995

FINAL REPORT FOR 08/01/92 - 07/01/95

APPROVED FOR PUBLIC RELEASE; DISTRIBUTION IS UNLIMITED.

19961028 028

MATERIALS DIRECTORATE

WRIGHT LABORATORY

AIR FORCE MATERIAL COMMAND

WRIGHT PATTERSON AFB 0H 45433-7734

NOTICE

When government drawings, specifications, or other data are used for any purpose other than in connection with a definitely related government procurement operation, the United States Government thereby incurs no responsibility nor any obligation whatsoever; and the fact that the government may have formulated, furnished, or in any way supplied the said drawings, specifications, or other data, is not to be regarded by implication or otherwise as in any manner licensing the holder or any other person or corporation, or conveying any rights or permission to manufacture, use, or sell any patented invention that may in any way be related thereto.

This report is releasable to the National Technical Information Service (NTIS). At NTIS, it will be available to the general public, including foreign nations.
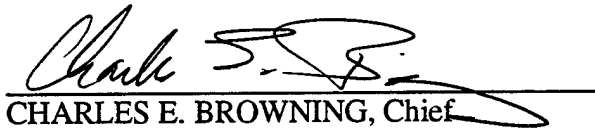
This technical report has been reviewed and is approved for publication.

KARL R. MECKLENBURG, Project Engineer
Nonstructural Materials Branch
Nonmetallic Materials Division

KENT J. EISENTRAUT, Chief
Nonstructural Materials Branch
Nonmetallic Materials Division

CHARLES E. BROWNING, Chief
Nonmetallic Materials Division
Materials Directorate

If your address has changed, if you wish to be removed from our mailing list, or if the addressee is no longer employed by your organization, please notify WL/MLBT, Bldg 654, 2941 P Street, Suite 1, Wright-Patterson AFB OH 45433-7750 to help maintain a current mailing list.

Copies of this report should not be returned unless return is required by security considerations, contractual obligations, or notice on a specific document.

DISCLAIMER NOTICE

THIS DOCUMENT IS BEST
QUALITY AVAILABLE. THE
COPY FURNISHED TO DTIC
CONTAINED A SIGNIFICANT
NUMBER OF PAGES WHICH DO
NOT REPRODUCE LEGIBLY.

REPORT DOCUMENTATION PAGE

Form Approved
OMB No. 0704-0188

1. AGENCY USE ONLY (Leave blank)	2. REPORT DATE JUL 1995	3. REPORT TYPE AND DATES COVERED Final Report 08/01/92--07/01/95

4. TITLE AND SUBTITLE CERAMIC BEARING TECHNOLOGY PROGRAM

VOL 1   Final Report

5. FUNDING NUMBERS
C F33615-92-C-5933
PE 62712
PR 8355
TA 00
WU 10

6. AUTHOR(S) R. KOMANDURI   J. LANGE
J. WICKSTED   J. KRASINSKI

7. PERFORMING ORGANIZATION NAME(S) AND ADDRESS(ES)

OKLAHOMA STATE UNIVERSITY
STILLWATER OK

8. PERFORMING ORGANIZATION REPORT NUMBER

9. SPONSORING / MONITORING AGENCY NAME(S) AND ADDRESS(ES)

MATERIALS DIRECTORATE
WRIGHT LABORATORY
AIR FORCE MATERIEL COMMAND
WRIGHT PATTERSON AFB OH 45433-7734

10. SPONSORING / MONITORING AGENCY REPORT NUMBER

WL-TR-96-4020

11. SUPPLEMENTARY NOTES

12a. DISTRIBUTION / AVAILABILITY STATEMENT

APPROVED FOR PUBLIC RELEASE; DISTRIBUTION IS UNLIMITED.

12b. DISTRIBUTION CODE

13. ABSTRACT (Maximum 200 words) This project deals with the development of advanced manufacturing technologies for finishing silicon nitride balls and rollers for bearing applications and non-destructive inspection (NDI) methods for assessing surface damage of ceramic materials and to correlate the surface properties with tribological performance. Magnetic field assisted polishing was used for finishing the balls and magnetic abrasive finishing for finishing rollers (Komanduri). By applying low levels of controlled force (1 N/ball or less) the damage to the finished surface is expected to be minimal. Also chemo-mechanical polishing was used to minimize the brittle fracture. Using these techniques the polishing time was reduced from some 10- 20 weeks to about 20 hours. The finish obtained was about 5-10 nm and the sphericity in the range of 0.5 -1 μm. The non-destructive inspection (NDI) techniques used include Raman spectroscopy and radio frequency absorption (Lange), Brillouin scattering (Wicksted), and photoacoustic methods (Krasinski)] to detect surface damage. Inelastic Raman Light Scattering technique was found to be a rapid, non-contact method for characterizing the physical properties of the near-surface ($\sim$ 2 μm) ceramic material in bearing balls. A number of features of the Raman spectra were demonstrated to be related to properties of the ceramic which are pertinent to the performance of the bearing balls.

14. SUBJECT TERMS Silicon nitride, balls and rollers, finishing, bearings, NDI methods, magnetic field assisted polishing, Raman spectroscopy, radio frequency absorption, Brillouin scattering, photoacoustic techniques.

15. NUMBER OF PAGES 169

16. PRICE CODE

17. SECURITY CLASSIFICATION OF REPORT UNCLASSIFIED	18. SECURITY CLASSIFICATION OF THIS PAGE UNCLASSIFIED	19. SECURITY CLASSIFICATION OF ABSTRACT UNCLASSIFIED	20. LIMITATION OF ABSTRACT SAR

NSN 7540-01-280-5500

Standard Form 298 (Rev. 2-89)
Prescribed by ANSI Std. Z39-18
298-102

Table of Contents

List of Figures

List of Tables

1. EXECUTIVE SUMMARY

In 1993, ARPA announced an innovative program (BAA #91:11) on Ceramic Bearing Technology to enhance the processing technology base for high quality ceramic ball and rolling elements for bearing applications. Ceramic bearings were considered to offer significant improvements in performance and durability for a wide variety of military applications ranging from inertial guidance instruments and precision gimbals to turbine engine exhaust nozzle actuators and submarine pumps. Two principal barriers considered for the greater use of ceramic bearings by DoD were their high cost and lack of operational reliability. Manufacturing cost of the product is high due to long processing times and high rejection rates. The high rejection rates at the finished component level were attributed to the inherent variability in the process (grinding and finishing) for producing ball and rolling elements and lack of reliable, non-destructive inspection (NDI) methods in the prefired green blank, densified blank, and finished bearing component stages. Reliability issues included the need for realistic life and performance. The overall goal of the ARPA Ceramic Bearing Technology Program was to enhance the industrial technology base capabilities for ceramic-hybrid and all ceramic bearings for use in advanced DoD systems through innovative research efforts for developing and introducing advanced processing and process control technologies to ceramic fabricators and bearing manufacturers.

To address some of these issues, Oklahoma State University (OSU) proposed the development of advanced manufacturing technologies for finishing silicon nitride balls and rollers for bearing applications and non-destructive inspection (NDI) methods. The objectives of the OSU program were the following: (i) the development of improved manufacturing technologies (grinding and polishing) for finishing silicon nitride ceramic materials (for ball and roller elements for bearing applications) (Dr. R. Komanduri) and (ii) research and development studies on non-destructive inspection (NDI) techniques [Raman spectroscopy (Dr. J. Lange), radio frequency absorption (Dr. J. Lange), Brillouin scattering (Dr. J. Wicksted), and photoacoustic methods (Dr. J. Krasinski)] to detect surface damage during processing. This Executive Summary is Part 1 of the ARPA Ceramic Bearing

Technology Program at OSU. Parts 2 - 5 is the Final Report that presents various aspects of the program including the advanced manufacturing processes and non-destructive inspection (NDI) methods. Volume II includes the Appendices giving details of the various aspects of advanced manufacturing processes investigated under this and related programs.

Under advanced manufacturing technologies, 'gentle' grinding and magnetic field assisted polishing techniques were proposed for development so that a reduction in the damage to the ground and polished surfaces can be obtained during manufacturing. This can be accomplished by controlling the level of force applied to the work material by the abrasive. For example, the low level of controlled force (1 N/ball or less) and high rotational speed of the spindle (up to 10,000 rpm) should enable rapid finishing of the balls (2 or 3 days instead of several weeks with the conventional methods) with minimal surface and near surface defects. Also, the float polishing apparatus enables polishing of small batches of ceramic balls which will be ideal in cases where only a small batch is needed or in the R & D environment where different materials under development need to be investigated for specific applications.

Non-destructive inspection methodologies proposed were to determine optimal techniques for assessing surface damage of ceramic materials and to correlate the surface properties with tribological performance. The inspection methodology should reveal fundamental surface properties as well as provide a means to evaluate the grinding and polishing technologies in a way that is cost effective and timely for the production of improved ceramic balls and rollers for bearing applications.

1.1 ADVANCED MANUFACTURING TECHNOLOGIES

1.1.1 Magnetic Field Assisted Polishing (R. Komanduri)

Under advanced manufacturing technologies for finishing of Si_3N_4 ceramic balls and rollers, we initially concentrated on 'gentle' grinding [using the Rank-Pneumo submicron diamond turning and grinding machine (ASG 3200)] for finishing the rollers and magnetic float polishing for the balls.

However, as we had difficulty in recruiting suitable graduate students and/or technical staff with skills necessary for the conduct of 'gentle' grinding work, we sought the Program Manager K. R. Mecklenburg's permission to work on magnetic field assisted polishing techniques instead of 'gentle' grinding for finishing Si3N4 rollers. The techniques selected for finishing of ceramic rollers were magnetic abrasive finishing and magnetic float polishing.

Soon after the initiation of the project, we reviewed the literature on magnetic field assisted polishing. It covered extensive work done by the researchers from the former U.S.S.R. and East European countries (chiefly, Bulgaria) and by the Japanese researchers [chiefly, Prof. Shinmura and his group at Utsunomia University and Prof. Kato and Dr. Umehara and their group at Tohoku University]. We exchanged several visits to discuss research of mutual interest. One of the researchers from Japan, Dr.Umehara, spent a year on sabbatical at OSU to conduct research in this area. Another researcher, Dr.Shinmura, spent several brief periods at OSU on this project. Reference 21 provides details of the literature review. Based on the review of literature and discussions, we have formulated the research methodology that was used as a base over the past 3 years. Similarly, we made an extensive review of the literature on the magnetic fluids, including patent literature. Reference 18 provides details of this review.

We used the finite element method (FEM) (ANSYS program) for magnetic fields and applied it to the design of the apparatus for magnetic field assisted polishing. We used this program to design the magnetic heads for magnetic abrasive finishing, to design the equipment for magnetic float polishing of balls using permanent magnets and an electromagnet, and to determine the buoyancy force and the stiffness of the magnetic float polishing apparatus. Details of these are covered in References 1, 7, and 16.

We designed and built two apparatus for magnetic float polishing of silicon nitride balls - one using permanent magnets [14,16, 20] and the other using an electromagnet [7]. The apparatus can be used either with the spindle of the Bridgeport CNC milling machine (up to 6000 rpm) or with the PI (Professional Instruments Inc.) high speed (up to 10,000 rpm), high precision air bearing spindle. We conducted parametric studies to relate process

3

parameters, such as magnetic field strength and gradient, spindle speed, abrasive used (material, grain size, and concentration) with the polishing rate and surface finish. We finished five sets of 12 balls each of 1/2 in silicon nitride balls. We achieved surface finish (Ra) in the range of 20 to 30 nm and sphericity in the range of 0.3 to 0.9 μm for these balls [17]. They will be delivered to the WPAFB for further evaluation. We also built a new float polishing apparatus for finishing smaller size (1/4 in) balls. We are currently completing two sets of 24 balls.

We obtained HIPed Si_3N_4 balls with a nominal diameter of 13.4 mm from CERBEC (NBD 200) for finishing into 1/2 in balls. Unfortunately, these balls, in addition to being significantly larger, also contained a 200 μm thick x 5 mm wide band of silicon nitride material around the parting line in the HIPing process. Initially we were not sure if our apparatus could remove such non-uniform surfaces. We found the magnetic float polishing apparatus to be capable of removing this band without much difficulty. It took about 2 hours to remove this ring around the balls. We also received some 50 CERBEC (NBD 100) balls (1/2 in diameter) for initial evaluation, courtesy of CERBEC. We want to thank CERBEC, in particular Dr. C. Burk, for his cooperation and support.

The electromagnet design of the magnetic float polishing apparatus was based on Dr. Shinmura's previous experience with the electromagnet design for magnetic abrasive finishing. Since we had no basis to check it, we adopted this design and built the apparatus. However, we discovered that the equipment was inadequate in terms of magnetic field strength, stiffness, and magnetic buoyant force. It may be pointed out that this was before our involvement with the FEM analysis (ANSYS). Using ANSYS program, we were able to modify the apparatus significantly so that ceramic balls could be finished. During shakedown, we experienced another problem, namely, overheating of the magnetic fluid due to I^2R losses of the magnetic coil located just below the container in which polishing takes place. This resulted in the evaporation of the fluid and consequent solidification of the magnetic fluid. We have developed a cooling system which reduced this problem significantly. Details of the modifications and performance of this apparatus are given in Reference 7.

We found the sphericity and finish on the balls to depend on the magnitude of the force and stiffness of the system. Bearing faults have been detected in the past, on a routine basis, using vibration or sound level monitoring which is applied in industry where such monitoring is beneficial. Increased vibration/sound levels correspond to increased wear of the bearing or the case of a faulty bearing. Frequency domain analysis can be used to eliminate extraneous noise and identify the different modes of bearing failure. In this investigation, we used a similar technique based on sound measurements to monitor the polishing process. Initially, the balls being non-uniform in diameter and shape would give higher sound levels during polishing. With improvement in shape and size, the vibration level would decrease significantly. Using the PI high-speed, high-precision spindle, our initial results have indicated that the sphericity of the balls can be monitored using sound levels generated during polishing. We have detected initial sound levels to be around 93 dB when the sphericity was in the range of 200 μm. As the sphericity improved to about 0.5 μm, the sound level decreased to 68 dB. The background sound level was about 64 dB. Using this, it would be possible to monitor the improvement in sphericity with corresponding decrease in sound level or vibration. Load during the process can be similarly monitored. Also, the ball motion in the polishing chamber can be deduced by monitoring the ball circulation speed. Using the sound and force sensors, we are developing an on-line monitoring and control system for magnetic field assisted polishing. Details of the use of sound signals for monitoring sphericity are given in Reference 11.

For finishing Si_3N_4 rollers, we designed and built a magnetic abrasive finishing apparatus on a 1.5 hp Hardinge precision lathe (0-3,000 rpm) using an electromagnet magnet [1,8,9]. This apparatus was designed with the assistance of Dr. Shinmura of Utsunomia University, Japan. Initially, we conducted a parametric study on a non-magnetic stainless steel (as a model material for non-magnetic silicon nitride) to relate process parameters, such as magnetic field strength and gradient, spindle speed, abrasive used (material, grain size, and concentration) with the polishing rate and surface finish. We subsequently finished silicon nitride rollers to a surface finish (Ra) in the range of 5 to 10 nm. However, we were recently asked to finish the

rollers not only for finish but also for roundness and size for use as rolling contact fatigue (RCF) rods. We received four rollers [two CERCOM material and one each of Toshiba and CERBEC material] from MTI for this purpose. The latter two are intended for initial experimentation for straightness and roundness as they were undersize. We are currently automating axial motion of the lathe (feed direction) to obtain straightness and roundness. Once this modification is complete, we intend to finish the rods and deliver them to MTI for further evaluation.

For finishing Si_3N_4 rollers (eight HIP-Si_3N_4 rollers from Japan with a diameter of 19 mm and length of 26 mm), we modified the magnetic fluid grinding apparatus originally designed and built by Drs. Umehara and Kato of Tohoku University, Japan The apparatus is currently in use at OSU, was developed on the basis of the principle of magnetic buoyancy theory developed by Rosensweig. The original magnetic float polishing apparatus for finishing ceramic balls was also developed on the basis of this theory. We finished silicon nitride rollers by magnetic fluid grinding starting from the as-HIPed condition. Surface finish was improved from 1.6 μm to about 5 nm. Cylindricity was improved from 16.65 μm to 4.25 μm. The rollers finished by this technique provides slightly rounded edges with a minimum value of straightness of about 10 μm over the length of the roller. This feature seems to be a characteristic of the process, as it polishes both the face and the sides leading to rounded edges. This, however, may be considered as an advantage (not a limitation) with this process as most rollers for bearing applications have similar geometries imposed by the designer to prevent stress concentrations at the contact surface. So a secondary operation is normally required to provide this crown on the rollers. Using magnetic fluid grinding, this crowning can be accomplished in one step without the need for a secondary operation. Details of this process and test results are given in Reference 19.

We made fundamental contributions on the tribological interactions between the abrasive and the work material and the micro-mechanisms of material removal and surface generation process in finishing (surface roughness in the range of a few nanometers rms) of advanced ceramics and glasses. In developing plausible mechanisms, we made an attempt to clearly

6

delineate the failure mechanisms operable in polycrystalline ceramics and glasses versus the metals. This was necessary because of the significant differences in the nature of bonding, microstructure, tribochemistry, flaws generated during processing of these materials and their consequent effect on the associated failure mechanisms.

Since ceramics are processed from powders using sintering, hot-pressing, or hot-isostatic pressing, they possess less than theoretical density. This results in some inherent porosity in the microstructure. Also, the grain boundaries generally consist of a weak, glassy phase. All these factors affect the strength and failure (deformation/fracture) behavior of these materials. In this case, grain dislodgement, viscous flow at the grain boundaries, and microfracture of the crystals may be the predominant modes of failure rather than plastic deformation. Also, under the high pressures and temperatures generated at the contacting points during polishing, mechano-chemical effects can play an important role in the material removal. Details of this work are covered in References 6, 12, 13, and 22.

We made also significant contributions towards an understanding of the chemo-mechanical polishing of Si_3N_4 with Cr_2O_3 abrasive, which is an excellent abrasive for the polishing of silicon nitride work material. As the hardness of Cr_2O_3 is nearly the same as that of Si_3N_4, the mechanism of material removal is believed to be chemo-mechanical rather than mechanical abrasion [15]. However, no evidence of any compound formation of Si_3N_4 with Cr_2O_3 abrasive was reported in the literature. Consequently, the role of Cr_2O_3 was considered to be as one of a *catalyst*, in view of its well known role as a catalyst, rather than its direct involvement in the chemical reactions with Si_3N_4. We analyzed the wear debris and showed conclusively that Cr_2O_3 does participate in chemo-mechanical polishing of Si_3N_4 forming chromium nitride and chromium silicate. Details of this are given in References 2 and 3.

We also developed a new model of chemo-mechanical polishing of Si_3N_4 in *air* and in *water* environments with Cr_2O_3 abrasive. For the chemo-mechanical polishing *in air*, the possible reactions that can be formed include oxidation of Si_3N_4 to form a silica layer on the surface and the evolution of nitrogen gas. Other reaction products included the formation of

chromium nitride and chromium silicate. For polishing *in water*, the reactions were essentially the same except in this case, the adsorption of hydroxyl ions to the surface of Si_3N_4 and oxidation of the surface took place, which formed initially a silica layer which subsequently oxidized to form a hydrated silica ($SiOH_4$) layer. When the nitrogen ions get an opportunity to pair up with hydrogen ions present in water, they form ammonia gas (instead of nitrogen gas, as in the case of air). The other reaction products were the same, namely, chromium nitride and chromium silicate. The implication of gaseous reaction products in the generation of pore-free surface in finishing should be appreciated. Details of this work are given in References 2 and 4.

In the study of the chemical reaction products that may form in chemo-mechanical polishing, both flash temperatures and flash times have to be considered. While flash temperatures can be used as a basis for thermodynamic analysis (free energy of formation) for the feasibility of formation of a particular chemical reaction between the work material, abrasive, and the environment, the flash times are needed to investigate the kinetics. To address this problem, a thermal model was developed for the calculation of flash temperatures and flash times at the contact points in magnetic float polishing and magnetic abrasive finishing processes. The heat source at the contact area (i.e. between the ball and the shaft in the former case or between the abrasive and the roller in the later case), where much of the material removal takes place, was approximated to be a disc. Carlsaw and Jaeger's classical moving heat source theory was then applied to solve the circular ring heat source problem and finally the disc heat source problem. The flash temperatures, flash times, and temperature distribution between the balls and the shaft of the polishing apparatus were calculated using this technique. The mathematical analysis developed has enabled the calculation of flash times, which is not possible with the use of approximate solutions developed earlier. Details of the thermal model with application to magnetic float polishing are given in Reference 10. Application of the moving disc heat source model for the case of magnetic abrasive finishing (i.e. between the roller and the magnetic abrasive) is given in References 2 and 5.

1.2 NON-DESTRUCTIVE EVALUATION

1.2.1 Inelastic Raman Light Scattering (J. Lange)

A non-contract light scattering technique was developed to evaluate surface properties of silicon nitride bearing balls and relate this information to wear properties of the ceramic. The inelastic scattering from the vibrational states of the crystalline silicon nitride ceramic is known as Raman scattering. This technique yields a rapid, non-contact method of characterizing the physical properties of the near-surface (~ 2 μm) ceramic material in bearing balls. A number of features of the Raman spectra are demonstrated to be related to properties of the ceramic which are pertinent to the performance of the bearing balls. The physical properties determined by Raman scattering include internal strain, relative quantities of the low and the high temperature phase of silicon nitride, impurity compositions, and defects in crystalline structures of the ceramic. Internal strain of the ceramic determined by using the Raman light scattering technique correlates with rolling contact fatigue wear test results. The Raman technique also identifies local physical parameters, such as strain gradients which lead to chipping in wear tests, to be related to local damage.

The wide range of physical parameters detectable in silicon nitride ceramic by the Raman technique makes it well suited for production monitoring as well as a means of screening to reduce the probability of failure in bearing balls. Our development of computerized measurement and evaluation procedures allows timely evaluations of the bearing balls by relatively unskilled personnel. Further development of software and advanced measuring techniques is proceeding through a commercial concern. The objective is to develop non-destructive, non-contact imaging which evaluates the global physical properties of bearing balls in a rapid manner. This new information which is not available through visible inspection should become an important component for quality control. Details of this work are given in Reference 23.

1.2.2 Dielectric Properties of Silicon Nitride Ceramics (J. Lange)

The dielectric constant and losses of silicon nitride ceramics were measured over a wide frequency range. Measurements were made in the radio frequency range (100 MHz) and at microwave frequencies (10 GHz). Ceramic rods used in rolling contact fatigue (RCF) wear tests were cataloged using measurements of the dielectric constant and losses over a wide frequency range. An extensive data base of dielectric constant and loss was complied for silicon nitride ceramics from various sources. The dielectric properties of the RCF rods did not correlate with wear testing done by Timken Research Center. The wear tests were using a high load and may not be representative of bearing response.

As additional wear data become available at lower loads, the dielectric properties will be correlated with the results to determine if the dielectric constant measurements are a useful prediction of wear behavior. Details of this work are given in Reference 23.

1.2.3 Brillouin Scattering (J. Wicksted)

Brillouin and Rayleigh backscattering techniques were developed in an attempt to detect flaws or defects on the surfaces of Si_3N_4 balls and rollers. These techniques were used to investigate changes in the laser scattering from the surface and compare them with known wear surfaces.

Rayleigh-Brillouin backscattering techniques were used to measure effective elastic constants of both bulk and surface acoustic waves over the surfaces of Si_3N_4 ceramic bearing balls and RCF rods. Several regions of the surface of each ball or roller were measured to test the consistency of the results.

A backscattering configuration using a multipass Fabry-Perot interferometer system that can be used to study the Rayleigh and Brillouin scattered light from Si_3N_4 ceramic bearing samples was developed. We compared the surface quality from both flat and cylindrical surfaces of unpolished, excellent, mediocre, and poor bearings using Rayleigh scattering. Samples with different polished surfaces also were compared. Two Si_3N_4

ceramic balls from a lot of identically prepared samples also were measured. The peak intensities and full-width-half-maximum (FWHM) resulting from the surfaces of each of these balls have been determined. This resulted in a surface characterization graph which compared these measured parameters with their known wear tests. Although the FWHM results were not reliable, a clear distinction was seen between the known wear properties of the samples and the peak of the Rayleigh scattered intensity.

A preliminary data bank has been constructed based on the Rayleigh backscattering studies in order to assess the surface quality of the Si_3N_4 ceramic bearing balls. In addition, the Brillouin and Rayleigh scattering results are currently being prepared for presentation at conferences and in publications. Details of this work are given in Reference 24.

1.2.4 Photoacoustic Microscopy (J. Krasinski)

Photoacoustic microscopy provided a means by which sub-surface flaws could be detected, which allowed for testing of various manufacturing and polishing techniques to optimize for reliability of the ball bearing's structural integrity. The technique is based on detection of acoustic waves produced by illumination of the surface of the element by an amplitude modulated laser beam. The detector utilized was a piezo electric transducer attached to the sample. To enhance sensitivity of the laser-based photoacoustic technique, the experiment is performed at the resonance frequency of the sample/detector structure.

The photoacoustic microscope was a difficult apparatus to adequately shield from sources of noise. However, once adequate isolation has been accomplished the technique is one of very few that can observe subsurface flaws in Si_3N_4 balls used for bearing applications. The size, opaque nature, round surfaces, and the grain structure of the ball bearings to be tested make other classic techniques inadequate.

Though not conclusive, the experiments performed during this study show promise of photoacoustic microscopy providing accurate data for determining the presence or absence of flaws. Based upon these results, further study of this technique should be made. The use of alternate

monitoring techniques, which provide direct measurement of the deformation of the surface or of localized heating of the ball bearing, could reduce the noise to an acceptable level. These techniques need to be explored as they hold promise of improving the detection of flaws. Toward this end, an interferometer is under construction to allow direct observation of the surface deformations produced by the cyclic heating and cooling of the surface by an amplitude modulated laser beam.

Results of the further development of the nondestructive photoacoustic technique, including those from the interferometry work and the surface temperature measurements will be presented at conferences and in publications. Details of this work are given in Reference 25.

REFERENCES

1. Agarwal, K., "Magnetic Abrasive Finishing of Nonmagnetic Rollers," M.S. Thesis, Oklahoma State University, Stillwater, OK (1994)

2. Bhagavatula, S. R., "Chemo-Mechanical Polishing of Silicon Nitride with Chromium Oxide Abrasive," M.S. Thesis, Oklahoma State University, Stillwater, OK (1995)

3. Bhagavatula, S. R., and R. Komanduri, "On Chemo-Mechanical Polishing of Silicon Nitride with Chromium Oxide Abrasive," (references 3 and 4 as a single paper), accepted for publication in Philosophical Magazine (1995)

4. Bhagavatula, S. R., and R. Komanduri, "On the Mechanism of Chemo-Mechanical Polishing of Silicon Nitride with Chromium Oxide Abrasive," (references 3 and 4 as a single paper), accepted for publication in Philosophical Magazine (1995)

5. Hou, Zhen Bing, S. R. Bhagavatula, and R. Komanduri, "Application of Moving Disc Heat Source Theory to Magnetic Abrasive Finishing of Ceramic Rollers," submitted for publication to Trans ASME, J. Tribology (1995)

6.   Chandramouli, V., "An Analysis of Indentation of Brittle Materials," M.S. Thesis, Oklahoma State University, Stillwater, OK (1993)

7.   Dock, M, "Electromagnetic Float Polishing of Ceramic Balls for Bearing Applications," M.S. Thesis, Oklahoma State University, Stillwater, OK (1995)

8.   Fox, M., "Magnetic Abrasive Finishing of Non-ferromagnetic Rolling Elements," M.S. Thesis, Oklahoma State University, Stillwater, OK (1994)

9.   Fox, M., K. Agrawal, T. Shinmura, and R. Komanduri, "Magnetic Abrasive Finishing of Rollers," Annals of CIRP, 43/1, (1994) 181-184

10.   Hou, Zhen Bing and R. Komanduri, "A Thermal Model of Magnetic Float Polishing of Ceramics," submitted for publication in Trans ASME, J. Tribology (1995)

11.   Ming, Jiang, M. Raghunandan, and R. Komanduri, "Monitoring of Magnetic Float Polishing Process Using a Sound Sensor," to be submitted for publication in Wear (1995)

12.   Kesavan, S. R., "An *In Situ* Stage for Scratching of Glass Inside ESEM," M.S. Thesis, Oklahoma State University, Stillwater, OK (1994)

13.   Komanduri, R. and T. R. Ramamohan, "On the Mechanisms of Material Removal in Fine Grinding and Polishing of Advanced Ceramics," a keynote paper presented at the 7th Int. Conf. on Production/Precision Engineering, Chiba, Japan (September 15-17,1994) and published in Advancement of Intelligent Production (JSPE Publication Series No.1) by Elsevier Science B.V. (1994) K-38-K51

14.   Raghunandan, M.,"Magnetic Float Polishing of Silicon Nitride Balls," Ph.D Thesis, Oklahoma State University, Stillwater, OK (Summer 1996)

15.   Raghunandan, M., N. Umehara, and R. Komanduri, "On the Possibility of Chemo-Mechanical Polishing of Silicon Nitride," Proc. of

the Symposium on Tribology in Manufacturing, ASME/STLE Tribology Conference, Lahaina, Maui, Hawaii (1994) 81-89. Also, accepted for publication in Trans. ASME, J. Tribology, (1995)

16. Raghunandan, M., N. Umehara, A. Noori-Khajavi, and R. Komanduri," Magnetic Float Polishing of Ceramics," accepted for publication in Trans ASME, J of Engg. for Ind. (1995)

17. Raghunandan, M., and R. Komanduri, "Finishing of Silicon Nitride Balls," to be submitted for publication in Trans ASME, J of Engg. for Ind., (1995)

18. Iyengar, Sujatha and R. Komanduri, "A Review of Magnetic Fluids," to be submitted for publication (1995)

19. Umehara, N. and R. Komanduri, "Magnetic Fluid Grinding of HIP-SI3N4 Rollers," accepted for publication in Wear, (1995)

20. Umehara, N., "Magnetic Fluid Grinding - a New Technique for Finishing Advanced Ceramics," Annals of CIRP, 43/1, (1994) 185-188

21. Umehara, N., T. Shinmura, and R. Komanduri, "Magnetic Field Assisted Polishing - A Review," paper under preparation (1995)

22. Umehara, N. and R. Komanduri, "On the Material Removal Mechanisms in Polishing of Advanced Ceramics," paper presented at the Annual Meeting of the Japan Society of Tribologists (1994)

23. Lange, J., "Raman Scattering and Silicon Nitride Ceramics," ARPA Final Report on Ceramic Bearing Technology (F33615-92-C5933), Part 3, Oklahoma State University, Stillwater, OK (1995), WL-TR-96-4020

24. Wicksted, J., "ARPA Final Report on Ceramic Bearing Technology (F33615-92-C5933), Part 4, Oklahoma State University, Stillwater, OK (1995), WL-TR-96-4020

25. Krasinski, J. S., and G. H. Miller, "Photoacoustic Method for Nondestructive Testing of Si3N4 Ceramics," ARPA Final Report on

Ceramic Bearing Technology (F33615-92-C5933), Part 5, Oklahoma State University, Stillwater, OK (1995), WL-TR-96-4020

2. ADVANCED MANUFACTURING TECHNOLOGIES FOR FINISHING OF SILICON NITRIDE BALLS AND ROLLERS

R. Komanduri
School of Mechanical and Aerospace Engineering
Oklahoma State University
Stillwater, OH

2.1 SUMMARY

Advanced ceramics are brittle, in general, and failure of parts made from them are initiated by cracks formed at or near the surface during conventional grinding and polishing. To minimize the damage due to processing, it is necessary to finish them under gentle conditions, i.e. very low level of forces (1 N). While improved machine tools will certainly facilitate reducing deflections and chatter, need arises for applying controlled, low levels of force. Also, the finishing operation has to be economically attractive. These considerations led to the introduction of non-traditional manufacturing technologies where the material removal process is aided by a secondary source. Magnetic field assisted polishing is one such non-conventional manufacturing technology in which the cutting force is controlled by the magnetic field. As a machine tool technology for finishing, it essentially accomplishes the task without the need for designing expensive, rigid, ultra-precision, vibration free, and error free machine tools. The main advantage is that the new technology can be incorporated into existing conventional machine tools, thereby minimizing the cost of new equipment. The process can thus be very effective and at the same time economical.

At the beginning of the project, we reviewed the literature on magnetic field assisted polishing as well as on magnetic fluids. The former included extensive work done in the former U.S.S.R. and Bulgaria as well as the work done by the Japanese researchers. The latter included extensive U.S. patent literature. We also developed extensive collaborative activities with leading researchers from Japan (Professors Kato and Umehara of Tohoku

University and Professor Shinmura of Utsunomia University) and exchanged visits to discuss research of mutual interest. Based on this background, we have formulated the research methodology that formed the basis for much of the research conducted in the last three years.

We developed magnetic float polishing (MFP) processes for finishing ceramic balls as well as rollers and magnetic abrasive finishing (MAF) for finishing ceramic rollers. We designed and built equipment for magnetic float polishing (using permanent magnets as well as an electromagnet) and magnetic abrasive finishing (using an electromagnet) for rollers. We verified the machine tool characteristics, such as buoyant force and stiffness of the float polishing system, contour map of the magnetic field intensity on the surface and inside the permanent magnets in magnetic float polishing, and design aspects of electromagnet-type magnetic float polishing using the ANSYS-FEM magnetic field analysis.

In our experimentation, we started the polishing process with the as-received HIPed silicon nitride balls of nominal diameter of 13.4 mm and finished them to a diameter of 1/2 in (12.7 mm). We achieved a sphericity in the range of 0.3 to 0.9 μm, and surface finish (Ra) in the range 20-30 nm. It may be noted that the as-received silicon nitride balls also had a rim that was a belt around the middle of the balls, 200 μm thick x 5 mm wide. It took about 2 hours to remove this rim of material by our process. To complete a batch of balls took only about 16-20 hours. We completed five batches of 12 balls each. We also completed finishing two sets of 12 silicon nitride balls (1/4 in diameter). These samples will be delivered to WPAFB for further evaluation.

We finished 8 silicon nitride rollers (19 mm diameter X 26 mm long, material: Japanese source) to a finish (Ra) of 5 nm and cylindricity of 4.24 μm using magnetic fluid grinding. The surface finished by this technique provided slightly rounded edges (crown) (straightness 10 μm) which is usually part of the roller design incorporated by the designer to relieve the stress concentrations.

We also finished silicon nitride rods by magnetic abrasive finishing to a finish (Ra) of 5 nm. However, we were informed recently that the RCF rods

for use at MTI should meet the specifications for diameter and straightness as well. Since the Hardinge precision lathe we use for this application has only manual feed, we are currently automating the feed axis to obtain the desired diameter and straightness. Once this equipment is modified, we will be finishing the RCF rods received from MTI for this purpose and will be shipping them back to them for further evaluation.

We made significant contributions towards an understanding of the micromechanisms of material removal and surface generation in finishing of ceramics as well as the chemo-mechanical polishing of silicon nitride with chromium oxide abrasive. Contrary to what has been reported in the literature, we found the role of chromium oxide to be more than a catalyst and that, in fact, it actually participates in the chemical reactions forming chromium silicate and chromium nitride as evidenced by the X-ray diffraction studies of the wear debris. We also developed a model of the chemo-mechanical polishing process both in air and in water environments. We developed a thermal model of the magnetic float polishing (MFP) as well as magnetic abrasive finishing (MAF) for the calculation of flash temperatures and flash times using a moving disc heat source and applying Jaeger's classical solutions.

It may be pointed out that much of the work conducted on this project was written in the form of technical papers that were submitted (or to be submitted) for publication and/or presentation at conferences to enable rapid technology transfer. The material prepared thus far has been included in this report as Appendices A - L.

2.2 INTRODUCTION

Advanced ceramics, such as SiC, Si_3N_4, Al_2O_3, and ZrO_2, are currently finished by conventional grinding with diamond wheels followed by polishing. But grinding generally leads to several defects including large scratches, formation of pits due to dislodgement of grains, viscous flow of the glassy phase in some cases, and surface and subsurface microcracks. These defects could affect the properties, performance, and service life of these

materials. Hence the defects are removed by subsequent diamond polishing to improve strength and reliability of the parts. The conventional polishing method, however, takes considerable time, which adds significantly to the cost of manufacture of these parts and yet may not remove many of the defects. The last decade has seen the emergence of such novel finishing techniques as magnetic field assisted polishing and mechano-chemical polishing (particularly in Japan) to finish advanced ceramics cost effectively with minimal defects. The objective was to develop a 'gentle' (low force level) but fast material removal process for finishing advanced ceramics, thereby meeting the rigorous surface quality requirements.

In the following, a brief description of conventional methods of finishing (grinding and polishing) of silicon nitride balls and rollers is given. This is followed by a description of ultrafine polishing and mechano-chemical polishing techniques. The technique used in the present investigation, namely, magnetic field assisted polishing, is then presented. It is subdivided into magnetic float polishing of ceramic balls, magnetic float polishing of ceramic rollers, and magnetic abrasive finishing of ceramic rollers. The characterization techniques used for the analysis of finished balls and rollers, as well as the wear debris, are then given, followed by a discussion of the analytical techniques and the simulation used for magnetic fields in the design of magnetic field assisted polishing equipment. This is followed by a discussion of the micromechanisms of material removal and surface generation in polishing as well as chemo-mechanical polishing of Si_3N_4 with Cr_2O_3 abrasive. Finally, a thermal model for magnetic field assisted polishing of ceramic balls and magnetic abrasive finishing of ceramic rollers is presented. Finally, the researchers involved in advanced manufacturing technologies on the ARPA project, infrastructure development at OSU, and a list of publications as well as M.S. and Ph.D theses are given. Results of much of the work presented here has been submitted (or is to be submitted) for publication in various archival journals and/or presentation at various international conferences for rapid technology transfer to industry and are included in Appendix A-L.

2.2.1 Conventional Methods of Finishing (Grinding and Polishing) of Silicon Nitride Balls and Rollers

The conventional method of finishing ceramic balls initially involved ultrasonic rough grinding silicon nitride billets to ball shape. Alternately, the silicon nitride balls are sintered or HIPed to nominal size and subsequently rough ground. HIPing generally leaves a rim at the parting line. In our investigation for finishing 1/2 in (12.7 mm) balls, we received from CERBEC as HIPed balls of 13.4 mm nominal diameter with a band of 200 μm thick x 5 mm wide around the periphery of the ball. Whatever may be the initial procedure to form a nominal shape for the balls, in the conventional method they have to be rough ground initially followed by several stages of lapping. The first two stages in conventional polishing is accomplished by multigroove lapping with a 500 grit SiC in oil under a plate pressure of 40 psi in the first stage and 20 psi in subsequent stages to remove out-of-roundness. Following this, a single groove lapping is performed with a 0.25 μm diamond paste in oil to improve the surface finish. This is generally followed by metrology and NDI.

For finishing rollers, hot pressed silicon nitride is surface ground to a uniform thickness by diamond grinding. The rollers are then ultrasonically trepanned from the billets. The ends are rough ground on a Blanchard surface grinder using a diamond wheel. The outer diameter of the roller is rough ground on a centerless grinder using a diamond wheel. This is followed by chamfering of the rollers on a tool and cutter grinder using a diamond wheel. The ends of the rollers are semifinished and then finished on a double disc surface grinder using silicon carbide and alumina wheels, respectively. The outer diameter of the roller is finish ground on a centerless grinder using a SiC wheel. The corners are then blended using a vibratory finisher using alumina power. Alternately, much of the finishing is done using diamond abrasive. This is again followed by metrology and NDI of the rollers.

2.2.2 Ultra Fine Polishing Techniques

Ultrafine finish (Ra of the order of a few nanometers) on a component is achieved by the progressive removal of extremely small amounts of

material using fine abrasive grains. The traditional finishing methods hitherto employed (i.e. conventional grinding and polishing) using larger size abrasives (several μm) generate large forces. They, in turn, generate flaws and deep scratches which affect the performance of the ceramic components. As a solution to this problem, modern precision finishing techniques, such as polishing with ultrafine diamond abrasives, polishing by magnetic abrasives and abrasives in a magnetic fluid, and polishing by soft abrasives in mechano-chemical polishing, are being developed. All these processes apply controlled, low levels of force (about 1 N) for material removal.

2.2.3 Mechano-Chemical Polishing

Hard, abrasive particles used in polishing of ceramic parts remove material by scratching (brittle fracture) causing surface defects, such as microcracks, voids, and intergranular and transgranular fracture. Mechano-chemical polishing, in contrast, uses softer abrasives and the material removal is accomplished by a solid phase chemical reaction caused by the high temperatures and high pressures generated due to frictional energy at the contacting points between the abrasive and the workpiece. In this process, a very small amount of material is removed from the surface of the ceramic workpiece at the contact points as a result of chemical reaction between the abrasive and the work material. The brittle reaction product is removed by subsequent mechanical action of the abrasive. Mechano-chemical action can be obtained, for example, between Al_2O_3 and SiO_2 or Fe_2O_3, between silicon nitride and B_4C or Fe_2O_3 or Fe_3O_4 or Cr_2O_3, and between SiC and Cr_2O_3. Details on the chemo-mechanical polishing work conducted in this investigation are given in the later part of this report.

2.3 MAGNETIC FIELD ASSISTED POLISHING OF CERAMIC BALLS AND ROLLERS

The requirements of high finish and accuracy, as well as absence of any surface defects, such as cracks, combined with the difficulty of finishing ceramics, especially silicon nitride to these requirements by the conventional methods of grinding and polishing cost effectively, necessitated the

investigation of alternate manufacturing technologies. The recent contribution of tribo-chemical wear of silicon nitride suggests the possibility of a new method of finishing ceramic balls and rollers, namely, magnetic field assisted polishing. They are subclassified as: i. Magnetic float polishing (MFP) of ceramic balls and rollers and ii. Magnetic abrasive finishing (MAF) of ceramic rollers. These finish polishing techniques have recently been developed in Japan and offer great potential for the ceramic bearing components considered in this program. We now have this technology vastly improved and ready for implementation. The salient features of these techniques are the following;

1. Very high finish and accuracy can be obtained,

2. Very little or no surface damage, such as microcracks, is imparted to the ceramic parts during the finishing operation due to the application of extremely low forces,

3. Finishing operation can be significantly faster than by conventional techniques. This is due to higher spindle speeds possible using this technique,

4. Smaller polishing batch can be used. For example, very few ceramic balls are needed in a batch for polishing, unlike in conventional polishing where a large number is required for alignment and accuracy requirements. This is an advantage where new materials are being developed for specific applications and have to be tested or where the demand is such that only a small batch is needed.

5. Fewer polishing steps are needed. For example, the balls can be processed from the rough to the finished state in a single operation by varying the strength of the magnetic field intensity, abrasive size and material etc. It is, therefore, not necessary to change the polishing machines for roughing, semi-finishing, and finishing as is commonly done in conventional polishing, and

6 The equipment is very simple and inexpensive. In addition, the apparatus can be easily incorporated in any conventional machine tool. Hence, the capital costs are minimal or negligible.

Although the magnetic field assisted polishing concept was originated in the U.S., it was in the former U.S.S.R. (Baron and his associates [1-5]) and Bulgaria (Mekedonski and his associates [6]) that much of the development work took place after World War II. These researchers have shown that the technique can be applied to a wide range of products. In the 80's, the Japanese researchers (chiefly, Professor Kato and his associates of Tohoku University [7-11], Professor Nakagawa and his associates of Tokyo University [12], and Dr Shinmura and his associates of Utsunomia University [13-16]) followed this work and began applying the techniques for finishing. Several ceramic companies in Japan, including Toshiba, are actively working in this area. In the U. K., Childs et al [17-19] extended Professor Kato's work on magnetic fluid grinding from a mechanical engineering point of view. The Principle Investigator, R. Komanduri, is working actively with two leading research groups in Japan, namely Professor Kato's group and Professor Shinmura's group, where much of the research and development in this field is currently taking place.

2.3.1 Magnetic Float Polishing of Silicon Nitride Balls

Magnetic float polishing (also termed as magnetic fluid grinding) is a novel finishing process for finishing ceramic balls. It is based on the magneto-hydrodynamic behavior of a magnetic fluid that can float non-magnetic abrasives suspended in it under the action of a magnetic field. The process is considered highly effective for finishing because a buoyant levitational force is applied to the abrasives in a controlled manner. Hence, the forces applied by the abrasives to the component are extremely small and highly controllable. The magnetic field can be produced using a bank of permanent magnets (alternate N and S) or by an electromagnet. The magnetic fluid (also known as ferrofluid) is a colloidal dispersion of extremely fine (100 to 150 A), subdomain ferromagnetic particles, usually magnetite (Fe_3O_4), in various carrier fluids, such as water or kerosene. They are made stable against particle agglomeration by coating them with a suitable surfactant. When a

magnetic fluid is placed in a magnetic field gradient, it is attracted toward the region of higher magnetic field. If non-magnetic particles (abrasives in this case) are dispersed in the magnetic fluid, they are discharged towards the regions of lower magnetic field. When the field gradient is set in the gravitational direction, the nonmagnetic particles are made to float by the action of the magnetic levitational forces. The polishing operation is thus facilitated by the magnetic buoyant levitational force.

Apart from producing smooth surfaces, the process is known to reduce the finishing time by as much as 40 times compared to conventional lapping [7]. Figure 1 is a schematic of the magnetic float polishing (MFP) process. A cylindrical container (non-magnetic) placed on a bed of permanent magnets with alternate N and S holds a colloidal mixture of magnetic fluid and the abrasive (about 10 %vol). The abrasive particles and float are suspended in the magnetic fluid to a depth at which the magnetic force balances the gravitational force. A non-magnetic shaft holds the top plate, which is immersed in the magnetic fluid, and presses the balls down. A diverging magnetic field is created in the fluid which repels the abrasive particles, the balls, and the float from the magnets. The balls to be finished (also non-magnetic) are placed on top of a non-magnetic circular disk (known as the float) at the periphery of the container. Each ball contacts the float, the top plate, and the side of the container, forming a three point contact. Thus, good sphericity can be achieved. The top plate is rotated at high speed (up to 10,000 rpm).

Experimental Apparatus

Magnetic float polishing of ceramic balls can be carried out in two different types of equipment - permanent magnet-type and electromagnet-type. Figures 2 (a) and (b) show photographs of the experimental set-up using permanent magnets and an electromagnet, respectively. In this investigation, the top plate is attached to the spindle of the Bridgeport CNC milling machine or the Professional Instruments Inc. high speed, high precision, air bearing spindle. This gives the required accuracy and rigidity of motion and a speed range of up to 10,000 rpm. As already mentioned, the chamber

DRIVE SHAFT

ACRYLIC GUIDE RING

MAGNETIC FLUID AND
ABRASIVES

URETHANE RUBBER

CERAMIC BALLS

ACRYLIC FLOAT

ALUMINIUM CHAMBER

MAGNETS

STEEL BASE

N S N S N S
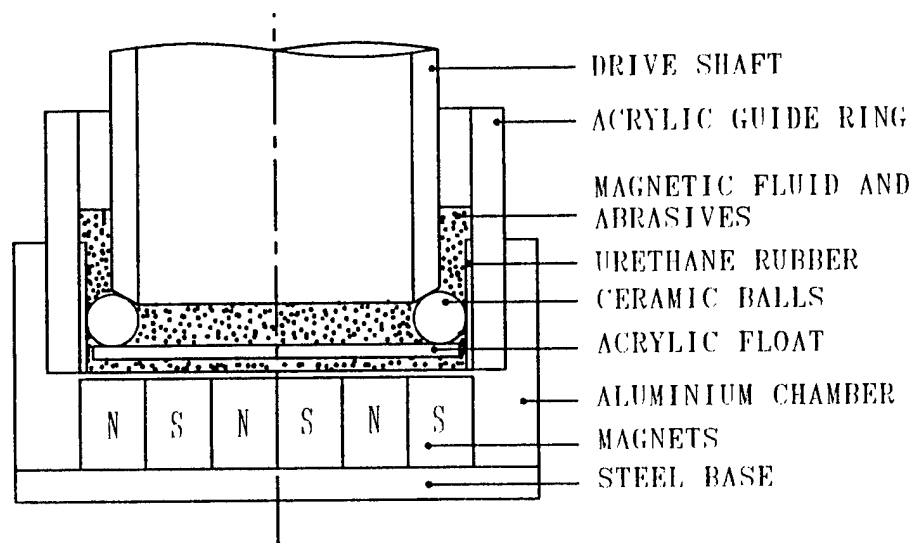
Figure 1   Schematic of the magnetic float polishing (MFP) apparatus using permanent magnets
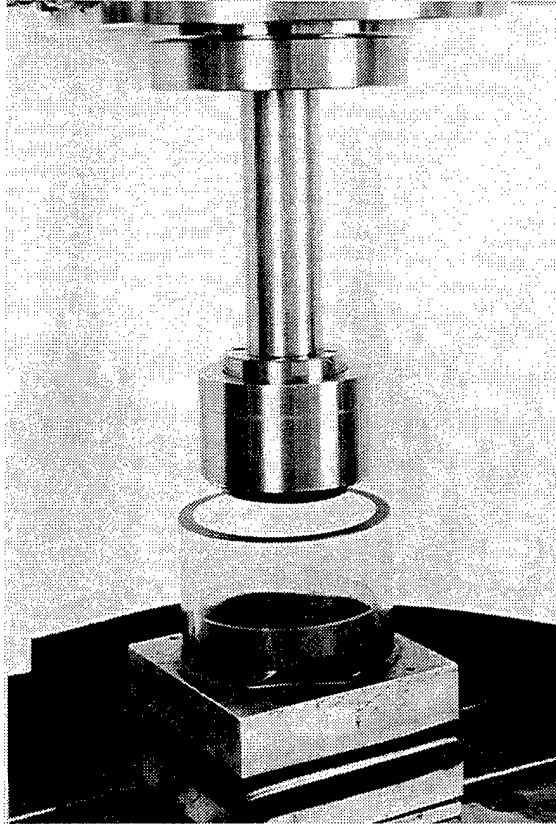
Figure 2 (a)   Photograph of the magnetic float polishing (MFP) apparatus using permanent magnets
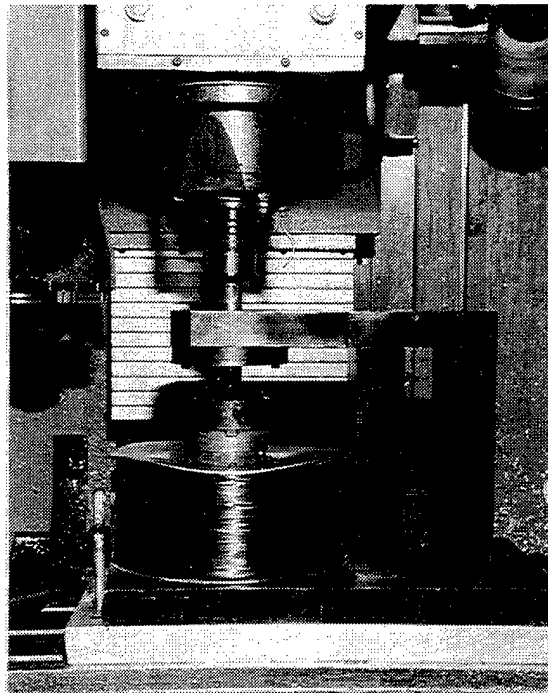
Figure 2 (b)   Photograph of the magnetic float polishing (MFP) apparatus using an electromagnet

26

containing the balls and the float is filled with magnetic fluid and fine abrasives (about 10 vol %).

In the permanent magnet set-up, a bank of permanent magnets is arranged below the chamber, with alternating N and S polarity. In the electromagnet set-up, the magnetic field is obtained by an electromagnet with the N-pole below the chamber and the S-pole above in a horse shoe type arrangement. The electromagnet consists of a core, around which a coil of copper wire is wound. The magnetic field is produced by passing DC current through the coil. When the magnetic fluid is placed in a magnetic field with a gradient in the vertical direction, an upward buoyant force is exerted on all non-magnetic materials present in the magnetic fluid. Thus, the balls are pushed by the float against the top plate with a buoyant force F_b. Similarly, the abrasives remain suspended at certain heights inside the fluid are also pushed by the buoyant force F_b. The polishing action occurs by rapid rotation of the balls through the abrasives. Table 1 gives the specification of the magnetic float polishing equipment.

Table 1 : Specification of the Magnetic Float Polishing Equipment

Work material	:	HIPed Si_3N_4 Balls
Abrasive type	:	Cr_2O_3, CeO_2, Fe_2O_3, MgO, B_4C, SiC, SiO_2
Abrasive size	:	1-30 μm
Magnetic fluid	:	Ferrofluid (water or oil based)
Gap	:	1 - 6 mm
Speeds	:	1000-10000 rpm
Load	:	0.1 - 2 N/ball

Electromagnet Set Up

Coil current	:	0.5 - 4 A

Permanent magnet Set Up

Magnet material	:	Nd-Fe-B
Width of magnets	:	0.25, 0.375, 0.5 in.
Thickness of magnets	:	2 x pole width

Experimental Procedure

It may be noted that the polishing efficiency is dependent on many factors, including the speed of rotation, buoyant force of the float, stiffness of the float, and size and material of the abrasive used. The buoyant force of the float and stiffness of float are controlled by the gap between the float and the magnet as well as the magnetic field intensity and gradient of the magnetic field. The required field intensity and gradient are obtained by varying the coil current in the case of the electromagnet set-up or by selecting appropriate pole width and material of the magnets for the permanent magnet set-up. The ceramic balls are placed around the periphery in the chamber and the top plate is positioned to obtain the required gap. Tests are carried out at selected speeds. The polishing process is interrupted periodically and various features of relevance to the finishing of ceramic balls are determined.

Experimental Results

Figures 3 (a) and (b) are TalyRond roundness traces of an as-received silicon nitride ball (NBD 200 from CERBEC) (13.4 mm nominal diameter) and the finished ball. The final sphericity is in the range of 0.3 to 0.9 μm. Note the ring around the periphery of the ball at the parting line of the HIPing process in the as-received ball. The band was found to be about 200 μm thick x 5 mm wide. It took only about 2 hours to remove this ring of material by magnetic float polishing. Figure 4 is a Talysurf trace of the finished ball showing a surface finish of about 18.3 nm. Figure 5 is a ZYGO plot of the finished ball showing an R_a of about 7.4 nm. We took only about 16-20 hours to complete one batch. We completed five batches of 12 balls each. We also completed finishing two sets of 12 silicon nitride balls (1/4 in diameter). Details of the finishing of silicon nitride balls are given in Appendix A (under separate cover).

2.3.2 Magnetic Abrasive Finishing of Silicon Nitride Rollers

Magnetic abrasive finishing (MAF) is also a novel polishing technique with high material removal rate (1 μm/min) and finish capability. Figure 6 is a schematic of the magnetic abrasive finishing process. The magnetic abrasive employed here is an agglomerate of ferromagnetic particles (iron) and fine
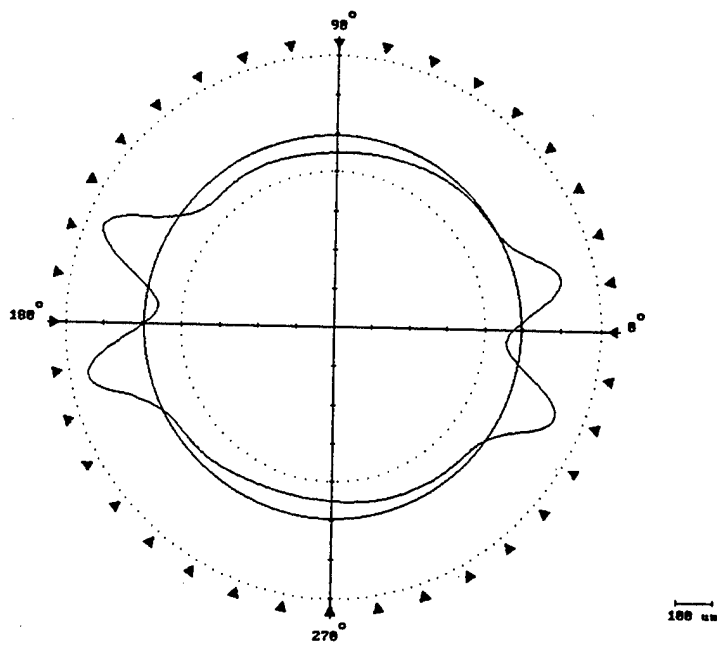
Roundness   206.35 μm

Figure 3 (a)   TalyRond roundness trace of an as-received Si_3N_4 ball
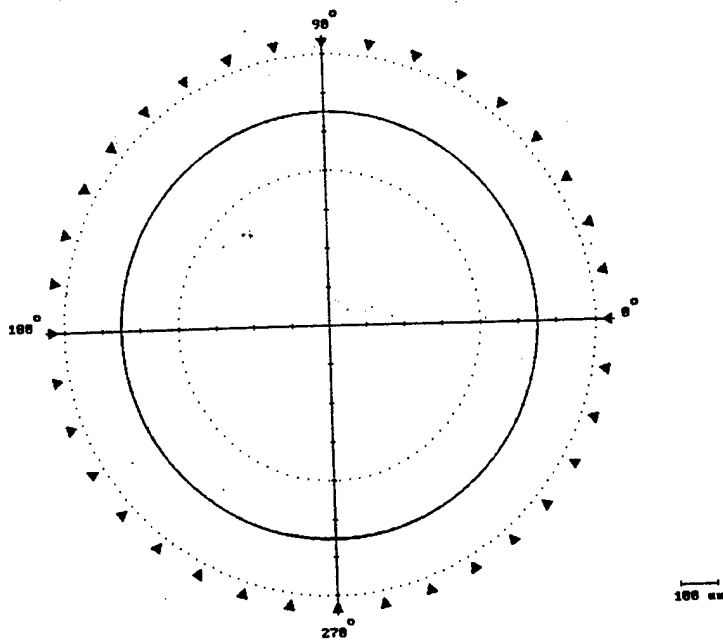
Roundness   0.50 μm

Figure 3 (b)   TalyRond roundness trace of a finished 1/2 in diameter Si_3N_4 ball

R_a 18.3 nm R_t 0.49 μm

0.2 μm

200 μm
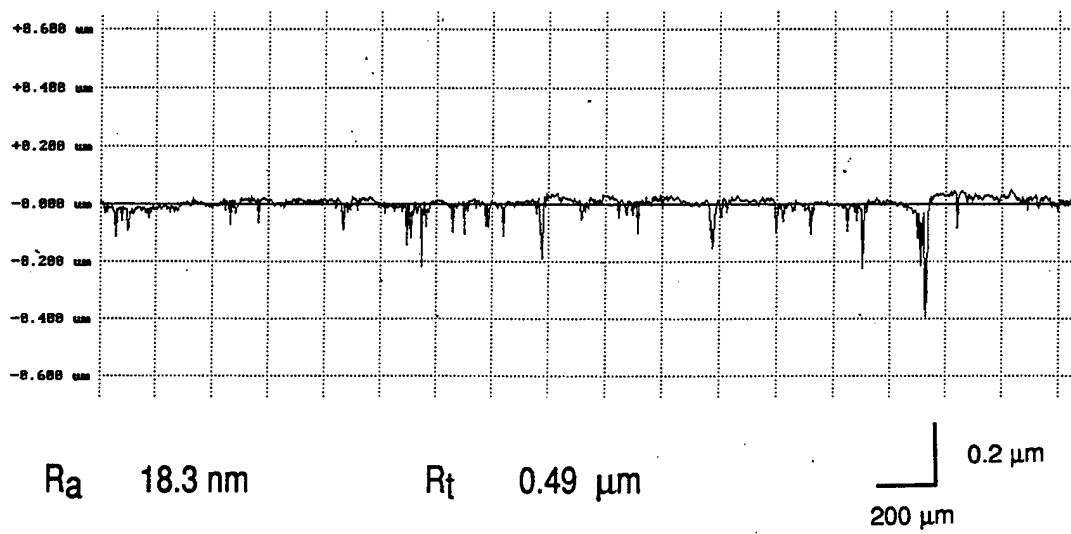
Figure 4   TalySurf trace of the finished 1/2 in diameter Si_3N_4 ball

Figure 5   ZYGO plot of the finished 1/2 in diameter Si$_3$N$_4$ ball

abrasive with or without a solid lubricant. The magnetic abrasive when charged into the gap between the magnetic poles forms two magnetic abrasive brushes around the periphery of the roller [Figure 7]. When a nonmagnetic cylindrical workpiece, such as a ceramic roller, is placed in the magnetic field and rotary and vibratory motions are given, surface and edge finishing operations are performed by these magnetic abrasive brushes. The process is highly efficient and the removal rate and finish depend on many factors including the workpiece circumferential speed, magnetic flux density, working clearance, workpiece material, size of the magnetic abrasive agglomerate including the type of abrasive used, grain size, and volume fraction of the abrasive in the magnetic abrasive agglomerate. The mean diameter of the magnetic abrasive agglomerate is in the range of 50 to 400 μm and the mean diameters of the abrasive is in the range of 1 to 10 μm.

Experimental Apparatus

Figure 8 (a) is a photograph of the experimental set-up used for polishing of ceramic rollers and Figure 8 (b) is a close up showing details. The apparatus consists of an electromagnet for the generation of the magnetic field. The copper coil, wound in the form of a solenoid, is used for the generation of the magnetic field in the core. The magnetic core material is generally a low carbon steel (0.16% C). Magnetic heads are designed such that the magnetic field is concentrated with minimum leakage surrounding the air gap between the magnetic heads. A pneumatic air vibrator is used for providing the vibratory motion to the magnetic heads. The equipment is mounted on a 1.5 hp Hardinge precision lathe with continuous speed capability up to 3000 rpm. Table 2 gives the specifications of the magnetic abrasive finishing equipment.

Experimental Procedure

In the magnetic abrasive finishing process, a magnetic field is generated using the electromagnet. Current in the range of 0.5-2 A is passed through the copper coil wound in the form of a solenoid. The magnetic field generated within the magnetic core passes through the magnetic head gap between the N and S poles. Magnetic abrasives are introduced in the head gap. Due to
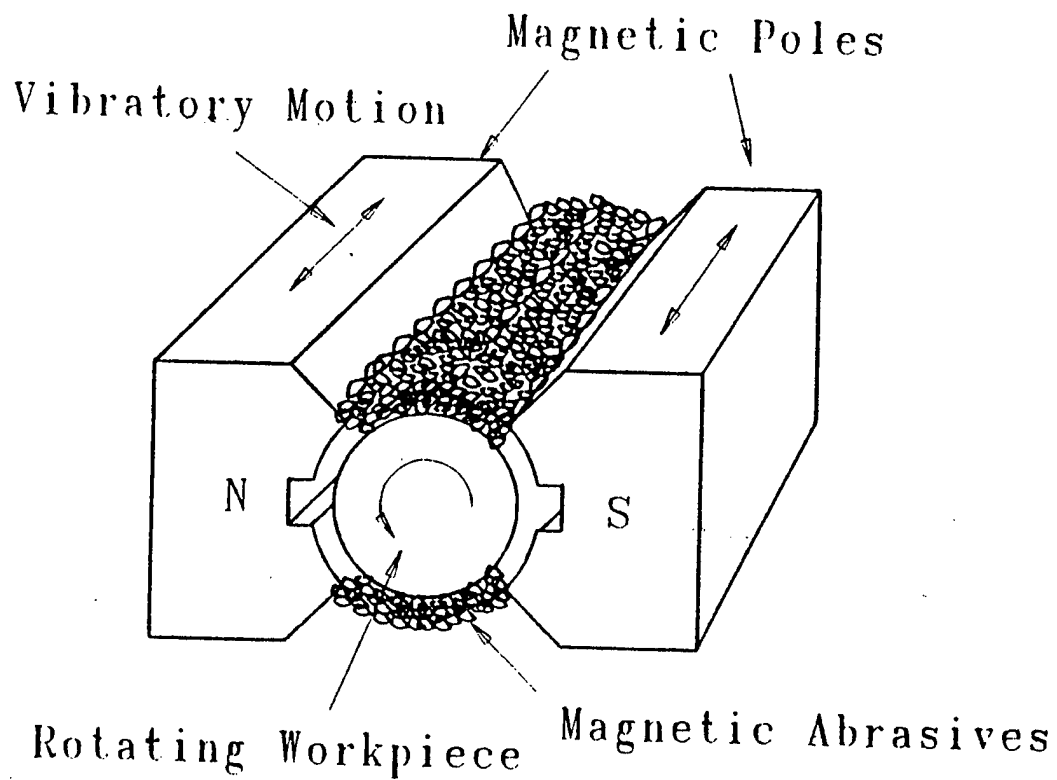
Figure 6   Schematic of the magnetic abrasive finishing (MAF) process
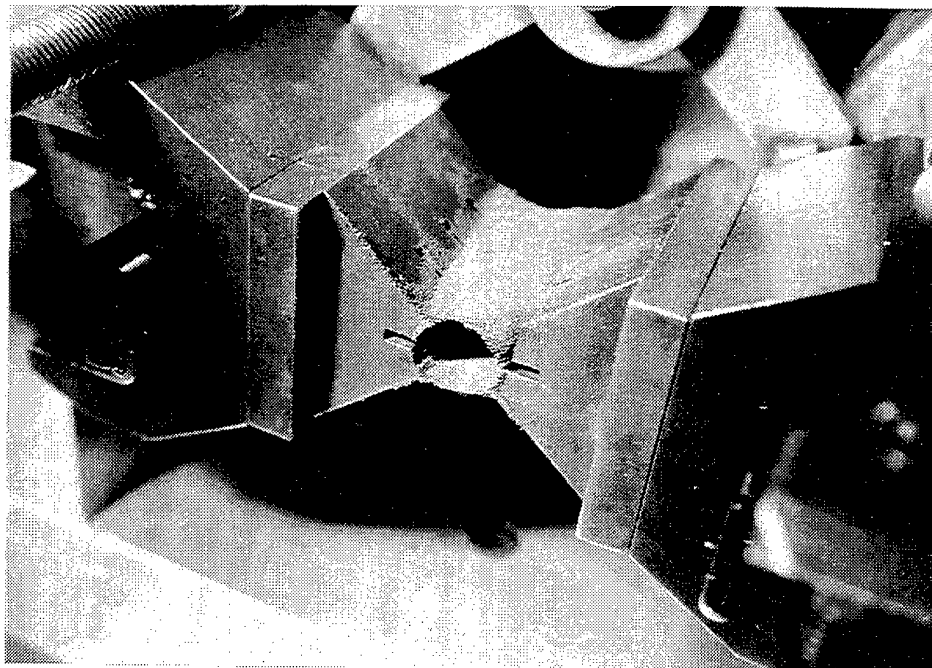
Figure 7   Photograph showing the magnetic abrasive brush in magnetic abrasive
                  finishing
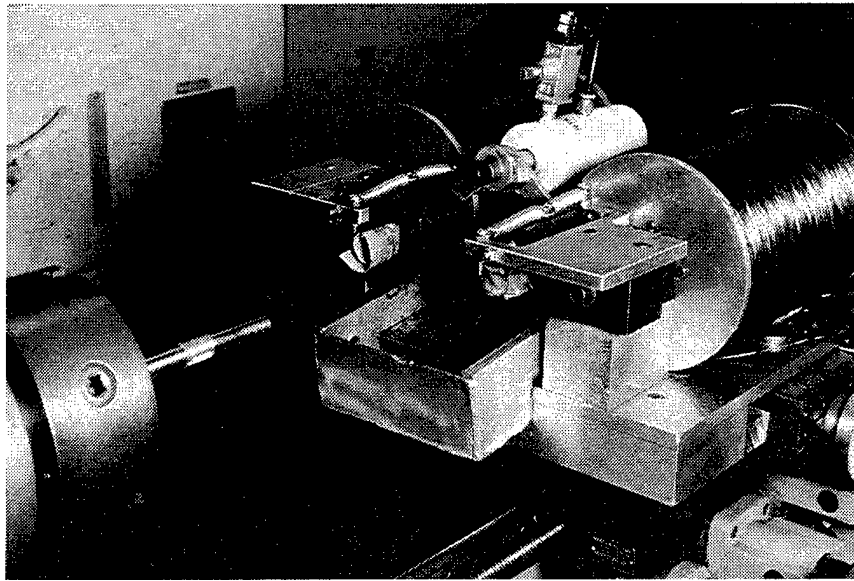
Figure 8 (a)   Photograph of the magnetic abrasive finishing (MAF) apparatus
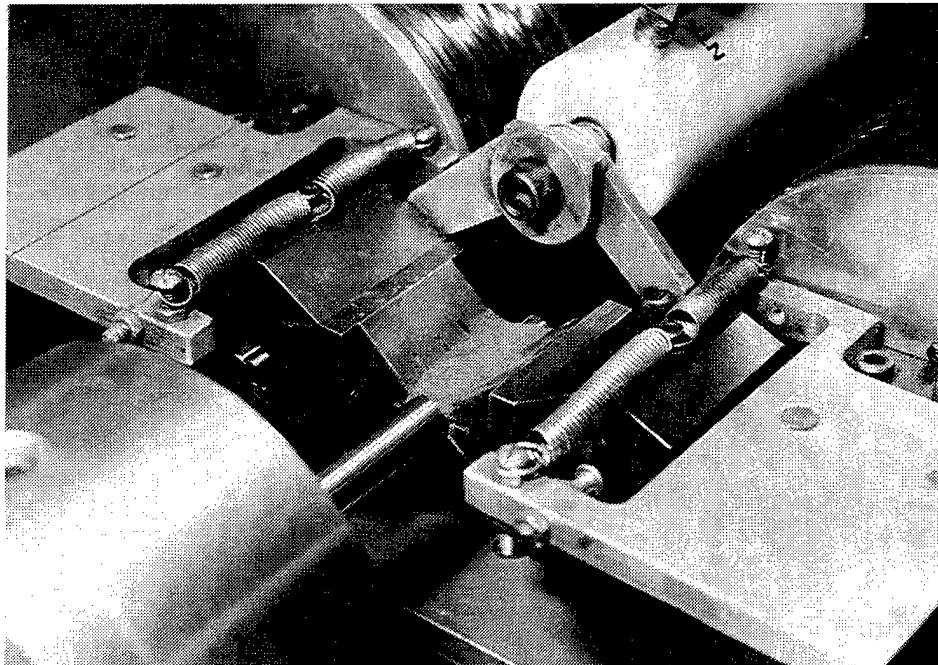
Figure 8 (b)   A close up of Figure 8(a) showing details

the presence of the field, the abrasives align in the direction of the field. The cylindrical roller to be polished is held in the chuck of the lathe. The roller is given a rotary motion and is positioned in the magnetic field. A small clearance between the magnetic head and chuck of the lathe is necessary to avoid accidental collision. The vibratory motion is provided to the magnetic head with the help of a pneumatic vibrator. The typical frequency of vibration of the head is 15-20 Hz. The abrasives are stirred at intervals of 1 minute to achieve uniform wearing of the abrasives.

Table 2 Specifications of the Magnetic Abrasive Finishing Equipment

Machine capacities:	
Machine tool	: 1.5 hp Hardinge high precision lathe
Lathe speed	: 500- 2,500 rpm
Workpiece size	: 5-15 mm diameter x 120 mm long cylindrical roller
Polishing capacity	: 45 mm long
Magnetic field intensity	: 0.5-1.2 T
Magnetic pressure	: 0-40 KPa
Magnetic core	: 0.16% carbon steel
Magnetic abrasives	: Cr_2O_3, CeO_2, Fe_2O_3, MgO, B_4C, SiC, SiO_2 abrasive (5-10 μm) in a matrix of iron particles (100-400 μm)

Experimental Results

We have received four ground rods (two CERBEC material and two Toshiba material) from MTI. We have measured the surface roughness using Talysurf and ZYGO and roundness using TalyRond. Although the Ra values of the ground surfaces are excellent and in the 10-20 nm range, the peak to valley (PV) height is found to be reasonably high (from the ZYGO plots) up to 300 nm. This is due to the formation of pits during the grinding process. This can be clearly seen in the surface map as well as intensity map of the ZYGO plot shown in Figure 9(a). Since the magnetic abrasive finishing is a 'gentle' polishing operation, very little modifications will occur in the geometry or

35

Figure 9 (a)   ZYGO plot of the as-received Si_3N_4 RCF rod
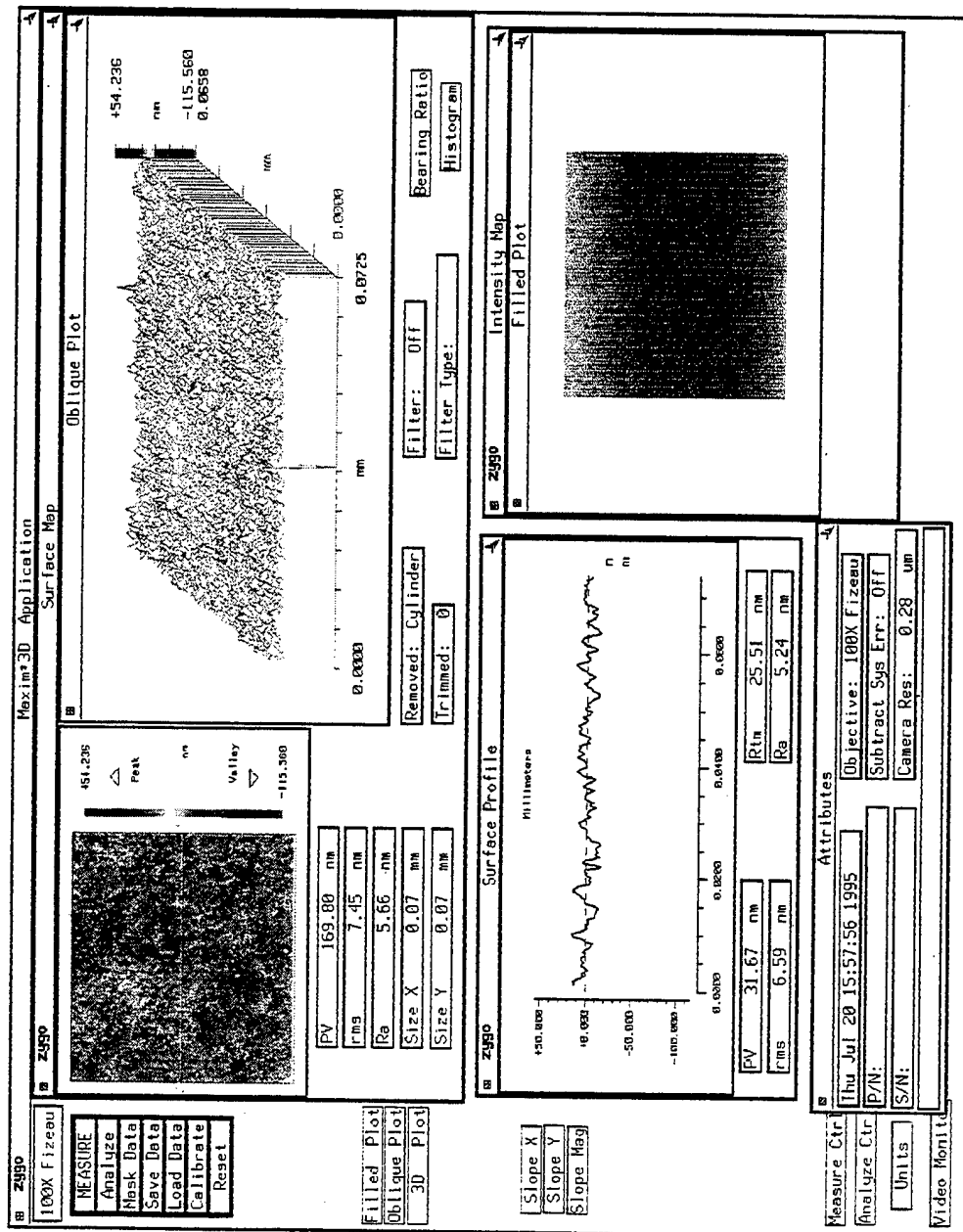
Figure 9 (b) ZYGO plot of the Si_3N_4 RCF rod finished by MAF

straightness of the rods but the finish will be improved significantly within a short period, say 10-15 min.

We measured the roundness of the as-received rods using TalyRond and found it to be in the range of 0.35 to 0.75 μm. After magnetic abrasive finishing, we found the roundness to be in the range of 0.35 μm. However, we were able to finish the ground silicon nitride rods from an initial surface roughness of 10-20 nm to 2-4 nm and bring the the peak-to-valley roughness (PV) value down to 50 nm. Figure 9(b) is a ZYGO plot showing these features. Note particularly the absence of pits in the intensity maps in this figure. With prolonged polishing it will be possible to bring down the PV value even further. Initially, we were emphasizing the finish obtainable by this technique. Since then, we were informed to produce rods to a given diameter, straightness, and finish so that they can be used as RCF rods. Since our Hardinge precision lathe is manual, we are automating the feed motion so that the desired straightness and roundness can be obtained with significantly better surface finish. This should not be a problem since magnetic abrasive finishing is a fine finishing operation which will not alter the roundness or straightness. So the final roundness and straightness will depend more or less on the initial values of the as-received material.

2.3.3 In-Process Monitoring of the Magnetic Float Polishing Equipment

As already mentioned, magnetic float polishing has been used successfully in this investigation for rapid polishing the as-received, HIPed silicon nitride balls to a good finish and sphericity. Though the total polishing time is quite short (about 16-20 hours) for finishing 1/2 in balls, the total cycle time can be higher due to intermittent breaks needed in polishing to (a) monitor the ball sphericity and ball diameter, (b) correct for the decrease in the polishing forces due to wear of the shaft and the float, (c) remachine the float and shaft surfaces as wear on these surfaces can affect the sphericity.

The total cycle time for polishing can be decreased by incorporating appropriate monitoring and control schemes. The wear on the shaft can be decreased by coating the surface of the shaft with a hard, wear resistant material, such as the newly developed superlattice coatings of B_4C. T A & T

Inc. has developed a process for this and we are working with them to explore the application of this coating to the shaft for reducing wear.

Bearing faults have been detected in the past using vibration or sound level monitoring and are being used extensively in industry. An increase in vibration/sound level generally corresponds to an increase in the wear rate of the bearing or can be a case of a faulty bearing. Frequency domain analysis can be used to eliminate extraneous noise and identify different modes of bearing failures.

To test the concept of monitoring the polishing process using force and sound sensors, we have conducted some preliminary studies. Figure 10 is a schematic of the experimental apparatus used for measuring the magnetic buoyant force and sound level during polishing. The polishing chamber is placed on a Kistler piezoelectric drilling dynamometer for measuring the buoyant force [range 20 kN in compression and 5 kN in tension; resolution 0.02 N). The sound level monitoring is performed using a digital sound level meter with an accuracy of ± 2dB and a range of 50 - 126 dB.

We characterized the variation of magnetic buoyancy force, F_b, with distance from the magnet, h, for two different magnetic pole widths (0.25 in and 0.5 in). This provides the base line data on the maximum force obtainable. From the buoyancy force measurements, the stiffness of the float was computed as the gradient of the F_b-h curve. A batch of 12 HIPed silicon nitride balls (NBD 200) (13.4 mm nominal diameter) were used in the polishing tests. The ball sphericity was measured using TalyRond. Typically, nine measurements were taken on three balls with three measurements on each ball. The polishing force at the start of the test was measured. With the piezoelectric load cell the electronic drift can become significant after a few minutes. We, therefore, incorporated a strain gauge load cell, which permits continuous monitoring of forces during the polishing process. The sound levels were measured at the start of the polishing experiment and at regular intervals during polishing. The ambient noise level of the room was measured to be 64 dB. The relative sound level (Δ dB) was obtained as the difference between the sound level measured during polishing and the ambient sound level.
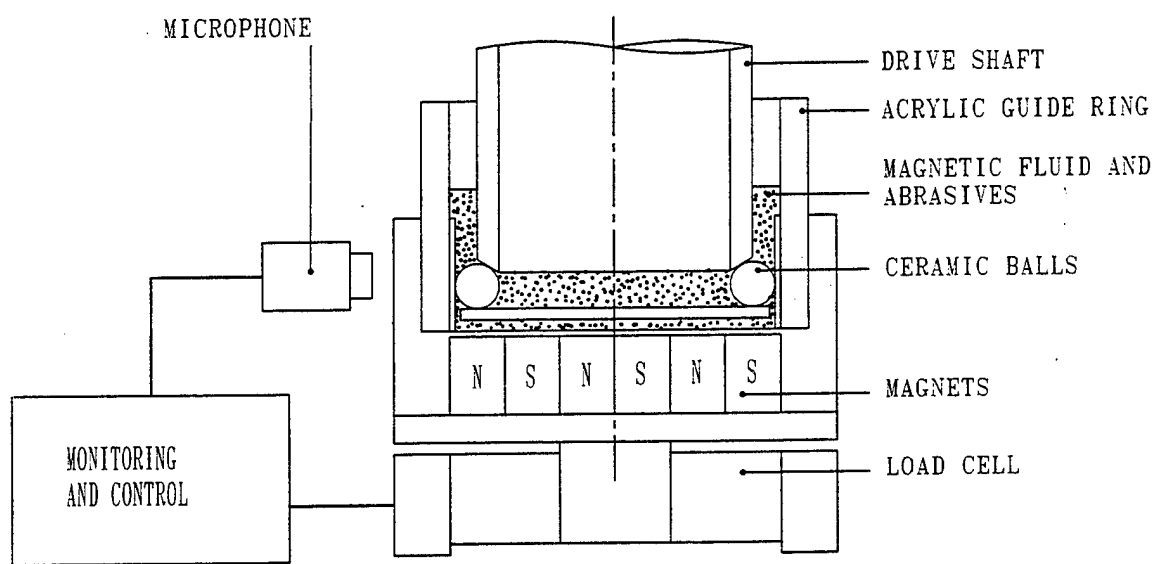
Figure 10   Schematic of the experimental apparatus used for in-process monitoring of magnetic float polishing (MFP)

Figure 11 (a) shows the variation of the magnetic buoyancy force, F_b, with distance from the magnet, h, for two different widths of magnet (1/4 in and 1/2 in). It can be seen from the figure that at distances larger than 2 mm, the 1/2 in magnet gives slightly higher forces than the 1/4 in magnet. However, at small distances, the 1/4 in magnet gives higher forces. The maximum force obtainable with the 1/2 in magnet is about 20 N, while that with the 1/4 in magnets it is about 25 N. Figure 11 (b) shows the variation of stiffness of the float with buoyancy force for 1/4 in and 1/2 in magnets. The smaller magnets give higher stiffness for all values of force. At the operating point (i.e. 12 N total polishing load or 1N/ball), the stiffness obtained from a 1/2 in magnet set-up is about 6 kN/m, while that from 1/4 in magnet set-up is 9 kN/m.

Figure 12 shows the variation of relative sound level (Δ dB) with sphericity. The initial sphericity of the balls was about 200 μm. At the beginning of polishing, the relative sound level (Δ dB) was about 35 dB. With continued polishing the sphericity improved significantly accompanied by a significant reduction in the sound level. After about 20 hours of polishing, the relative sound level (Δ dB) decreased from 34 to about 4 dB corresponding to a sphericity of 0.5 μm. Once good correlation of the sensor signals with the sphericity and finish obtained, different control strategies can be considered. The monitoring and control aspects can then be integrated into the CNC or incorporated on a PC for on-line monitoring and control of the polishing process which will be highly beneficial in industry.

2.3.4 <u>Magnetic Float Polishing of Silicon Nitride Rollers</u>

A magnetic float polishing apparatus for finishing silicon nitride rollers was developed on the basis of magnetic buoyancy theory developed by Rosenweig [20]. In an attempt to polish Si_3N_4 rollers, Umehara and Kato [21] started with the as-sintered rollers whose cylindricity was more than 50 μm. Traditional centerless grinding process cannot grind a roller of such irregular shape directly. But in this method, such irregularly shaped rollers can be ground from initial stage because of the flexible support, namely, the float. In Umehara and Kato's work, the cylindricity and circularity of the as-sintered silicon nitride rollers were reduced to one tenth of their initial values within

41
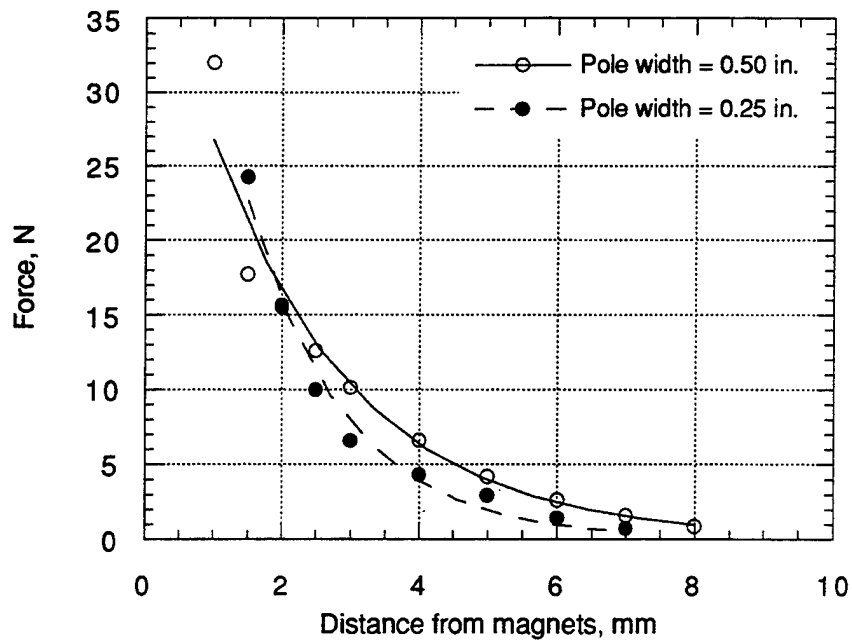
Figure 11 (a)   Variation of the magnetic buoyancy force, F_b, with distance from the magnet, h, for two different widths of magnet
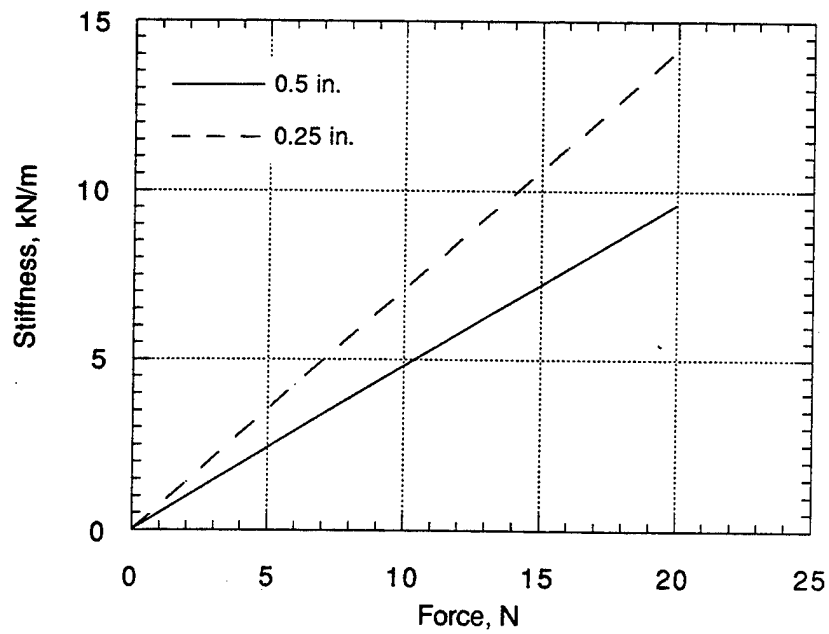
Figure 11 (b)   Variation of stiffness with buoyancy force
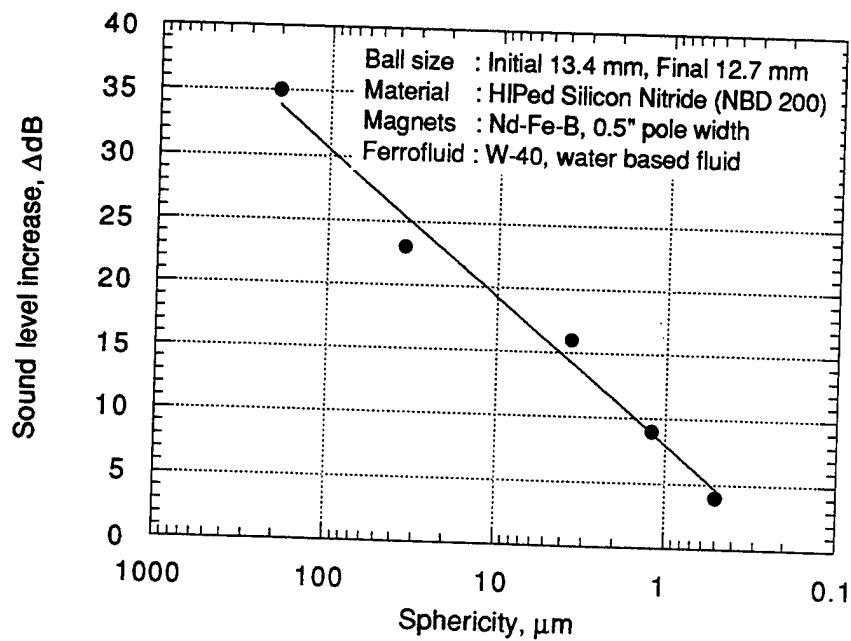
Figure 12   Variation of relative sound level (Δ dB) with sphericity

3 hours. Maximum removal rate was 0.76 μm/min. Minimum cylindricity was 22 μm. Minimum circularity around the center of the roller was 3.18 μm. These results showed the possibility of this method for rough polishing, but unfortunately, they could not obtain a smooth finish.

Figure 13 is a schematic of the magnetic fluid grinding apparatus used for finishing ceramic rollers [21]. Figures 14 (a) and (b) show the top and side sectional views of the apparatus, respectively. Figure 15 is an exploded view showing the assemblage of magnetic ring B, float, rollers, roller holder, and drive shaft. Figure 16 is a photograph of the magnetic grinding apparatus for finishing ceramic rollers.

As can be seen from Figures 13 and 14, there are two magnetic rings A and B. The magnets in both magnetic rings are made of Nd-Fe-B (Residual magnetization: 1.05 T). Magnetic ring A is comprised of 30 individual magnets assembled into one hollow cylindrical magnet (inner diameter: 95 mm, outer diameter: 145 mm, length: 60 mm). Each magnet was magnetized in the radial direction. The polarity of adjacent magnets is again alternate N and S. Magnetic ring A is fixed to the chamber [as shown in Figures 14 (a) and 15] and has two functions: one, to support the float in place like a static hydro-dynamic bearing, and the other, to facilitate in concentrating the abrasives around the center of the chamber. Magnetic ring B is comprised of 16 individual magnets assembled into a ring magnet (inner diameter: 70 mm, outer diameter: 90 mm, and thickness: 18 mm). Each magnet in this ring is magnetized in the longitudinal direction. The polarity of the adjacent magnets in this ring is again alternate N and S. Magnetic ring B is fixed to the cover plate and pushes the float in the longitudinal direction as the magnetic buoyant force is applied. The float then follows the inner 10-degree-tapered surface and presses it against the rollers.

Experimental Procedure

Table 3 is part of the specifications for the magnetic fluid grinding of rollers giving details of the work material, magnetic fluid, and test conditions used in this investigation. Eight HIP-Si$_3$N$_4$ rollers (diameter: 19 mm and length: 26 mm) were located on the roller holder (Figure 15), which acts like a

Spindle of
CNC milling machine

Driving
shaft

Magnet B

Magnetic fluid
and Abrasives

Cover plate

Float

Magnet A

Rollers
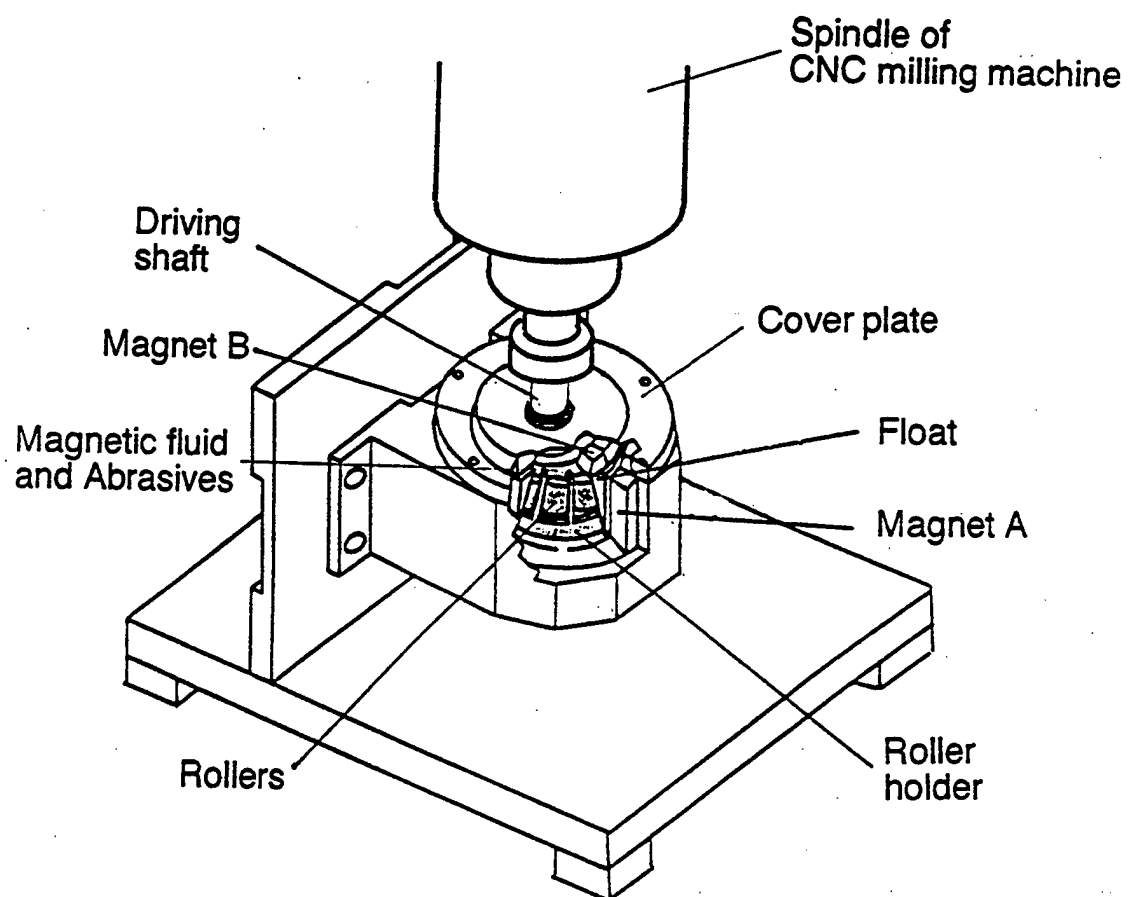
Roller
holder

Figure 13   Schematic of the magnetic fluid grinding apparatus used for finishing
ceramic rollers [21]

Magnet A

Rollers

Roller
holder

A —————— A'

Float

Driving
shaft

Magnetic fluid
and Abrasives
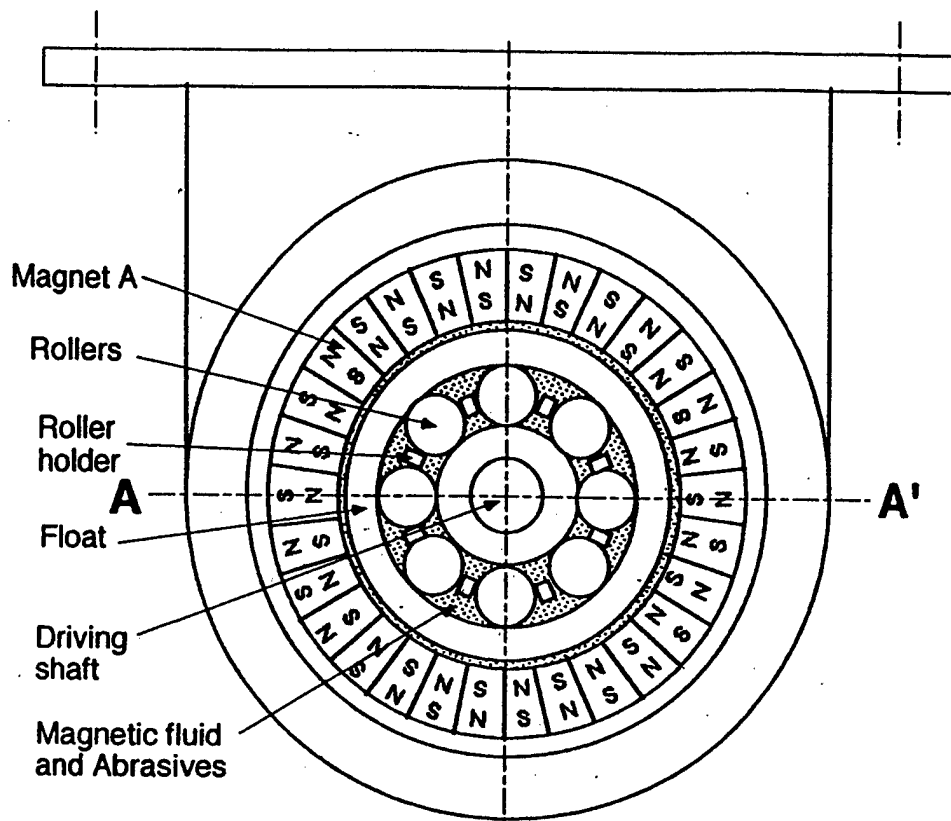
Figure 14 (a)   Top sectional views of the magnetic fluid grinding apparatus used for
finishing ceramic rollers

46
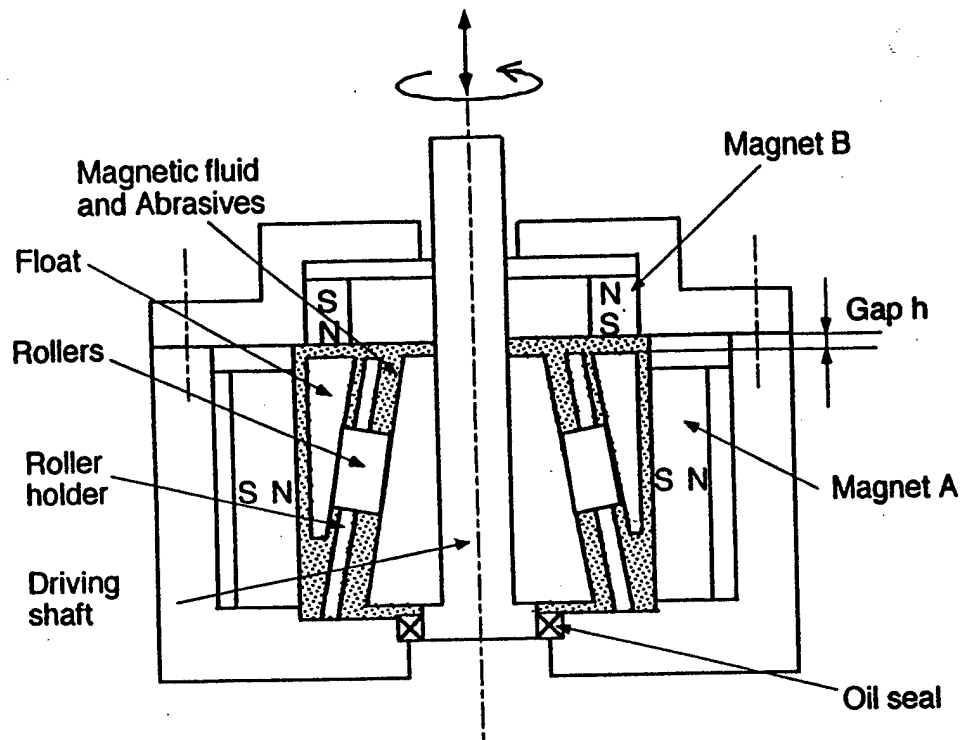
Figure 14 (b)   Side sectional views of the magnetic fluid grinding apparatus used for finishing ceramic rollers
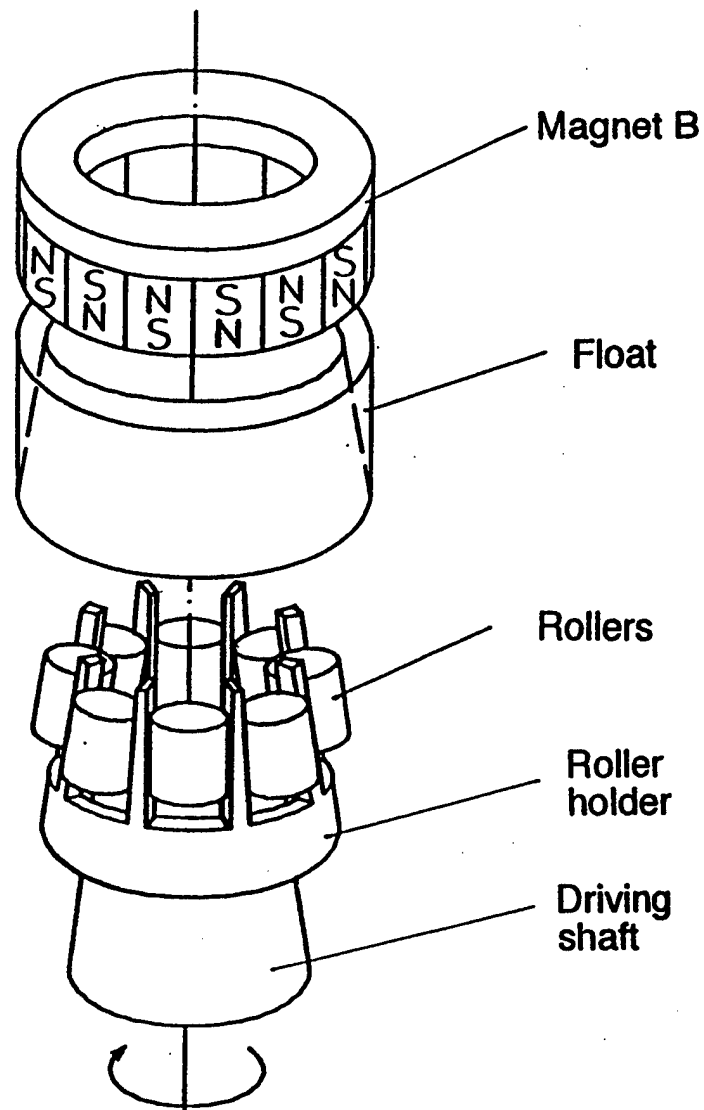
Figure 15   Exploded view showing the assemblage of magnetic ring B, float, rollers, roller holder, and drive shaft in the hole of the magnetic ring A
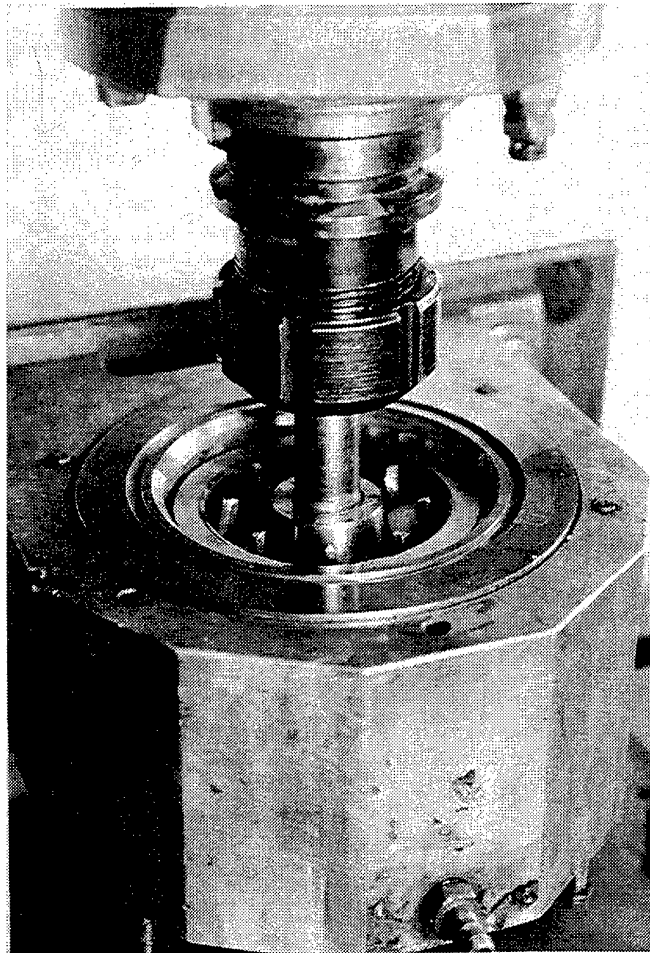
Figure 16   Photograph of the magnetic fluid grinding apparatus for finishing ceramic
                   rollers.

Table 3 : Specifications for the Magnetic Fluid Grinding of Rollers

----

Magnetic fluid   :   W-40(Water-based)

Saturated magnetization: 380G at 8000 Oe

Density: $1.40 \times 10^3 kg/m^3$

Viscosity: 25×10^{-3} Pas

Workpiece   :   HIP-Si3N4(ϕ19x26)

No of rollers: 4 or 8

Density: $3.25 \times 10^3 kg/m^3$

Strength: 100 kgf/mm^2

Hv: 1677 Kgf/mm^2

K_{1c}: 7.9 $MN/m^{3/2}$

Abrasives   : B_4C(#320)

SiC(#400, #2000)

Cr_2O_3(15-45 μm, 2-12 μm, 1-5 μm)

Concentration   :   6 Vol% abrasive

+ 94 Vol% magnetic fluid

Polishing load   :   0.084 N/roller

Speeds   :   1000-10000 rpm

Load   :   0.1 - 2 N/ball

Spindle speed   :   1500 rpm

Linear oscillation :   Stroke: 5mm

of the shaft   Frequency: 0.2 Hz

Magnets   :   Nd-Fe-B

12.7 mm width

25.4 mm thickness

10500 G residual magnetization

----

cage in a bearing. The assembly was then placed in the polishing chamber filled with the magnetic fluid (water based) and appropriate abrasive (see Table 3 for details). The drive shaft was connected to the spindle of a Bridgeport CNC milling machine which was capable of operating in the speed range of 60 - 6000 rpm. The rotation of the rollers along the axis of the shaft

was prevented by the roller holder in order to obtain high velocity between the roller and the drive shaft and consequently higher removal rates. This apparatus enabled finishing of eight silicon nitride rollers simultaneously. Depending on the size of the rollers, different roller holders needed to be used.

In an earlier work [21], only SiC abrasive was used to demonstrate the feasibility of the new finishing method for ceramic rollers. In the present investigation, three different abrasives, namely B_4C, SiC, and Cr_2O_3, were used. B_4C was selected as a hard abrasive against $HIP-Si_3N_4$ rollers for obtaining larger removal rates, while Cr_2O_3 was selected as a soft abrasive so that the rollers can be finished without any scratch marks. Also, chemomechanical action between the Cr_2O_3 abrasive and the Si_3N_4 roller was introduced resulting in a smooth surface on the rollers based on earlier work [22,23]. In this investigation, we selected very small load (0.084 N/roller) with the objective of obtaining very good surface finish (Ra 5-10 nm). Based on the earlier work [21], rotational speed of the spindle and volume concentration of the abrasive in the magnetic fluid were fixed at 1500 rpm and 6 vol %, respectively, as they seem to provide optimum conditions for polishing. Also, in order to polish ceramic rollers uniformly in the longitudinal direction, the drive shaft was given a sinusoidal oscillation during polishing (frequency: 0.2 Hz and amplitude: 5 mm) through the NC control of the machine tool.

Figures 17 (a) to (c) are surface profiles (Talysurf traces) of the silicon nitride rollers from the as-received condition to the finished state showing that the surface roughness, Ra, has improved from 1.6 μm to 4.9 nm with the Cr_2O_3 abrasive (3 and 7 μm grain sizes) after a total polishing time of 90 minutes. Figures 18 (a) and (b) are profiles in the longitudinal direction of a roller before and after polishing showing the rollers polished by this technique provide slightly rounded edges with a minimum value of straightness of about 10 μm over the length. This feature seemed to be a characteristic of the process as this process polished both the face as well as the sides, leading to rounded edges. This, however, may be considered as an advantage (and not a limitation) with this process as most rollers for bearing applications have similar geometries imposed by the designer to prevent

51
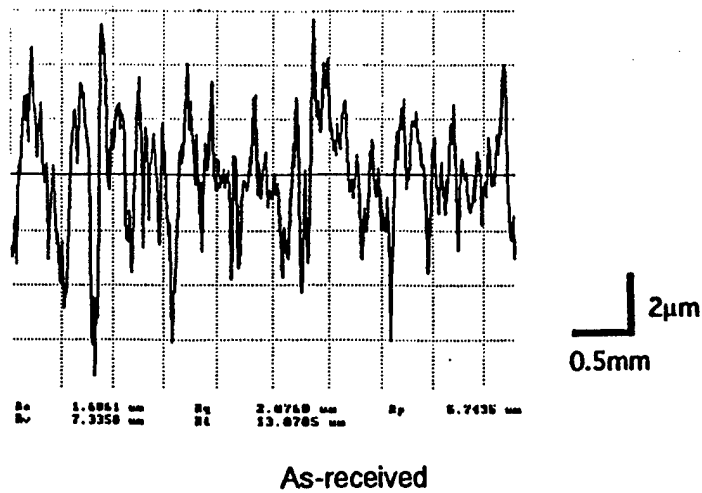
As-received

Figure 17 (a)   TalySurf trace of the as-received silicon nitride roller

Polished with Cr$_2$O$_3$ (7 μm)
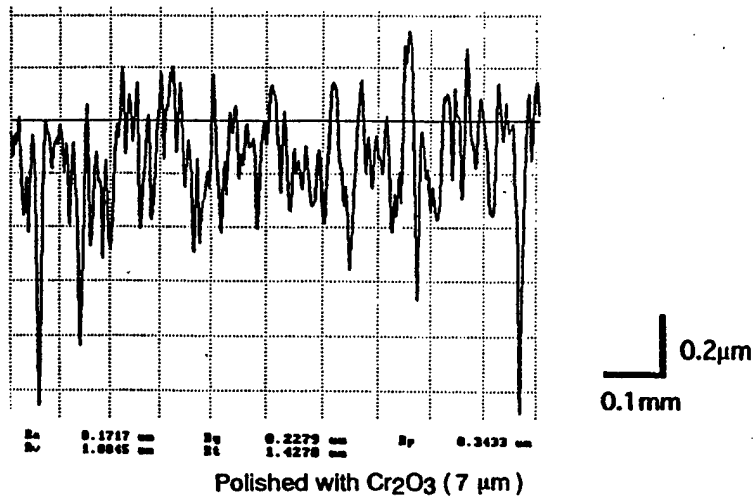
Figure 17 (b)   TalySurf trace of the Si$_3$N$_4$ roller finished using a 7 μm sized Cr$_2$O$_3$

Polished with Cr$_2$O$_3$ (3 μm)
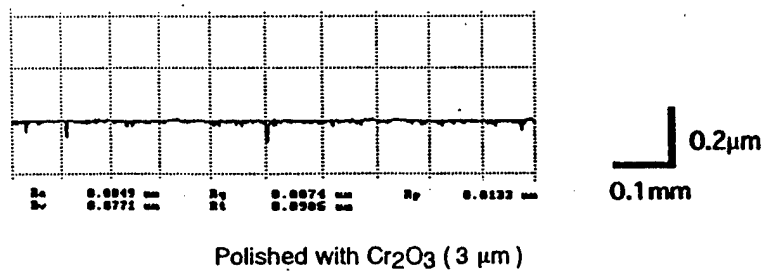
Figure 17 (c)   TalySurf trace of the Si$_3$N$_4$ roller finished using a 3 μm sized Cr$_2$O$_3$
                  showing the surface roughness, Ra, has improved from 1.6 μm to 4.9 nm

52
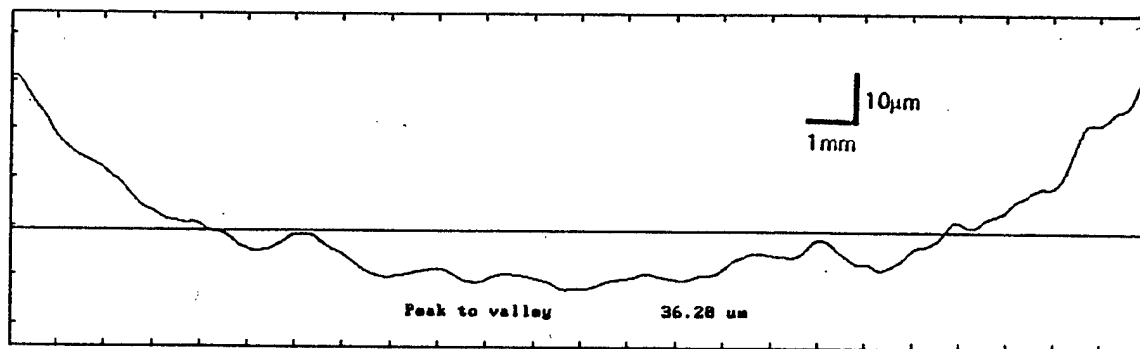
As-received

Figure 18 (a)   Straightness profile in the longitudinal direction of an as-received Si_3N_4 roller
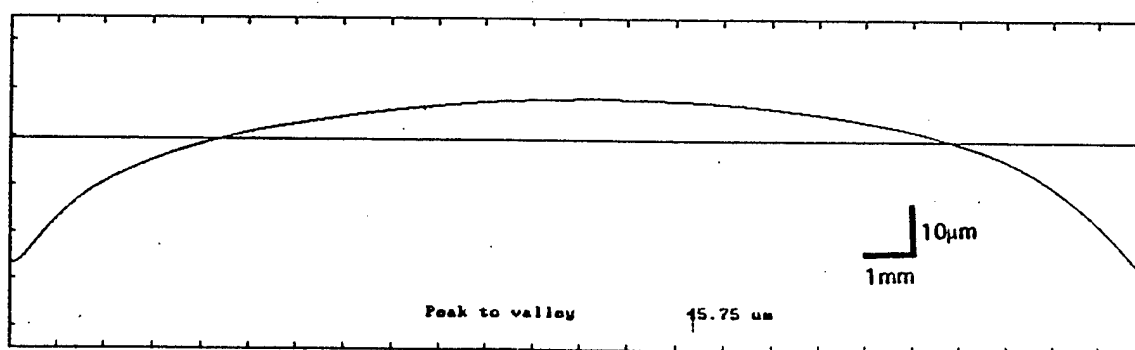
Polished

Figure 18 (b)   Straightness profile in the longitudinal direction of a finished Si_3N_4 roller showing the slightly rounded edges

stress concentrations at the contact surface. So, a secondary operation is needed to provide this crown on the rollers by conventional grinding technique, while in magnetic fluid grinding this is accomplished automatically.

Figures 19 (a) and (b) are the roundness profiles before and after polishing showing that the out-of-roundness of the roller has improved from 16.65 μm before polishing to 4.25 μm after polishing. Improvement in out-of-roundness appears to be partly responsible for the improvement in surface roughness obtained in this investigation. Figure 20 is a ZYGO plot showing the generation of a smooth surface (Ra 4.67 nm) by this technique. Details of this work are given in Appendix D (under separate cover).

2.3.5 Characterization Equipment

A non-contact ZYGO laser interference microscope, Rank Taylor Hobson's Talysurf and TalyRond, ABT 32 SEM and an ESEM both with Kevex X-ray microanalyzer, and Seimens low-angle X-ray diffractometer were used for surface characterization of the ceramic balls and rollers. The data obtained from the Talysurf and ZYGO measurements are used for the characterization of the surface texture of the polished surface by various parameters, such as average roughness, rms roughness, maximum height, and depth of the surface profile, and maximum peak to valley height. The data obtained from the TalyRond measurement are used for the evaluation of the polished surface by the various parameters such as roundness, vertical straightness, and cylindricity. SEM was used to identify surface topography and formation of grooves by abrasion, cracking, pitting etc. in addition to the chemical element identification of the surface using the X-ray microanalyzer. Siemen's low angle X-ray diffractometer was used to analyze the wear debris for possible chemo-mechanical reactions.

LS ROUNDNESS RESULTS

○   16.65 um   Meas. mode   External
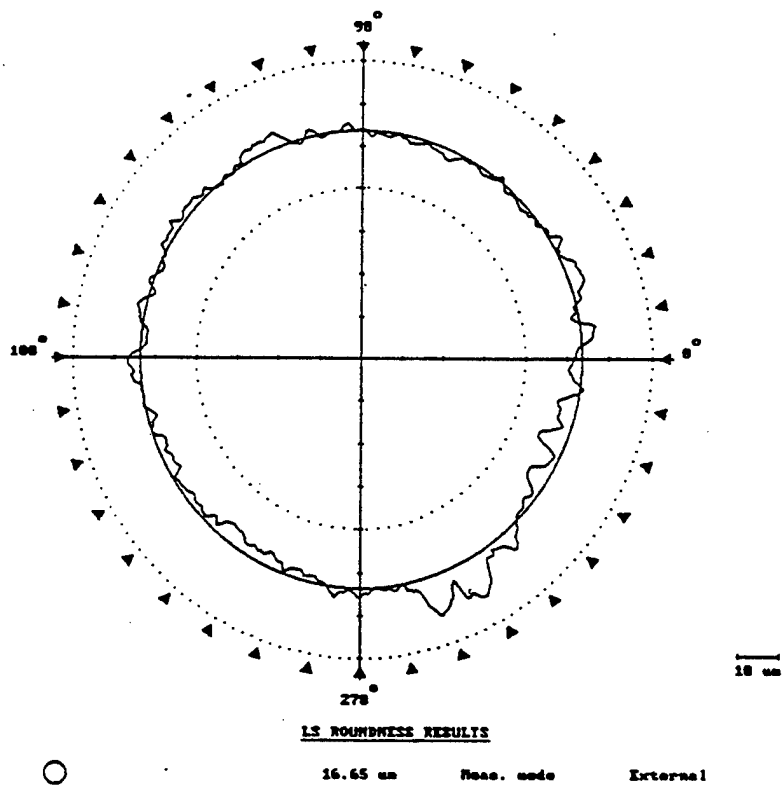
Figure 19 (a)   TalyRond roundness plot of an as-received Si_3N_4 roller

LS ROUNDNESS RESULTS

○   4.25 um   Meas. mode   External
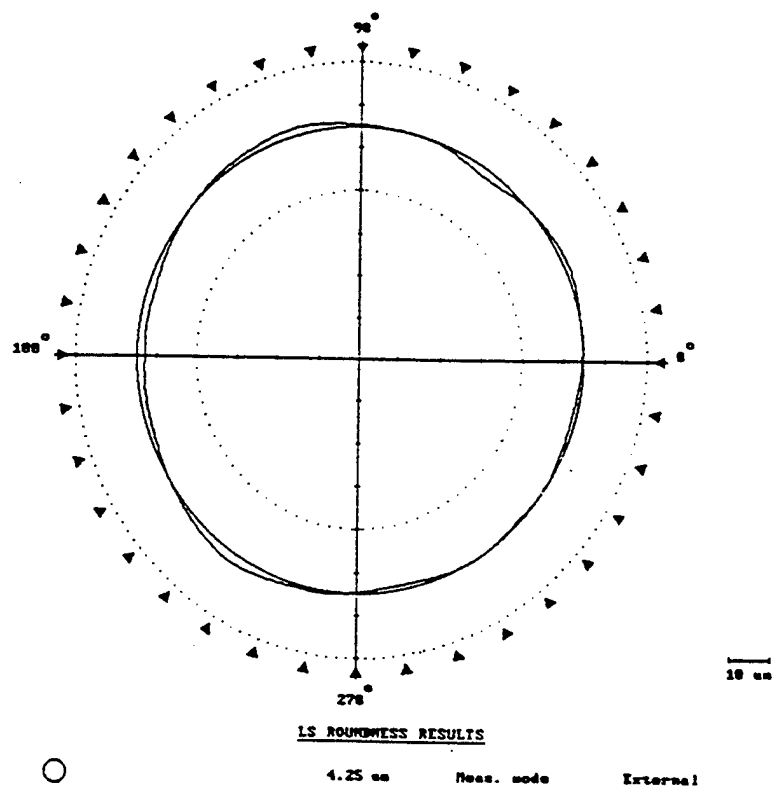
Figure 19 (b)   TalyRond roundness plot of a polished Si_3N_4 roller

55
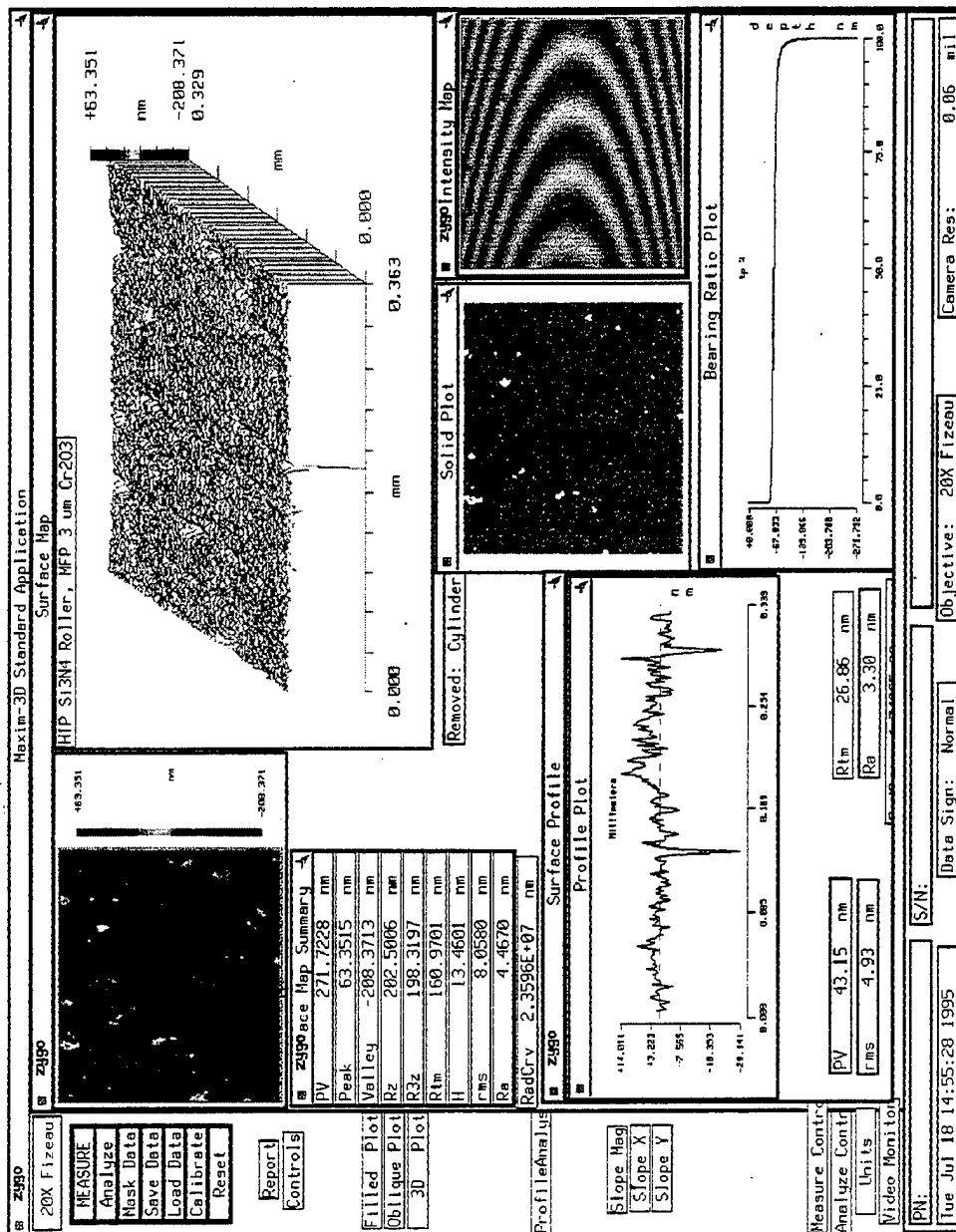
Figure 20   ZYGO plot of a finished Si$_3$N$_4$ roller

2.4. ANALYTICAL APPROACH

Ferromagnetic materials, when placed in a magnetic field, acquire magnetic polarization. The number of magnetic dipoles per unit volume of the material is known as the intensity of magnetization (or simply magnetization), and is represented by vector **M**. In the presence of a magnetizable material, magnetic field density, **B** can be shown as:

$$\mathbf{B} = \mu_o(\mathbf{M} + \mathbf{H}) \tag{1}$$

where **H** is magnetic field intensity. In the absence of any electric current in the media we have, according to Ampere's law:

$$\nabla \times \mathbf{H} = 0 \tag{2}$$

Therefore, from the divergence theorem there is a scalar potential function ϕ such that:

$$\mathbf{H} = \nabla \phi \tag{3}$$

The relation between **M** and **H** can be represented by:

$$\mathbf{M} = \chi \mathbf{H} \tag{4}$$

where χ is known as the magnetic susceptibility. For ferromagnetic materials, magnetization is strongly a function of **H**. Substituting Eq. 4 into 1, we get:

$$\mathbf{B} = \mu_o(1 + \chi)\mathbf{H} \tag{5}$$

According to Maxwell's equations:

$$\nabla \cdot \mathbf{B} = 0 \tag{6}$$

Substituting (3) and (6) into (5), we get:

$$\nabla \cdot [(1 + \chi)\nabla \phi] = 0 \tag{7}$$

This is a nonlinear equation because χ is a strong function of **H** and, as no analytical solution is currently available, it can be solved only numerically. The magnitude of **B**, **H**, and **M** can be found from Eq. 1, 3, and 4 respectively.

The forces acting on a magnetic material can be calculated through Maxwell stress tensor using the distribution of the magnetic field. Maxwell stress tensor can be represented as

$$
\begin{bmatrix} T_x & T_{xy} \\ T_{yx} & T_y \end{bmatrix} = \begin{bmatrix} [H_xB_x - H_yB_y]/2 & H_xB_y \\ H_yB_x & [H_yB_y - H_xB_x]/2 \end{bmatrix} \tag{8}
$$

If an object is immersed into the magnetic fluid, the buoyancy force, F_b, can be calculated as:

$$
F_b = (\rho_f - \rho_{mf})kV + \int_s (\tfrac{1}{2}\mu_o M_n^2 + \mu_o \int_0^H MdH)ndS \tag{9}
$$

where M, H, and M_n are the magnitudes of magnetization **M**, field intensity **H**, and magnetization, M_n, normal to the surface of the floating object respectively, ρ_f and ρ_{mf} are the density of the floating object and the magnetic fluid respectively, **n** and **k** are the unit vectors normal to the surface of the object and in the direction of the gravitational field respectively.

As pointed out earlier, susceptibly, χ, is a strong function of the magnetic field intensity, H, and hence can not be neglected in the analysis. Since there is no analytical solution to Eq. 7, it can only be solved numerically either through finite element or finite difference methods. In either methods the entire domain of the problem was divided into small elements by meshing the domain. The outputs of the program were the magnetic field H, magnetic flux density B, magnetic vector potential A, and magnetic potential, ϕ. Forces were calculated through Eq. 8 or Eq. 9. Details of this work are given in Appendix B (under a separate cover).

2.5 SIMULATION

As an illustration on the use of FEM analysis, in the following, three simulation studies on magnetic float polishing were compared with the experimental work showing a remarkable agreement between theory and experiment. They were (a) the contour map of the magnetic field intensity on the surface and inside the magnets, (b) determination of the buoyancy force and stiffness of the float, and (c) redesign of the electromagnet type apparatus to illustrate the utility of the technique as a design tool.

(a) Contour Map of the Magnetic Field Intensity on the Surface and Inside the Magnets

Childs and Yoon [17] conducted finite difference (FD) analysis to arrive at the design parameters, such as magnet width for a given ball size in a magnetic fluid grinding cell. Initially, we used the finite difference technique proposed by them to analyze the magnetic float polishing process. Unfortunately, the experimental results we obtained were found to differ significantly from the analytical values. As will be shown in the next section, the FEM analysis agrees well with the experimental values, thus lending support to the analytical technique. We attribute the lack of agreement between the values obtained using the FD technique and those of FEM technique or the experimental work to the inaccuracies inherent in the FD technique and the simplifying assumptions made in the analysis. These issues are discussed in detail in Appendix B (under a separate cover) In their analysis, Childs and Yoon assumed the magnets to be infinitely long in the N-S direction. This gives rise to the assumption that flux density on the surface of the magnet is uniform and equal to the residual magnetization (remenence) of the magnets. Childs and Yoon also neglected the internal resistance of the magnet. Figure 21 is a contour map of the magnetic field intensity on the surface and inside the magnets produced by ANSYS simulation of the magnetic float polishing using permanent magnets. The magnets are located alternately N and S. Apart from the magnets, the magnetic fluid, acrylic float and the steel plate are also shown in the figure. It can be seen that the magnetic flux density on the surface of the magnet is
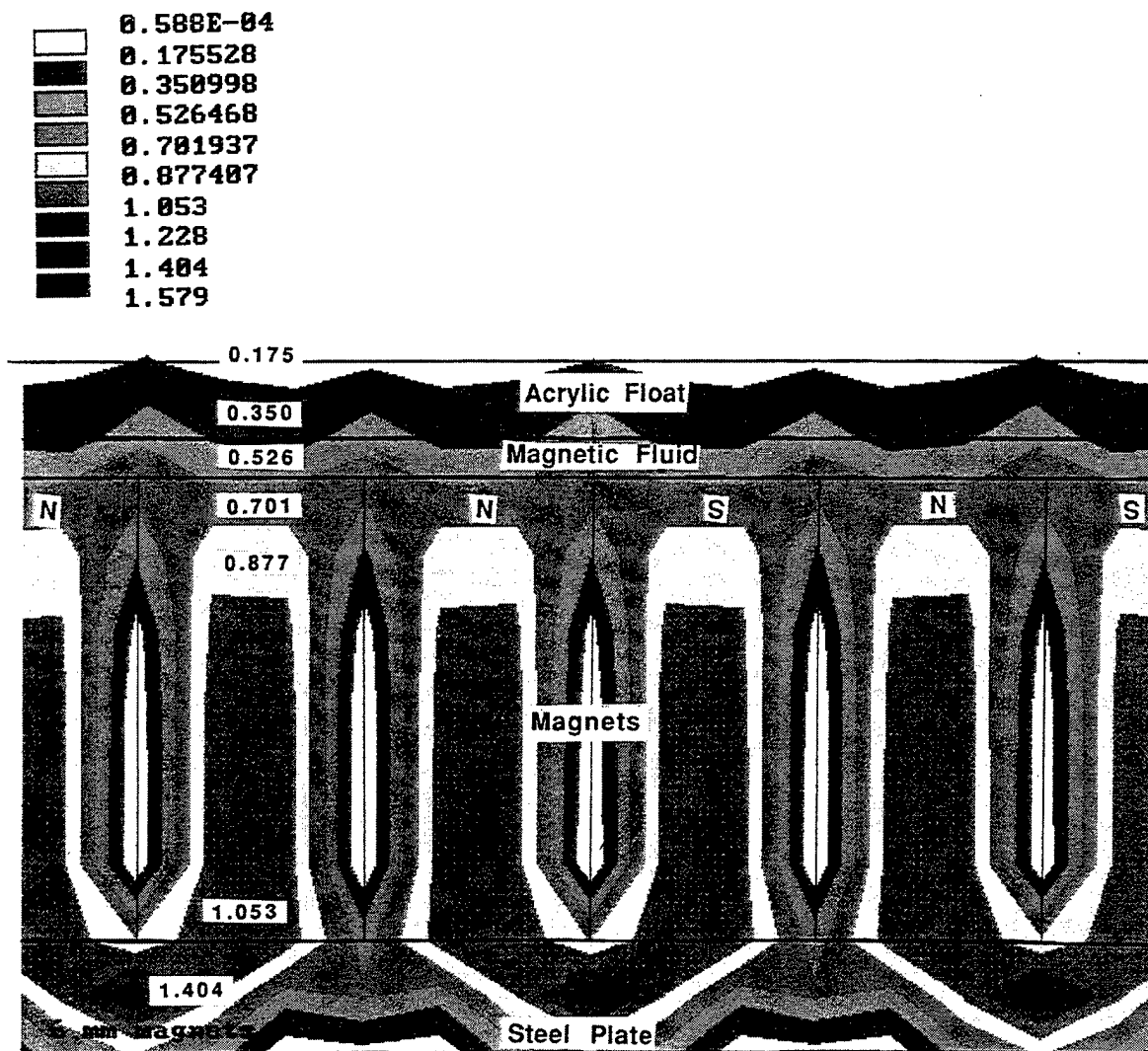
Figure 21   A contour map of the magnetic field intensity by ANSYS simulation of
magnetic float polishing (MFP) using permanent magnets

much lower than the remenence (about 0.5 T compared to the remenence of 0.96 T) and it varies over the surface of the magnet from about 0.3 to 0.5 T. Also, the magnetic flux density above the float is almost zero. Thus, the float not only increases the forces but also facilitates in smoothening out the variations in the magnetic field caused by the arrangement of magnets.

(b) Determination of the Buoyancy Force and Stiffness of the Float

Simulation studies were made using the ANSYS program to calculate the buoyant force and float stiffness in the magnetic float polishing. The geometrical information of the magnetic float polishing apparatus, such as magnet pole width, magnet thickness, diameter of the float as well as the magnetic properties of the magnet, such as residual magnetization and coercive force for magnet, M-H curve for magnetic fluid were provided as inputs to the system. Using this, a 2-D FEM analysis was performed. From the ANSYS solution, the magnetic field intensity at the nodes for different distances from the magnet were obtained. The buoyant force, F_b, was computed using the equation given by Rosensweig [20]:

$$F_b = \int_s \left(\frac{1}{2} \mu_0 M_n^2 + \mu_0 \int_0^H M \, dH \right) \vec{n} \, ds$$

(10)

The above integral was computed numerically using the field intensities obtained as above. For simplicity, it was assumed that:

$$
\begin{aligned}
M_n &= \chi H_n & H_n &< H_{saturation} \\
&= M_s & H_n &>= H_{saturation} \\
M &= \chi H & H &< H_{saturation} \\
&= M_s & H &>= H_{saturation} \\
\chi &= M_s / H_{saturation} &
\end{aligned}
$$

where H_n is the field intensity normal to the surface, H is the magnitude of field intensity, $H_{saturation}$ is the field intensity beyond which the magnetic fluid is saturated, M_s is the saturation magnetization, and M_n is the magnitude of magnetization normal to the surface.

From the above computations, F_b for different distances from the magnet (h) were obtained. Using these values, a function relating F_b and h was obtained. Stiffness of the float was computed by differentiating the above function with respect to h. Figure 22(a) shows the variation of the buoyant force on the float versus the gap between the magnet and the float and Figure 22(b) shows the variation of stiffness with buoyant force on the float obtained from analytical computations. The experimentally determined curves for the variation of the buoyant force on the float versus the gap between the magnet and the float and the variation of stiffness with buoyant force on the float are given in Figures 22(c) and (d) respectively. A remarkable agreement both in terms of magnitude and slope between experimental results and analysis can be noted for three different widths of the magnet. Such an excellent agreement between simulation and experimental work would enable one to design the system for an appropriate value of stiffness and buoyant force before it was built and experimentally tested for its performance evaluation, thus saving considerable time, money, and effort. Once we understand the relationship between the stiffness of the float, buoyant force with the removal rate and finish obtainable, we intend to develop in future optimum designs for this process.

(c) Redesign of the electromagnet type apparatus

The electromagnetic float polishing apparatus was designed and built for the first time to evaluate its performance with that of a permanent magnet set-up. It was also felt that the magnetic field strength and other parameters can be varied more easily with the electromagnetic set-up than the permanent magnet set-up. Dr. Shinmura, in collaboration with Dr. Komanduri, drew on his experience with the electromagnet design for magnetic abrasive finishing (MAF) and extended it to magnetic float polishing (MFP) by considering the similarities between the electromagnet and permanent magnet designs. Using the data given by Umehara and Kato [8], Shinmura took the values of typical field strengths for permanent magnets and air gap and used the same values to determine the design parameter, namely, minimum current and number of turns, etc., for the electromagnet design. The electromagnetic setup was then designed and built

62
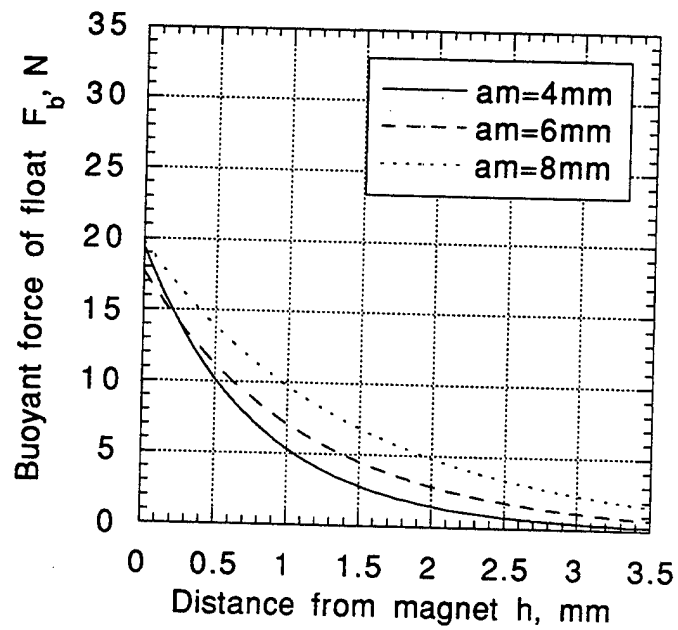
Figure 22 (a)   Variation of the magnetic buoyancy force, F_b, with the gap between the magnet and the float, h
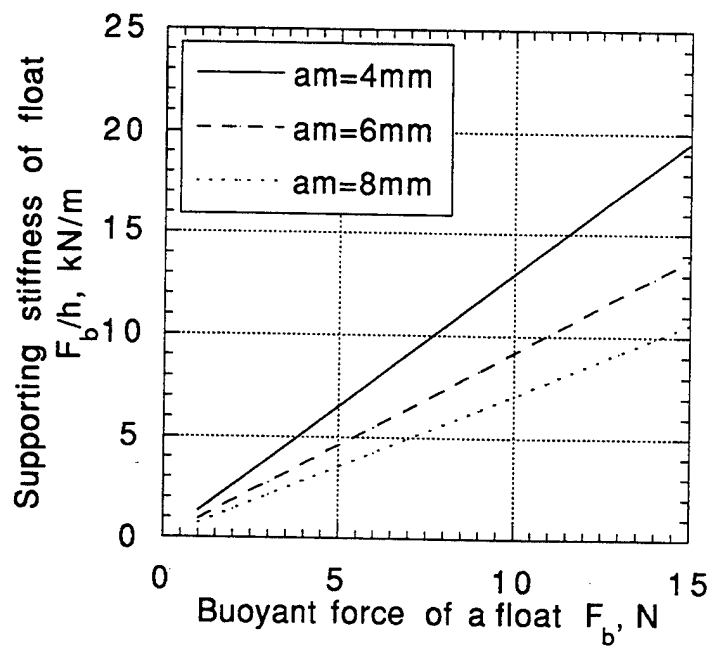
Figure 22 (b)   Variation of stiffness with magnetic buoyancy force, F_b
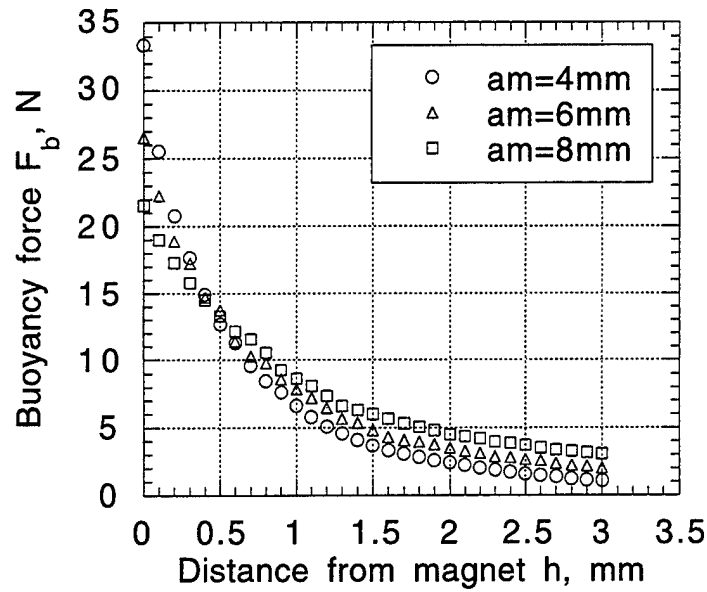
Figure 22 (c)   Experimental results for the variation of magnetic buoyancy
force with distance from the magnet
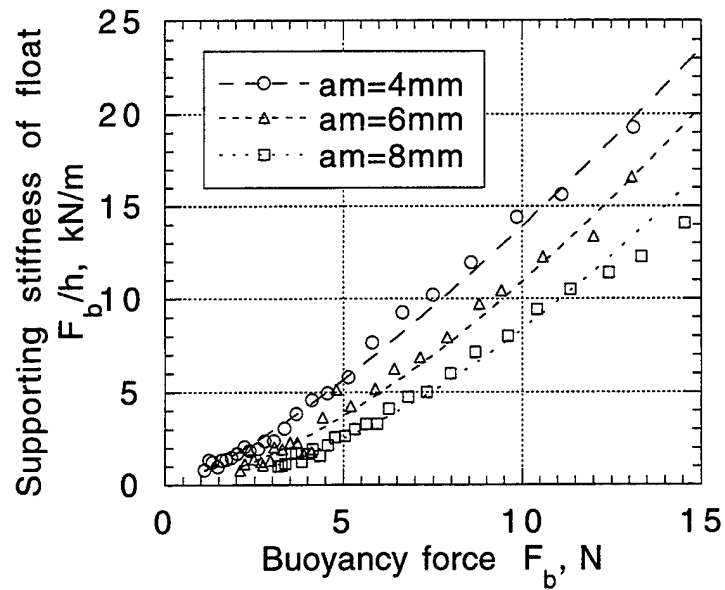
Figure 22 (d)   Experimental results for the variation of stiffness of
the float with distance from the magnet

64

around the maximum magnetic flux through all of the steel components to minimize the magnetic field losses during operation.

Figure 23 is a schematic of an electromagnet type magnetic float polishing apparatus as designed by Dr. Shinmura. It consisted of an electromagnetic coil, low carbon steel core for the conduction of the magnetic field, steel intensifiers to position the magnetic field, and an area designed to place a polishing chamber. The assembly was expected to generate the required field strength, gradient, and the buoyancy force required for polishing the balls. The lower intensifier, just above the magnetic coil, was responsible for the shape and gradients of the magnetic field dispersed through the polishing chamber, greatly influencing the polishing characteristics of the equipment.

Figure 24 is a comparison of a convoluted electromagnetic field intensifier, and a permanent magnet apparatus with alternating N and S poles. While the gap between the two intensifiers determined the field strength, the upper and lower field intensifiers determined the field gradient. Therefore, the shape of the lower field intensifier directly under the polishing chamber determined the field gradients and the strength of the buoyant forces inside the polishing chamber. The initial design of the lower field intensifier resembled somewhat the design of a permanent magnet apparatus with alternating north and south magnetic poles. The similarity showed the intent of the designer in attempting to reflect the field gradients of the permanent magnet equipment into an electromagnetic apparatus. The cut-out sections of the electromagnetic intensifier simulate the change in magnetic field direction inherent in the permanent magnet machine.

Figure 25 shows the magnetic field lines from these two configurations. The electromagnetic intensifier on the left is from the electromagnetic apparatus and generated strong and weak magnetic fields orientated in the same direction. However, the permanent magnet apparatus on the right generated alternating magnetic fields that were restrained to the surface of the magnets, generating extremely high magnetic field gradients. It can also be seen from the figure that in electromagnetic design, the field conducts straight through the polishing chamber, which rests on the north poles, and in a
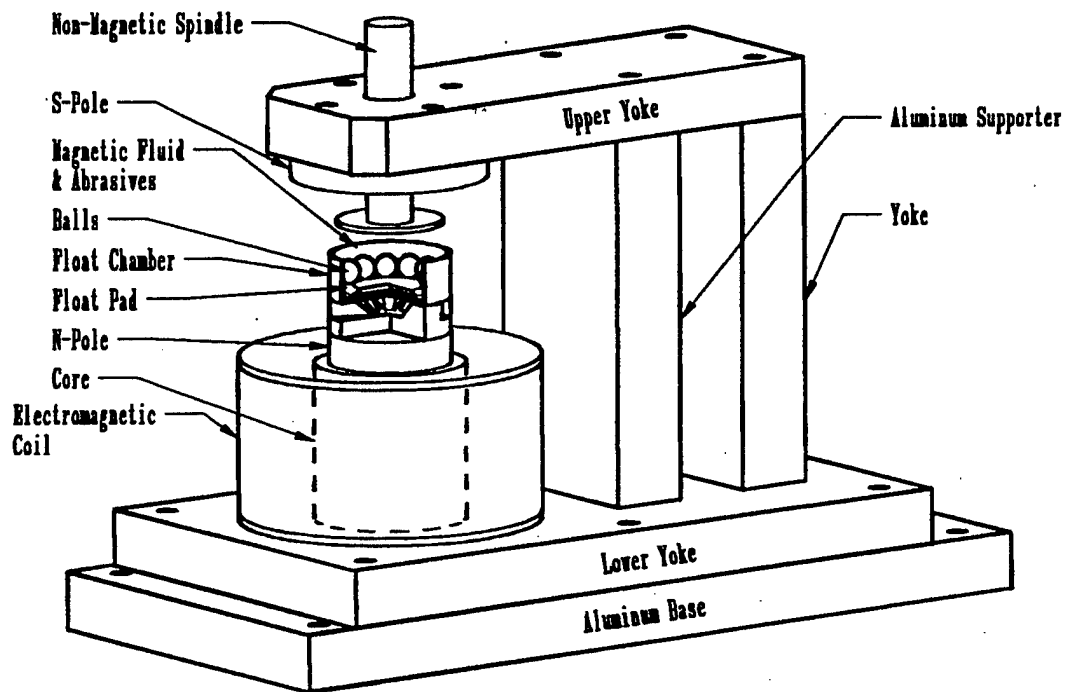
Figure 23   Schematic of an electromagnet type magnetic float polishing apparatus as designed by Dr. Shinmura
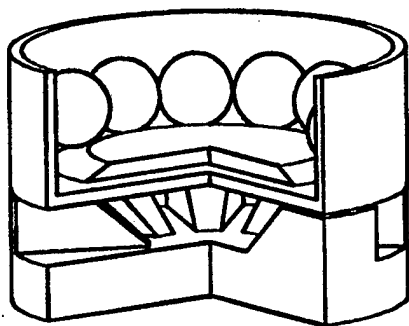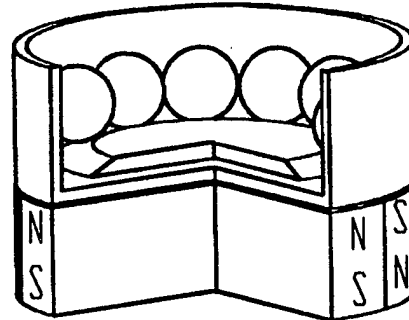
ELECTROMAGNET   PERMANENT MAGNET

Figure 24   Comparison of a convoluted electromagnetic field intensifier, and a permanent magnet apparatus with alternating N and S poles
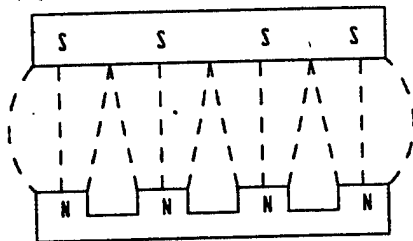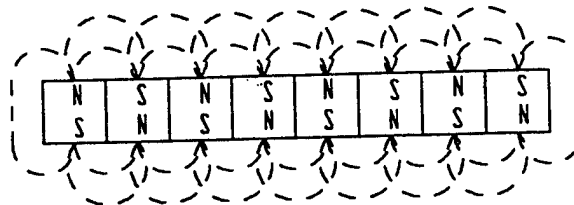
Electromagnet   Permanent Magnet

Figure 25   The magnetic field lines from the two configurations shown in Figure 23

permanent magnet system the magnetic field is reversed within the lower portion of the float polishing chamber. The differences between these two designs offers the possibility of new polishing capabilities.

The design developed by Dr. Shinmura is designated as straight field. This is because magnetic field conduction through the polishing chamber is relatively linear from the lower intensifier to the upper intensifier. The buoyancy force for the straight field design was found to be 3.5 N. This is significantly lower than the 15-20 N obtained with the permanent magnet set up. Also, at these low values of buoyancy forces, the removal rate was also very low. In order to increase the buoyancy forces and hence the removal rates, it was decided to redesign the apparatus using ANSYS analysis.

Figure 26 is the ANSYS model for the straight field electromagnetic apparatus. Figure 27 shows the distribution of the magnetic flux density B in the apparatus. It can be seen that the magnetic flux density in the float chamber near the balls is 0.18 to 0.2 T. It was felt that the low field intensity in the polishing region was due to the large air gap between the poles of the magnet. In order to reduce this, the upper pole was brought down and around the outside of the polishing chamber, yielding a ring pole arrangement. Figure 28 is a schematic of the ring pole design when a ring envelopes the circumference of the float chamber. The ring pole design is idealized as two conductors approaching the center core from each side. This geometry approximates the actual geometry of a circular ring around the central magnetic core.

Figure 29 shows the ANSYS model of the ring pole design. Figure 30 shows the distribution of magnetic field intensity B in the apparatus. It can be seen that the maximum flux densities in the working region of the float chamber are significantly higher (1.2-1.8 T) as compared to the straight field (0.18 to 0.2 T). Since the buoyancy force is proportional to both the intensity and the gradient of the magnetic field, ring pole arrangement must yield higher forces. In fact, it was found that with this arrangement, the buoyancy force was close to 10 N, yielding a three fold increase in force. The ring pole design with zero intensifier gap showed the most promise for efficient and geometrically acceptable polishing process. Thus ANSYS simulation
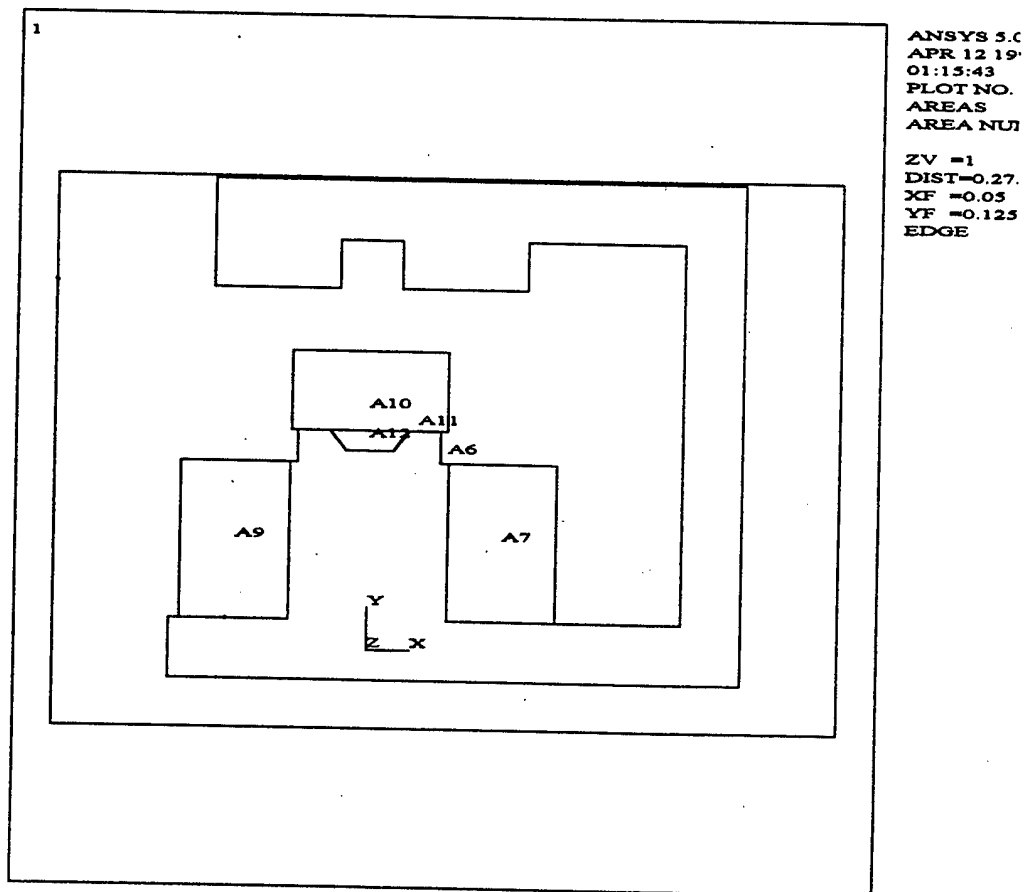
Figure 26   ANSYS model for the straight field electromagnetic magnetic float polishing apparatus

Figure 27   ANSYS contour map of magnetic field B for straight field magnetic float
polishing apparatus design
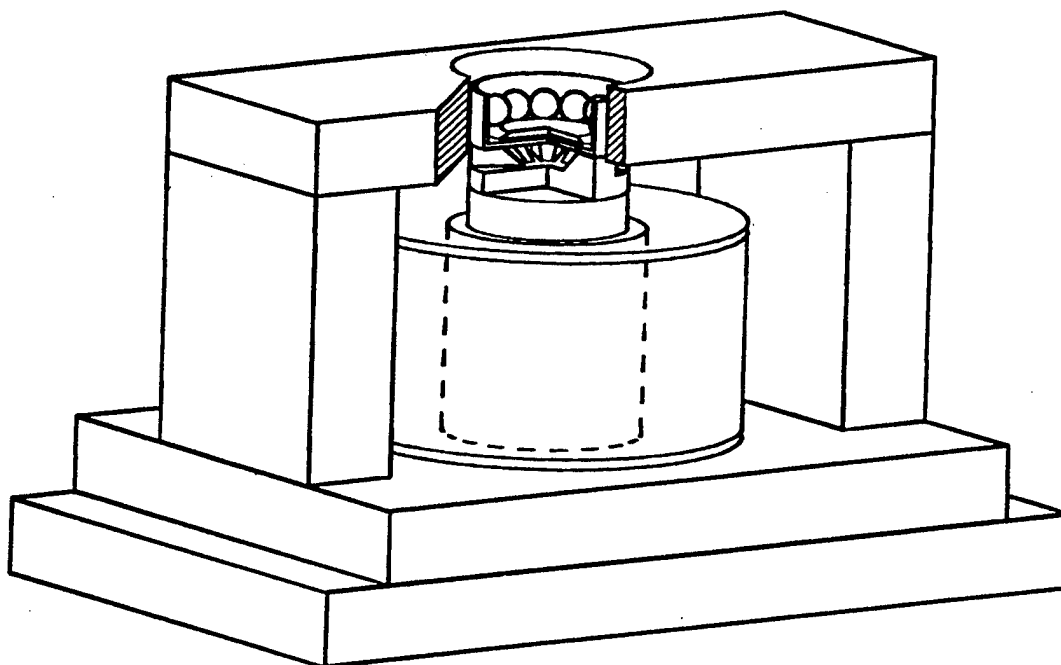
Figure 28   Schematic of the ring pole design when a ring envelopes the circumference
            of the float chamber
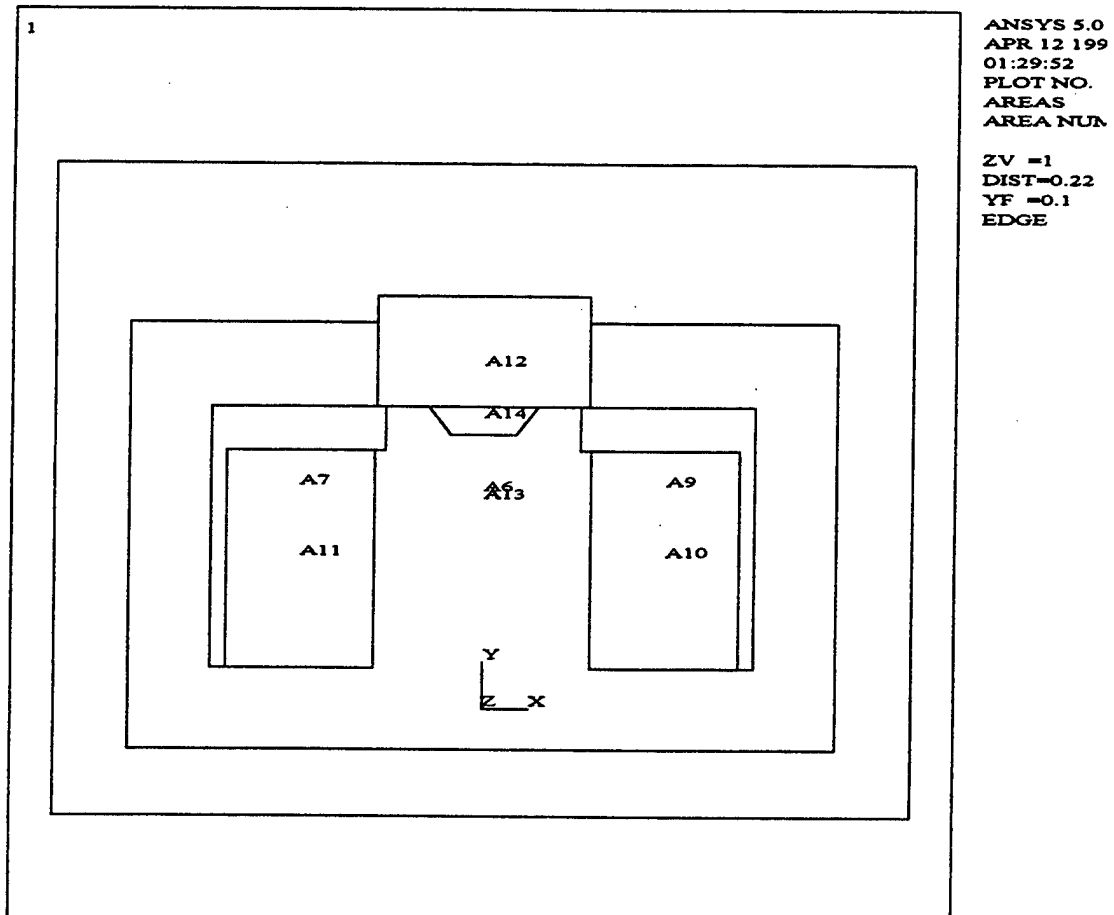
Figure 29   ANSYS model of the ring pole design

```
ANSYS 5.0
SEP  8 1994
23:32:30
NODAL SOLUTION
STEP=2
SUB =1
TIME=2
BSUM    (AVG)
SMN =0.001008
SMX =1.811
        0.001008
        0.202148
        0.403288
        0.604428
        0.805568
        1.007
        1.208
        1.409
        1.61
        1.811
```
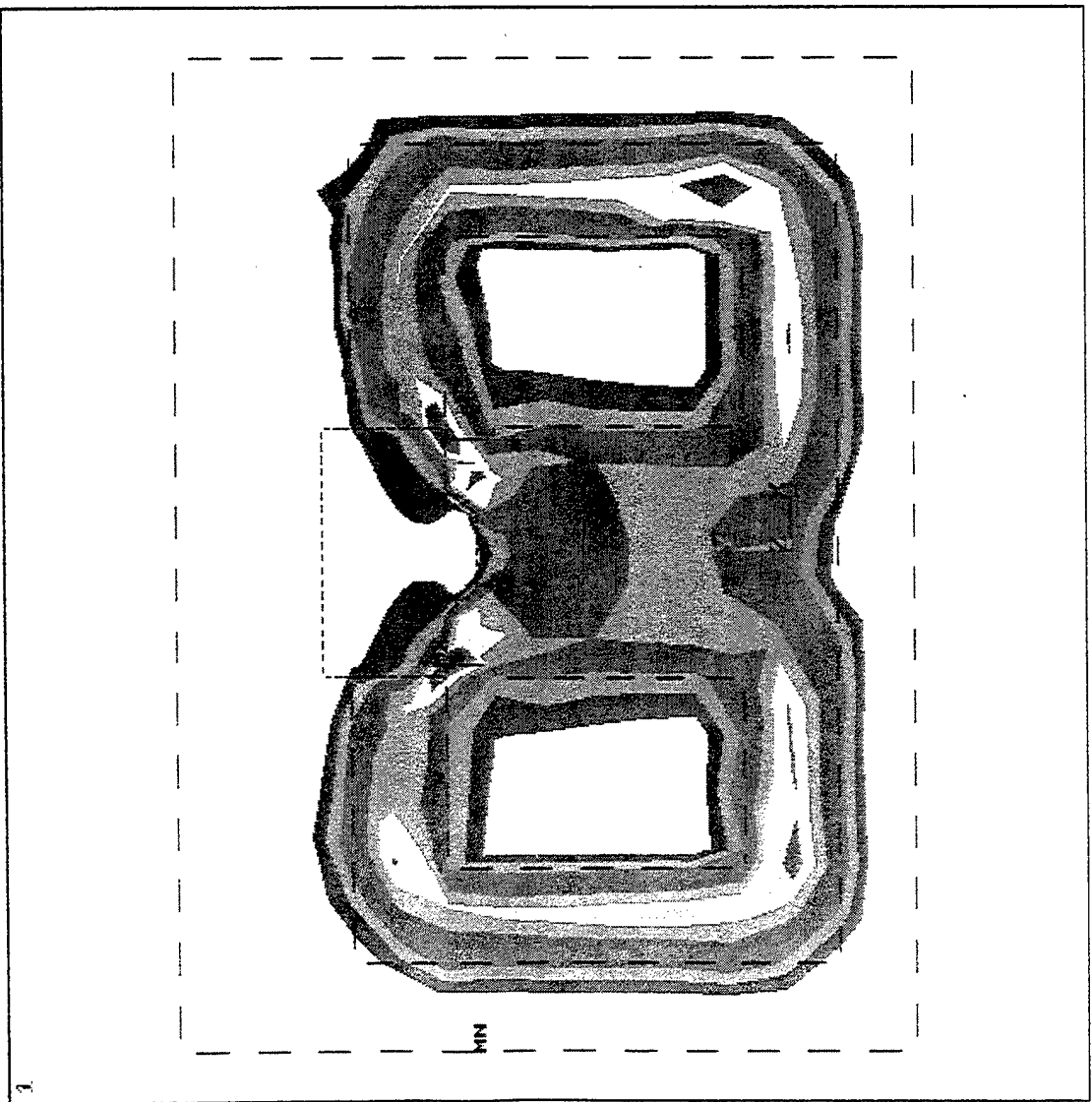
Figure 30   ANSYS contour map of magnetic field B for ring pole design

73

facilitated in the design modification of the permanent magnet float polishing apparatus. In fact, the modified design gave material removal rates higher than the permanent magnet type apparatus. Work is in progress to explore the capabilities of this apparatus.

As seen earlier, the convoluted design of the lower intensifier (with cut-out sections) gave raise to alternating strong and weak the magnetic field. This caused the ball to experience alternating high-low force as it revolves around the chamber, which gives raise to vibration of the ball and float. This vibration was detrimental to ball sphericity. It should be noted that this variation of the magnetic field is also the feature of the permanent magnet apparatus (Figure 21). However, in the permanent magnet apparatus, these variations were restricted to a region very close to the magnets and were not visible above the float. Also, the magnet size was usually kept on the order of the ball diameter so that the effect of variations was minimized. On the other hand, in the electromagnet machine due to the placement of the poles - one below the polishing chamber and other above it, these variations will always be felt by the balls. However, since the ring pole design produced field gradients, the convoluted lower intensifier was not necessary for this design. Hence, a lower intensifier without the cut-outs was used. This gave uniform forces on the ball all around the chamber. Hence, the ring pole design should also yield better sphericity. Details of the various design simulations performed are given in Appendix B (under separate cover) and in Mr. Fox, Mr. Agrawal, and Mr. Dock's M.S. theses and Mr. Raghunandan's work.

2.6 MICRO-MECHANISMS OF MATERIAL REMOVAL AND SURFACE GENERATION IN POLISHING

We have made significant contributions toward an understanding of the micro-mechanisms of material removal and surface generation in finishing of advanced ceramics and glasses. In developing plausible mechanisms, we made an attempt to delineate the failure mechanisms operable in polycrystalline ceramics and glasses versus the metals. This was necessary because of the significant differences in the nature of bonding, microstructure and the tribochemistry, and, flaws generated during

processing of these materials and their consequent effect on the failure mechanisms associated. For example, metals are fully dense crystalline materials with an orderly arrangement (both long and short range) of atoms in all directions. Plastic deformation, instead of brittle fracture, is by far the predominant mode of failure in these materials. Glasses, in contrast, are non-crystalline (or amorphous) and respond intermediately between a liquid and a solid, i.e. at room temperature they behave in a brittle manner but above the glass transition temperature in a viscous manner. Ceramics, though mostly crystalline, are different in the nature of bonding. For example, metallic bonding, in the case of metals; no long range order in the case of glasses; and ionic and/or covalent bonding in ceramics.

Since ceramics are processed from powders using sintering, hot-pressing, or hot-isostatic pressing, they are less than theoretically dense. This results in some inherent porosity in the microstructure. Also, the grain boundaries generally consist of a weak, glassy phase. All these factors affect the strength and failure (deformation/fracture) behavior of these materials. Grain dislodgement, viscous flow at the grain boundaries, and microfracture of the crystals may be the predominant modes of failure rather than plastic deformation. Also, under the high pressures and temperatures generated at the contacting points during polishing, mechano-chemical effects can play an important role in the material removal. In this investigation, the effects of these factors were carefully considered in the development of a mechanistic model of the process. While plastic deformation was feasible at high temperatures and/or under high hydrostatic pressures, the wide range of defect structures present at various levels in most ceramics tend to favor microfracture, grain dislodgement, etc. Further, in ceramics containing a glassy phase at temperatures higher than the glass transition temperature, viscous flow of the glassy phase takes place. Since the glassy phase is present at the grain boundaries, this can cause grain boundary sliding.

As pointed out earlier, some researchers consider the mechanism of material removal in grinding at low depths of cut due to plastic deformation of the ceramic. However, the arguments are somewhat circuitous and the evidence is far from direct. With this in view we have examined a range of glasses and ceramic materials to investigate the mechanism of material

removal. Figure 31(a) is a glass surface ground on a Rank-Pneumo sub-micron diamond grinding machine (ASG 2500) using a diamond grinding wheel. The surface finish was considered excellent and of optical quality. To the naked eye, the surface appeared highly polished and smooth. The surface roughness was 42.6 nm (rms). However, on careful examination in the environmental scanning electron microscope (ESEM) which neither required the sample to be conductive nor a conducting coating for non-conducting materials, we found the surface to be far from smooth. We observed several pits and parallel grooves corresponding to the feed marks of the grinding wheel made during the cross feed of the diamond wheel past the glass surface [Figure 31(a)]. At higher magnification, it appears that some of the pits were filled by material [Figure 31(b)] smeared over them. The visco-plastic nature of the glass may play an important role in the material removal mechanism. We then examined the surface using the ZYGO laser interference microscope using a 20 x Fizeau lens. The peak to valley distance was about 306 nm and the rms finish was about 32.23 nm.

Figure 32 (a) is a scanning electron micrograph of a glass ball polished by magnetic float polishing. The surfaces of these balls were very smooth but in some areas pits were formed by microfracture [Figure 32 (b)]. Note also the fine scratches, the nature of which would be of interest in the analysis. Figure 33(a) is a scanning electron micrograph of an aluminum oxide ball polished by conventional methods. It can be seen that the finished surface contains several pits. Figure 33(b) is a scanning electron micrograph of a pit at higher magnification showing dislodgement of individual crystallites. In addition, submicron sized scratches in random directions can be seen. These appear to be responsible for the finishing of the balls while the formation of large pits appear to be responsible for material removal. However, once these pits were formed, the polishing process for finishing required that all these pits be removed which would be a time consuming process involving several hundred hours as currently experienced. It may be necessary to investigate alternate strategies for obtaining the required finish by not damaging the surfaces so severely by the formation of a multitude of pits during rough polishing.

Figure 31 (a)   ESEM micrograph of a ground glass surface
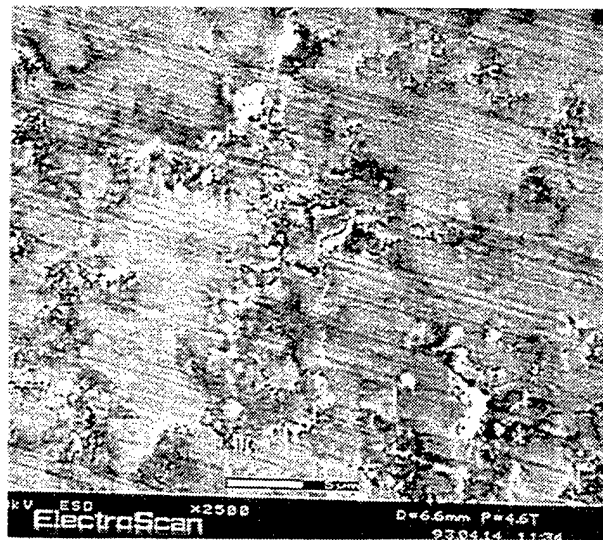
Figure 31 (b)   ESEM micrograph of the sample in Figure 31 (a) at higher magnification, showing some of the pits filled by material
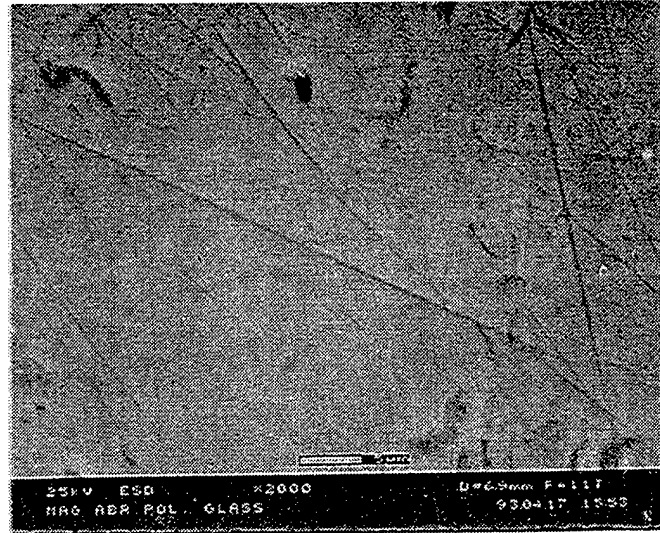
Figure 32 (a)   SEM micrograph of a glass ball polished by MFP
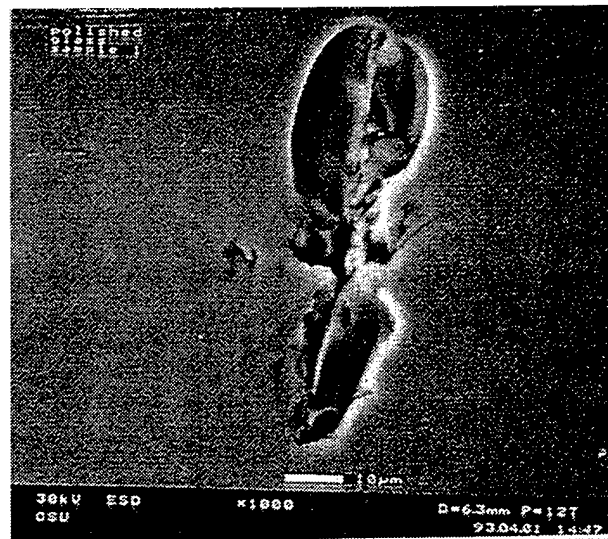
Figure 32 (b) SEM micrograph of sample in Figure 32 (a) showing pits formed by microfracture
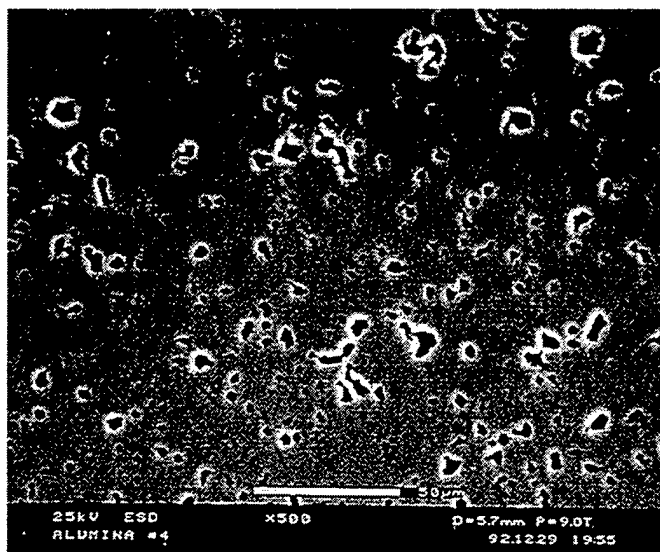
Figure 33 (a)   SEM micrograph of an aluminum oxide ball polished by conventional methods
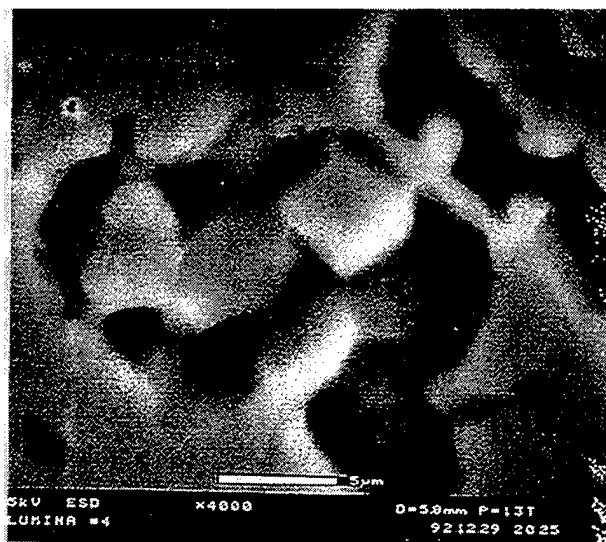
Figure 33 (b)   SEM micrograph at higher magnification of a pit seen in Figure 33(a) showing dislodgement of individual crystallites

The smooth surfaces obtained in grinding Si_3N_4 with fine diamond abrasive was interpreted by some researchers as the change in the mechanism of material removal from brittle to ductile. It should, however, be noted that Si_3N_4 ceramics have a glassy phase and the smooth surface could due to viscous flow of the glassy phase on the surface of the ceramic. In fact, when examined in the electron microscope, this layer appeared as a transparent layer. Alternately, the smooth surfaces produced were a result of chemo-mechanical polishing as will be shown in the next section. Details of this work are given in Appendix F (under separate cover).

2.7 CHEMO-MECHANICAL POLISHING OF Si_3N_4 WITH Cr_2O_3 ABRASIVE

Conventional material removal of advanced ceramics using abrasives harder than the work material involves indentation and abrasion leaving scratches, pitting, and fine cracks on the surface [24]. In contrast, chemo-mechanical polishing (also termed mechano-chemical polishing) depends on the chemical interaction between the abrasive, the work material, and the environment [25]. Oftentimes, the abrasive used is of the same hardness or even softer than the work material since hardness is really of no consequence in this type of material removal with chemical activity. Consequently, no scratching or groove formation is expected with these abrasives, leading to a very smooth surface. Hence, for finishing advanced ceramics, chemo-mechanical action is rather an attractive alternate proposition, especially during the final stages of polishing.

The chemo-mechanical process initiates a chemical reaction between a given abrasive and the work material. The process produces a weaker reaction product compared to either the abrasive or the work material. The environment used can facilitate the chemical action. The reaction product thus formed is brittle and subsequently removed by the abrasive action. This results in production of a smooth surface. However, the presence of defects, such as pits, grooves from an earlier semifinishing operation can still exist in the final operation unless all the defects are removed by this operation. Or, alternately, these defects could be gradually minimized as one progresses from roughing to semifinishing to finishing. Hence, the history of polishing

80

would be a very important consideration in the final finishing condition of advanced ceramics.

Several studies were reported in the literature on the various aspects of finishing Si_3N_4 in view of this material's potential for advanced structural applications, such as parts for gas turbine, bearings for high-speed, and high-precision spindles. These studies have indicated that oxidation of Si_3N_4 was the crucial step in the tribological and tribo-chemical behavior of this material. The results also indicated the formation of an amorphous silica on the surface when Si_3N_4 was polished in air and the formation of a hydrated silica layer when polished in water. However, no evidence of compound formation of Si_3N_4 with Cr_2O_3 abrasive was reported. Consequently, the role of Cr_2O_3 was considered as one of a catalyst rather than direct involvement in the chemical reactions. We found new evidence that shows conclusively that Cr_2O_3 did participate in the chemo-mechanical polishing of Si_3N_4 forming chromium nitride and chromium silicate, thus establishing the role of Cr_2O_3 not as a mere *catalyst* but as actively taking part in the chemical reactions during chemo-mechanical polishing. We collected the wear debris generated during polishing, separated and analyzed it using an ABT 32 scanning electron microscope (SEM) with a Kevex energy dispersive X-ray microanalyzer (EDX) and a Seimens low angle X-ray diffractometer (XRD). The energy dispersive X-ray (EDX) analysis (i.e. Si and Cr maps) with the SEM images of some individual wear particles generated during polishing of Si_3N_4 with Cr_2O_3 abrasive showed the presence of both chromium and silicon in the same area as the wear particle suggesting the possibility of chromium silicate formation (Figure 34). The analysis of the wear debris using the X-ray diffractometer (XRD) clearly showed the formation of chromium nitride and chromium silicate in addition to SiO_2 and Cr_2O_3 (Figure 35).

Based on the experimental evidence, a new model of chemo-mechanical polishing of Si_3N_4 in air and in water environments with Cr_2O_3 abrasive was developed. This model was based on the formation of such reaction products as chromium silicate and chromium nitride in addition to the formation of a silica layer on the Si_3N_4 surface as well as the gaseous reaction products, such as ammonia (in water) and nitrogen (in air). For the
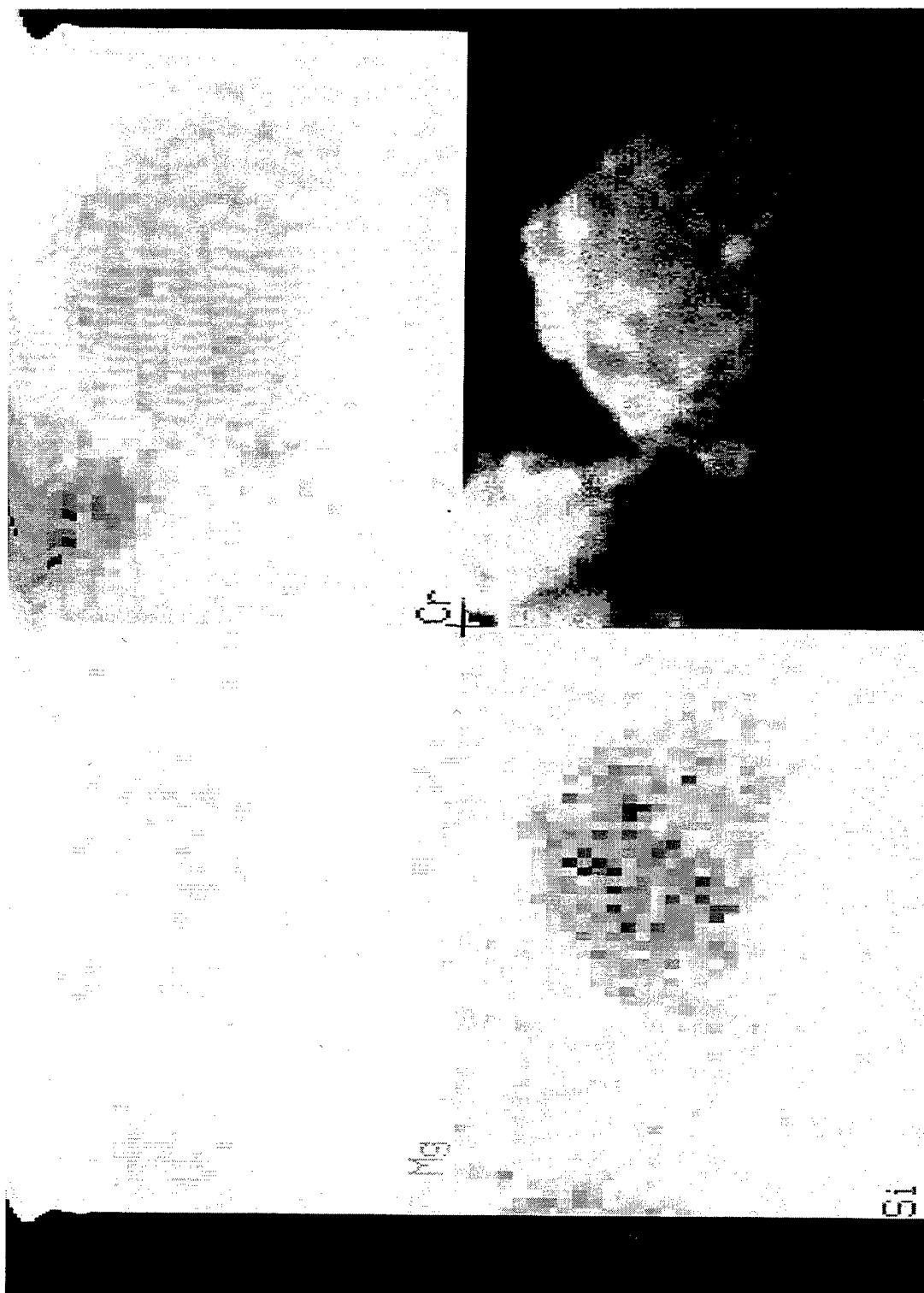
Figure 34   EDX plot of an individual wear particle generator during polishing of Si3N4 with Cr2O3 showing SEM image and Si and Cr maps suggesting the possibility of chromium silicate formation
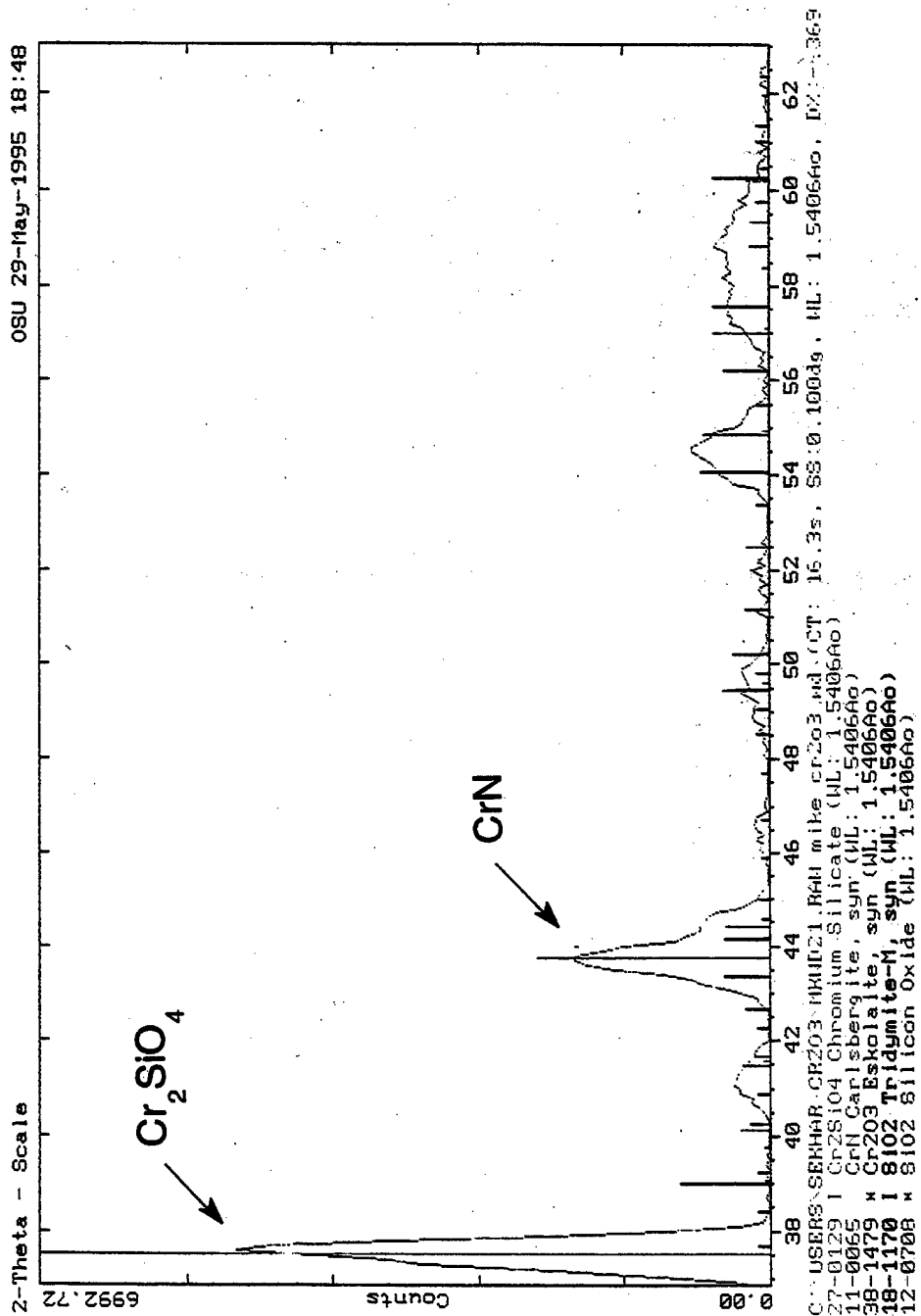
Figure 35   X-ray diffractometer (XRD) plot of wear debris showing the formation of chromium nitride and chromium silicate in addition to SiO_2 and Cr_2O_3

83

chemo-mechanical polishing Si_3N_4 work material with Cr_2O_3 abrasive *in air* [Figure 36 (a)], the reactions that are formed include oxidation of Si_3N_4 to form a silica layer on the surface and the evolution of nitrogen gas. Other reaction products include the formation of chromium nitride and chromium silicate. For the chemo-mechanical polishing *in water* [Figure 36 (b)], the reactions were essentially the same, except in this case, the adsorption of hydroxyl ions to the surface of Si_3N_4 and oxidation of the surface takes place, which forms initially a silica layer which further gets oxidized to form a hydrated silica ($SiOH_4$) layer. When the nitrogen ions get an opportunity to pair up with hydrogen ions present in water, they form ammonia gas (instead of nitrogen gas, as in the case of air). The other reaction products are the same, namely, chromium nitride and chromium silicate. The implication of gaseous reaction products in the generation of pore-free surface in finishing is also pointed out.

In summary, the function of Cr_2O_3 in chemo-mechanical polishing of Si_3N_4 may be considered as three fold. First, it enhances the oxidation kinetics by forming chromium nitride, facilitating the formation of the silica layer. Second, it increases the nitrogen ion residence time, which ultimately reduces the formation of surface porosity, which is crucial in achieving a good surface without stress concentrations. Third, it reacts with the silica layer to form chromium silicate, which gets removed during the subsequent mechanical abrasion. Details of this work are given in Appendices I and J (under separate cover) and in the M. S. thesis of Mr. Bhagavatula.

2.8 THERMAL MODEL FOR MAGNETIC FIELD ASSISTED POLISHING OF CERAMICS

In the determination of the feasibility of chemical reaction products that may form in chemo-mechanical polishing, both flash temperature and flash time have to be considered. The flash temperatures can be used as a basis for thermodynamic analysis (free energy of formation). For the feasibility of formation of a particular chemical reaction between the work material, abrasive, and the environment, flash times are needed to investigate the kinetics. To address this, we have developed a thermal model for the
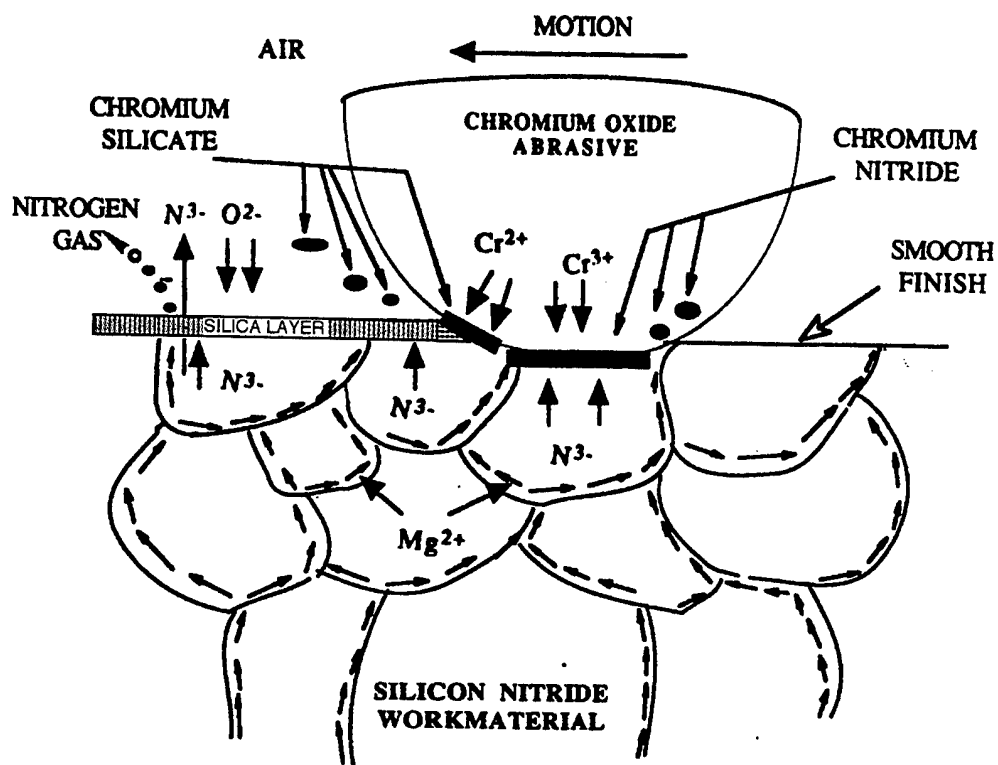
Reactions occuring in the chemo-mechanical polishing of silicon nitride with chromium oxide abrasive in air

$$Si_3N_4 + 3 O_2 \rightarrow 3 SiO_2 + 2 N_2 \uparrow$$

$$Si_3N_4 + 2 Cr_2O_3 \rightarrow 3 SiO_2 + 4 CrN$$

$$4 Si_3N_4 + 2 Cr_2O_3 + 9 O_2 \rightarrow 12 SiO_2 + 4 CrN + N_2 \uparrow$$

$$2 Cr_2O_3 + 2 SiO_2 \rightarrow 2 Cr_2SiO_4 + O_2 \uparrow$$
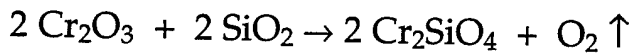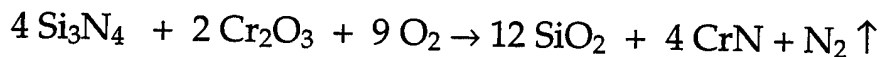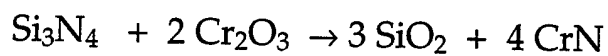
Figure 36 (a)   Schematic of the model for chemo-mechanical polishing Si_3N_4 work material with Cr_2O_3 abrasive in air

Reactions occuring in the chemo-mechanical polishing of silicon nitride with chromium oxide abrasive in water

$$Si_3N_4 \ + \ 6\,H_2O \rightarrow 3\,SiO_2 \ + \ 4\,NH_3 \uparrow$$

$$3\,SiO_2 \ + \ 6\,H_2O \rightarrow 3\,Si(OH)_4$$

$$Si_3N_4 \ + \ 2\,Cr_2O_3 \rightarrow 3\,SiO_2 \ + \ 4\,CrN$$

$$Si_3N_4 \ + \ Cr_2O_3 \ + \ 3\,H_2O \rightarrow 3\,SiO_2 \ + \ 2\,CrN + 2\,NH_3 \uparrow$$

$$2\,Cr_2O_3 \ + \ 2\,SiO_2 \rightarrow 2\,Cr_2SiO_4 \ + \ O_2 \uparrow$$
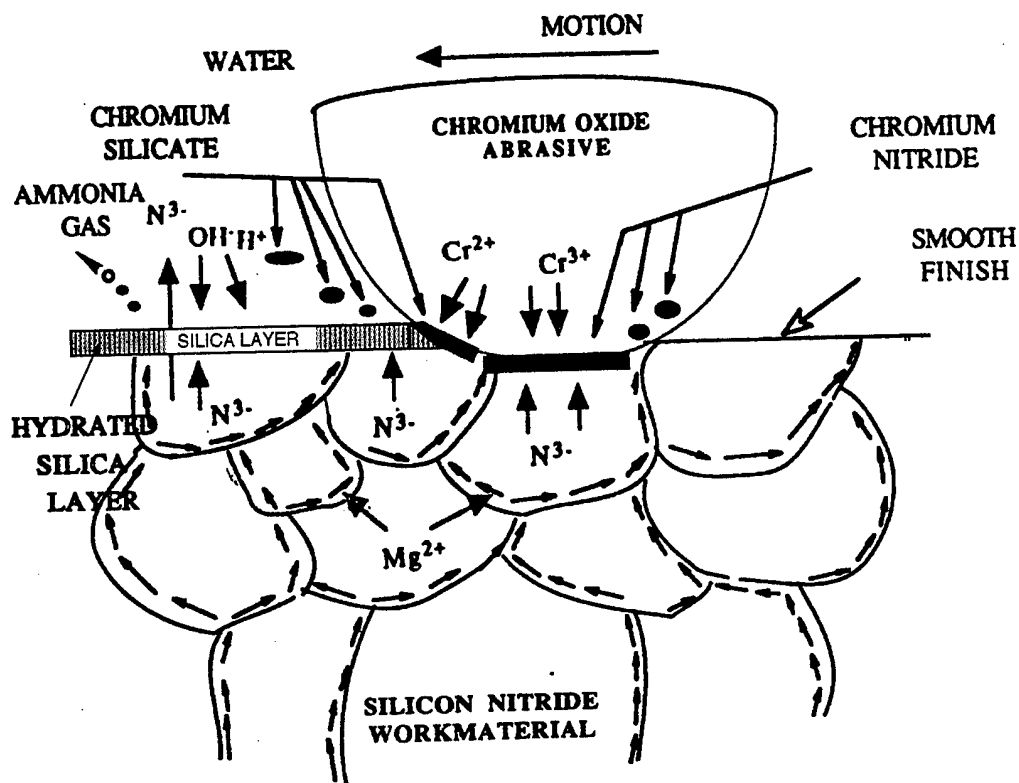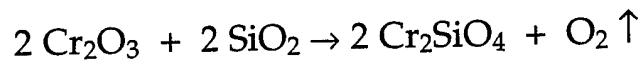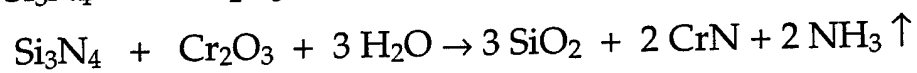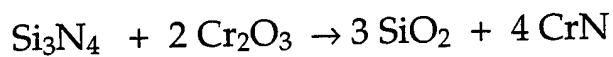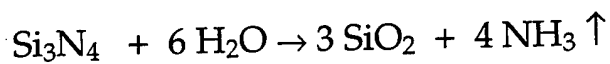
Figure 36 (b)   Schematic of the model for chemo-mechanical polishing Si3N4 work material with Cr2O3 abrasive in water

calculation of the flash temperatures generated at the contact points in the magnetic float polishing process. The heat source between the ball and the shaft (contact area) in magnetic float polishing, where much of the material removal takes place, was approximated to a disc. The disc plane heat source was considered as a combination of a series of concentric circular ring heat sources with different radii. Each ring in turn was considered as a combination of a series of infinitely small arc segments and each arc segment as a point heat source. We applied Carlsaw and Jaeger's classical moving heat source theory to solve the circular ring heat source problem and finally the disc heat source problem. We calculated the flash temperatures, flash times, and temperature distribution between the balls and the shaft of the polishing apparatus using this technique.

Figure 37 shows the results of the calculation of temperature rise on the surface along the X-axis (Y=0 and z = 0) for V = 2-6 m/sec. Figure 38 shows the temperature rise on the surface for V = 5 m/sec for different X and y (z = 0). Figure 39 shows isotherms of the temperature on the surface which can be used to calculate the flash times at different flash temperatures. Each involves the area where the temperature rise is higher than that of the isothermal. The length of the area enclosed the isotherms in the X-direction can be estimated from this figure. Based on this, the flash times at relevant flash temperatures can be obtained. Flash temperatures generated can be as high as $800^{\circ}C$, depending on the sliding velocity. For a sliding speed of 1 m/sec, flash temperatures are around $200\ ^{\circ}C$ and increase with an increase in sliding speed. Also, the flash time decreases with increase in the flash temperature. For example, for a flash temperature higher than $100\ ^{\circ}C$, the flash time is 4.87 μsec. For a flash temperature higher than $500\ ^{\circ}C$, the flash time is less than one μsec. While flash temperatures can be used as a basis for thermodynamic analysis (free energy of formation) for the feasibility of a particular chemical reaction that can be formed between the work material, abrasive, and the environment, flash times are needed to investigate the kinetics. Details of this work are given in Appendix K and L, (under separate cover) and in Mr. Bhagavatula's M.S. thesis.
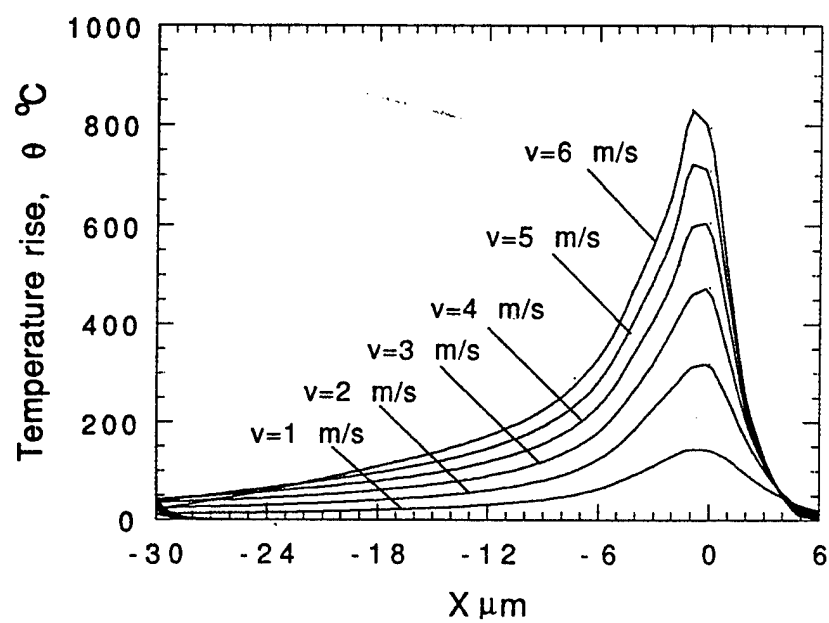
Figure 37   Plot of temperature rise on the surface along the X-axis (Y=0 and z = 0) for various sliding speeds (v = 2-6 m/sec)
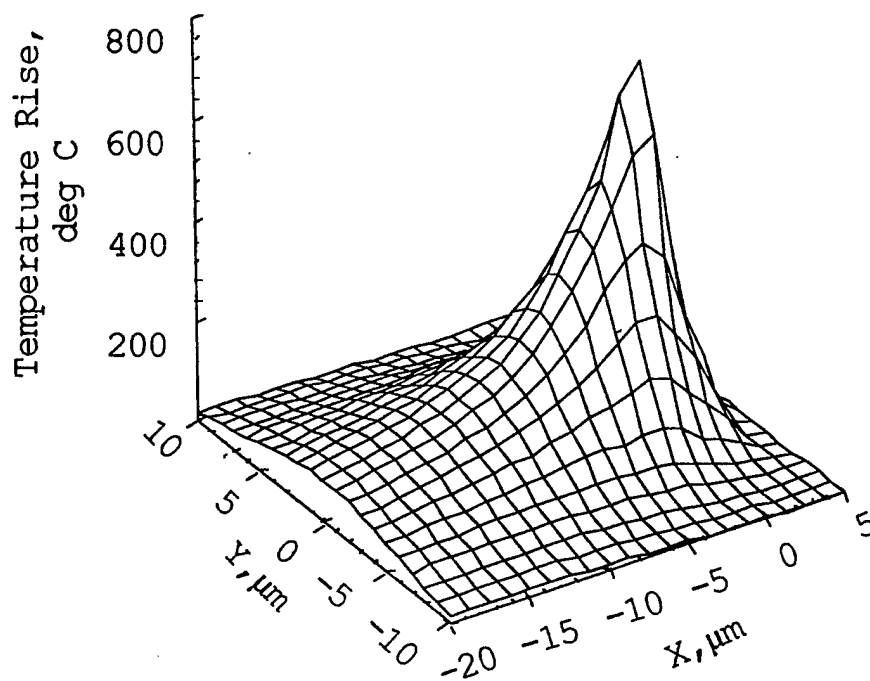
Figure 38   Temperature rise on the surface for v = 5 m/sec for different X and Y
(z=0)
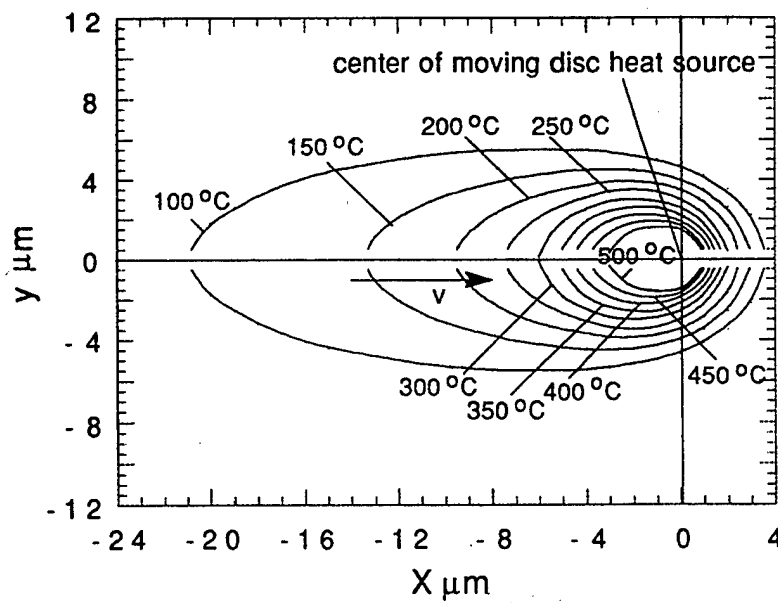
Figure 39   Isotherms of temperature on the surface for v = 5 m/sec to calculate
the flash times at different flash temperatures

2.9 RESEARCHERS INVOLVED IN ADVANCED MANUFACTURING TECHNOLOGIES

Several graduate students, including, M. Raghunandan, Michael Fox, Kishore Agrawal, Mathew Dock, Sanjai Kesavan, Vissa Chandramouli, Jiang Ming, Sekhar Bhagavatula, and Sujatha Iyengar were involved in various aspects on this project. Except for M. Raghunandan, who is completing his Ph.D, all the other students completed their M.S degrees. Michael Fox is continuing with his Ph.D. Many undergraduates were also involved part time on this project in the last three years. Also, several post-doctoral fellows and visiting faculty were involved in this project. They include Dr. T. Shinmura of Utsunomia University, and Dr N. Umehara of Tohoku University, both from Japan; Prof.Zhen Bing Hou of China; Dr. Ali Noori Khajavi (a Ph.D from OSU); and Dr. T. R. Ramamohan of IIT, Bombay, India. Michael Fox received the Graduate Research Excellence award from OSU for his M.S. thesis. Also, Dr. Umehara was selected as an Outstanding Young Manufacturing Engineer in 1995 by the Society of Manufacturing Engineers (SME) and F.W. Taylor Medal of CIRP in 1996 for his work on magnetic float polishing of ceramics.

2.10. INFRASTRUCTURE DEVELOPMENT

OSU has committed substantial resources for the acquisition of state-of-the art research facilities (equipment and instrumentation) in advanced manufacturing technology and non-destructive inspection (NDI) techniques as a result of the ARPA Ceramic Bearing Technology Program. In the manufacturing processes area alone (Komanduri), this includes Rank-Pneumo ASG 2500 submicron diamond turning and grinding machine with three grinding spindles; Hardinge precision lathe; Bridgeport CNC Milling Machine; PI precision air bearing spindle; Nikon optical differential interference microscope; ABT 3200 scanning electron microscope with KEVEX X-ray microanalyzer; ESEM environmental scanning electron microscope with Kevex X-ray microanalyzer; μ-Raman spectrometer; Siemens low angle X-ray diffractometer; ZYGO laser interference microscope; and Rank-Taylor

Hobson's Talysurf, TalyStep, and TalyRond. Our students have designed and built experimental apparatuses for magnetic float polishing of ceramic balls, magnetic abrasive finishing of ceramic rollers, and magnetic abrasive finishing of internal surfaces. In addition, we have a range of experimental facilities for low pressure diamond synthesis (microwave assisted CVD, combustion synthesis, hot-filament CVD, and laser assisted microwave CVD), all designed and built by our students; a range of industrial lasers (Class 4) including Control Data Laser 400 W Nd:YAG laser, a 1500 W CO_2 laser, and Lambda Physik excimer laser (XeF) for laser assisted machining of advanced ceramics, metals, plastics, and composites.

2.11 PUBLICATIONS AND THESES

2.11.1 Publications

The following is a partial list of technical publications as a result of work performed on this project. Several other papers are currently under preparation and will be sent for publication soon. It is hoped that this information will serve as a technology transfer to industry for implementation.

1. Komanduri, R., and T. R. Ramamohan, "On the Mechanisms of Material Removal in Fine Grinding and Polishing of Advanced Ceramics," a keynote paper presented at the 7th Int. Conf. on Production/Precision Engineering, Chiba, Japan (September 15-17,1994) and published in Advancement of Intelligent Production (JSPE Publication Series No.1) by Elsevier Science B.V. (1994) K-38-K51

2. Fox, M., K. Agrawal, T. Shinmura, and R. Komanduri, "Magnetic Abrasive Finishing of Rollers," Annals of CIRP, 43/1, (1994) 181-184

3. Bhagavatula, S. R., and R. Komanduri, "On Chemo-Mechanical Polishing of Silicon Nitride with Chromium Oxide Abrasive," (Ref. 3 and 4 as one paper) accepted for publication in Philosophical Magazine (1996)

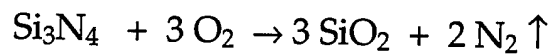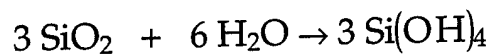4. Bhagavatula, S. R., and R. Komanduri, "On the Mechanism of Chemo-Mechanical Polishing of Silicon Nitride with Chromium Oxide Abrasive," (Ref. 3 and 4 as one paper) accepted for publication in Philosophical Magazine (1996)

5. Umehara, N., and R. Komanduri, "Magnetic Fluid Grinding of HIP-SI_3N_4 Rollers," J. of Wear, 192, (1996), 85-93

6. Umehara, N., "Magnetic Fluid Grinding - a New Technique for Finishing Advanced Ceramics," Annals of CIRP, 43/1, (1994) 185-188

7. Raghunandan, M., N. Umehara, and R. Komanduri, "On the Possibility of Chemo-Mechanical Polishing of Silicon Nitride," Proc. of the Symposium on Tribology in Manufacturing, ASME/STLE Tribology Conference, Lahaina, Maui, Hawaii (1994) 81-89. Also, accepted for publication in Trans. ASME , J of Tribology (1995)

8. Umehara, N., T. Shinmura, and R. Komanduri, "Magnetic Field Assisted Polishing - A Review," paper under preparation (1995)

9. Umehara, N. and R. Komanduri, "On the Material Removal Mechanisms in Polishing of Advanced Ceramics," paper presented at the Annual Meeting of the Japan Society of Tribologists (1994)

10. Raghunandan, M., N. Umehara, A. Noori-Khajavi, and R. Komanduri, "Magnetic Float Polishing of Ceramics," accepted for publication in Trans ASME, J of Engg. for Industry (1995)

11. Iyengar, Sujatha and R. Komanduri, "A Review of Magnetic Fluids," to be submitted for publication (1995)

12. Hou, Zhen Bing and R. Komanduri, " On the Thermal Aspects of Magnetic Float Polishing (MFP) of Ceramic balls," submitted for publication Trans ASME, J of Tribology (1996)

13. Zhen Bing Hou, Bhagavatula, S. R., and R. Komanduri, "A Thermal Model of Magnetic Abrasive Finishing (MAF) of Ceramic Rollers," submitted for publication Trans ASME, J of Tribology (1996)

14. Raghunandan, M., and R. Komanduri, "Finishing of Silicon Nitride Balls," submitted for publication Trans ASME, J. of Manuf. Engg. and Sci., (1996)

15. Jiang Ming, M. Raghunandan, and R. Komanduri, "Monitoring of Magnetic Float Polishing Process Using a Sound Sensor," to be submitted for publication (1995)

2.11.2 <u>M.S. and Ph.D Thesis</u>

The following is a list of candidates who submitted (or will submit) their M.S. or Ph. D theses as a result of working on this project. Three new students, Mr. Asif Patel, Jiang Ming and Brian Perry have joined the group. They are working in the areas of polishing of small size silicon nitride balls, finishing of larger size balls and in-process monitoring of magnetic float polishing equipment using sound and force sensors, and polishing using an eccentric system.

1. Raghunandan, M.,"Magnetic Float Polishing of Silicon Nitride Balls," Ph.D Thesis, Oklahoma State University, Stillwater, OK (to be completed in Summer 1996)

2. Bhagavatula, S. R., "Chemo-Mechanical Polishing of Silicon Nitride with Chromium Oxide Abrasive," M.S. Thesis, Oklahoma State University, Stillwater, OK (1995)

3. Dock, M, "Electromagnetic Float Polishing of Ceramic Balls for Bearing Applications" (1994), M.S. Thesis, Oklahoma State University, Stillwater, OK (1995)

4. Agarwal, K.,"Magnetic Abrasive Finishing of Nonmagnetic Rollers", M.S. Thesis, Oklahoma State University, Stillwater, OK (1994)

5. Fox, M., "Magnetic Abrasive Finishing of Non-ferromagnetic Rolling Elements," M.S. Thesis, Oklahoma State University, Stillwater, OK (1994)

6. Kesavan, S. R., "An *In Situ* Stage for Scratching of Glass Inside ESEM," M.S. Thesis, Oklahoma State University, Stillwater, OK (1994)

7. Chandramouli, V., "An Analysis of Indentation of Brittle Materials," M.S. Thesis, Oklahoma State University, Stillwater, OK (1993)

2.12 ACKNOWLEDGMENTS

2.13 REFERENCES

1. Baron, J. M., "Technology of Abrasive Machining in a Magnetic Field," Masino-strojenije, Leningrad (1975) (in Russian).

2. Konovalov, E. G., and F. J. Sakulevich, "Principles of Electro-Ferromagnetic Machining," Naukaitechnika (1974) (in Russian).

3. Sakulevich, F. J., and L. M. Kozuro, "Magneto-Abrasive Machining," Naukaitechnika, Minsk (1978) (in Russian).

4.   Sakulevich, F. J., and L. M. Kozuro, "Magneto-Abrasive Machining of Fine Parts," Vyssaja Skola, Minsk (1977) (in Russian).

5.   Konovalov, E. G., and G. S. Sulev, "Finishing Machining of Part by Ferromagnetic Powder in Magnetic Field," Naukaitechnika (1967) (in Russian)

6.   Mekedonski,. B. G., and A. D. Kotshemidov, "Schleifen im Magnetfeld," Fertigungstechnik und Betrieb, 24, H.4 (1974) 230 - 235

7.   Kato,K., " Tribology of Ceramics ", Wear, 136 (1990)117-133.

8.   Umehara, N, and K. Kato, " Principles of Magnetic Fluid Grinding of Ceramic Balls," Int. J. of Applied Electromagnetics in Materials, 1, (1990) 37-43.

9.   Umehara, N., and K. Kato., "A Study on Magnetic Fluid Grinding (1st Report), The Effect of the Floating Pad on Removal Rate of Si3N4 Balls," J. of Japan Society of Mechanical Engineers, 54, 503, (1988)1599-1604. (in Japanese)

10.   Umehara, N., and K. Kato, "Hydro-Magnetic Grinding Properties of Magnetic Fluid Containing Grains at High Speeds," J. of Magnetism and Magnetic Materials, 65 (1987) 397-400

11.   Umehara, N., K. Kato, and M. Takekoshi, "The Effect of Supporting Stiffness of a Float on Finishing Characteristics," to be published in the Proc.of the Annual Meeting of the Magnetic Fluid Research Society (1993) (in Japanese)

12.   Tani, Y., and K. Kawata/ Nakagawa, "Development of High Efficient Fine Finishing Process using Magnetic Fluid," Annals of CIRP, 33/1 (1984) 217-220

13.   Takazawa, K., T. Shinmura, and E. Hatano, "Development of Magnetic Abrasive Finishing and Its Equipment," MR 83-678. Proc. of the SME'S

12th Deburring and Surface Conditioning Conference, Orlando , Nov 8-10, 1983

14. Takazawa, K., T. Shinmura, and E. Hatano, "Advanced Development of Magnetic Abrasive Finishing and Its Equipment," Proc. of the SME'S Deburring and Surface Conditioning Conference '85, Orlando , (Sept 23-26, 1985) 30-46

15. Shinmura, T., K. Takazawa, and E. Hatano, "Study of Magnetic Abrasive Finishing," Annals of CIRP, 39/1 (1990) 325-328

16. Shinmura, T., T. Iizuka, and Y. Shinbo, "A New Process for Internal Finishing of Non-Ferromagnetic Tubing using Rotating Magnetic Field," Trans. NAMRI/SME, XXI (1993) 151-158

17. Childs, T.H.C. and H. J. Yoon, "Magnetic Fluid Grinding Cell Design," Annals of CIRP, 41/1 (1993) 343-346

18. Childs,T. H. C. , S. Mahmood, and H.J. Yoon, "The Material Removal Mechanism in Magnetic Fluid Grinding of Ceramic Ball Bearings," Proc.of I. Mech. E. , 208, No. B1 (1994) 47--59

19. Childs, T.H.C., D.A. Jones, S. Mahmood, K. Kato, B. Zhang, and N. Umehara, "Magnetic Fluid Grinding Mechanics," Wear, 175 (1994) 189-198

20. Rosensweig, R. E.,"Ferrohydrodynamics," Cambridge University Press, Cambridge, U.K. (1985)

21. Umehara, N. K. Kato, and H. Nakano, "Magnetic Fluid Grinding of Ceramic Rollers," Electromagnetic Forces and Applications, Supplement to Volume 2 of the Int. J of Electromagnetics in Materials, (1992) 139-142

22. Kikuchi, M., Y. Takahashi, T. Suga, S. Suzuki, and Y. Bando, "Mechano-Chemical Polishing of Silicon Carbide Single Crystal with Chromium(III) Oxide Abrasive," J. Amer. Ceram. Soc. , 75, No.1, (1992) 189-195

23. Raghunandan, M., N. Umehara, and R. Komanduri, "On the Possibility of Chemo-Mechanical Polishing of Silicon Nitride," Proceedings of Symposium on Tribology in Manufacturing, ASME/STLE Tribology Conference, Lahaina, Maui, Hawaii, (1994) 81-98

24. Marshall, D.B., A.G. Evans, B.T. Khuri Yakub, J.W. Tien, and G. S. Kino, "The Nature of Machining Damage in Brittle Materials," (1983), Proc. Roy. Soc. (Lond) A385, 461-475

25. Yasunaga, N., N. Tarumi, A. Obara, and O. Imanaka, "Mechanism and Application of the Mechanochemical Polishing Method using Soft Powder," 1979, NBS Publication No. 562, 171-183

3. RAMAN SPECTROSCOPY AND RADIO FREQUENCY ABSORPTION

J. Lange
Department of Physics
Oklahoma State University
Stillwater, OK

3.1 SUMMARY

A non-contract light scattering technique was developed to evaluate surface properties of silicon nitride bearing balls and relate this information to wear properties of the ceramic. The inelastic scattering from the vibrational states of the crystalline silicon nitride ceramic is known as Raman scattering. This technique yields a rapid, non-contact method of characterizing the physical properties of the near-surface (~ 2 μm) ceramic material in bearing balls. A number of features of the Raman spectra are demonstrated to be related to properties of the ceramic which are pertinent to the performance of the bearing balls. The physical properties determined by Raman scattering include internal strain, relative quantities of the low and the high temperature phase of silicon nitride, impurity compositions, and defects in crystalline structures of the ceramic. Internal strain of the ceramic determined by using the Raman light scattering technique correlates with rolling contact fatigue wear test results. The Raman technique also identifies local physical parameters, such as strain gradients which lead to chipping in wear tests, to be related to local damage.

The dielectric constant and losses of silicon nitride ceramics were measured over a wide frequency range (100 MHz - 10 GHz). Ceramic rods used in rolling contact fatigue (RCF) wear tests were cataloged using measurements of the dielectric constant and losses over a wide frequency range. The dielectric properties of the RCF rods did not correlate with wear testing done by Timken Research Center. The wear tests were using a high load and may not be representative of bearing response.

3.2 RAMAN SCATTERING AND SILICON NITRIDE CERAMICS

Raman scattering was demonstrated by to be an effective non-contact evaluation technique for ceramic bearing balls. A method was developed which allowed characterization of strain and composition of the near surface region (within 2 μm) of the bearing balls. Failure mechanisms in wear-tested silicon nitride surfaces were shown to correlate with the strain and the composition of the bearing ball surfaces. Measurements on a suite of commercial bearing balls provided extensive data to demonstrate the usefulness of the Raman scattering technique in evaluating the quality of ceramic surfaces. Various preparation stages from blanks to polished balls to wear tested regions were all evaluated from the inelastic light scattering techniques used to make Raman measurements. No float polished materials were available during the 2 year NDE phase of this program. The sources and surfaces states of the ceramics used in this investigation are shown in Table 4 in their "as received" condition. The surfaces were further treated by both mechanical abrasive polishing and chemical polishing using techniques recommended by Buehler LTD. In addition to the silicon nitride ceramics' high purity (99.9%), powder of crystalline silicon nitride was obtained from the Aldrich Chemical Company in both predominantly alpha and beta phase mixtures.

The high purity silicon nitride powder provided a Raman spectra that reflected the basic crystalline structure without complications due to components present in the ceramic form, such as fluxing agents or processing procedures. The Raman spectra for the pure powders provided a baseline to compare with the response of ceramics. The Raman spectra are shown in Figure 40 for two phases of crystalline silicon nitride referred to as the alpha or low temperature phase (upper trace) and the beta or high temperature phase (lower trace). The spectra for these two phases are distinct because the crystalline symmetry is different for the two phases. The vibrational modes which inelastically interact with the incident light to yield the Raman spectra are quite different for the two phases. This distinct Raman signature for the two phases was used to quantitatively identify the relative components of alpha and beta phase in the silicon nitride ceramic. The relative weight

Table 4 Commercial sources of the silicon nitride ceramics
(the "as received" condition and material type are also listed)

SOURCE	MATERIAL TYPE	CONDITION
Cercom	PSO-H	Blanks
	PSG-H	Blanks
ESK	2000	Bearing Balls
Norton Advanced Ceramics	NBD 200	Bearing Balls
	NBD 100	Bearing Balls
Timken Research	Various	RCF Rods
Toshiba	TSN-03NH	Bearing Balls
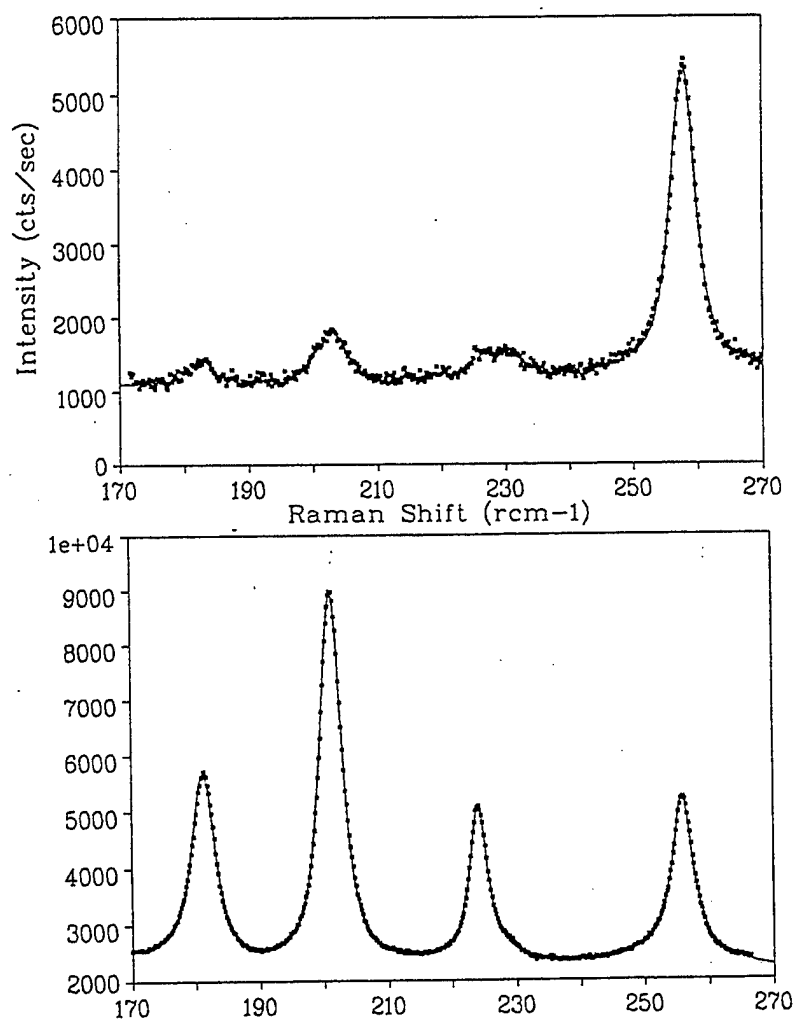
Figure 40   The Raman spectra for a high purity (99.9%) silicon nitride powder. The upper spectra predominately the low temperature or alpha phase of silicon nitride while the lower spectra are predominately the high temperature or beta phase.

percent was obtained by evaluating the relative Raman peak areas of the alpha phase at 258 cm^{-1} and the beta phase triplet peaks at 182 cm^{-1}, 202 cm^{-1}, and 226 cm^{-1}. The graph in Figure 41 yields the weight percentage of a particular phase from the relative peak area. This procedure was used in the following to characterize the relative phases of crystalline silicon nitride in ceramic bearing balls.

The Raman spectra of silicon nitride ceramics are more complex than the pure powders since additional components exist due to the flux and processing. The oxygen present in most fluxes, (i.e. magnesium oxide and alumina), can lead to the formation of silicon oxynitride in the ceramic. This compound has a different vibrational spectrum than silicon nitride and can be identified in the Raman spectra by additional peaks. These peaks are shown in Figure 42 where the experimental Raman spectra (points) are fit numerically to a series of peaks, the origin of which is alpha and beta phase silicon nitride in addition to silicon oxynitride. This figure illustrates how Raman spectra can be used to evaluate the phases of silicon nitride and relative amounts of additional compounds such as silicon oxynitride. The areas for the fit peaks were used to evaluate the relative abundance of the alpha and beta phase as well as that of silicon oxynitride. The evaluation process used software which required less than a minute to run.

The Raman scattering spectra provided considerable information concerning the phases, composition, and distortions in the near surface region of the ceramics. The region sampled by Raman scattering was within 2 μm of the surface. This is the region which is most critical in defining the failure modes of silicon nitride ceramic bearing balls.

3.3 RAMAN SCATTERING AND WEAR PROPERTIES

The Raman scattering technique was correlated with tribological testing using both bearing balls and rolling contact fatigue (RCF) rods. The correlation was done with silicon nitride ceramics supplied by Timken Research Center and Enceratec. No float polished materials were available during the NDE phase of the project.
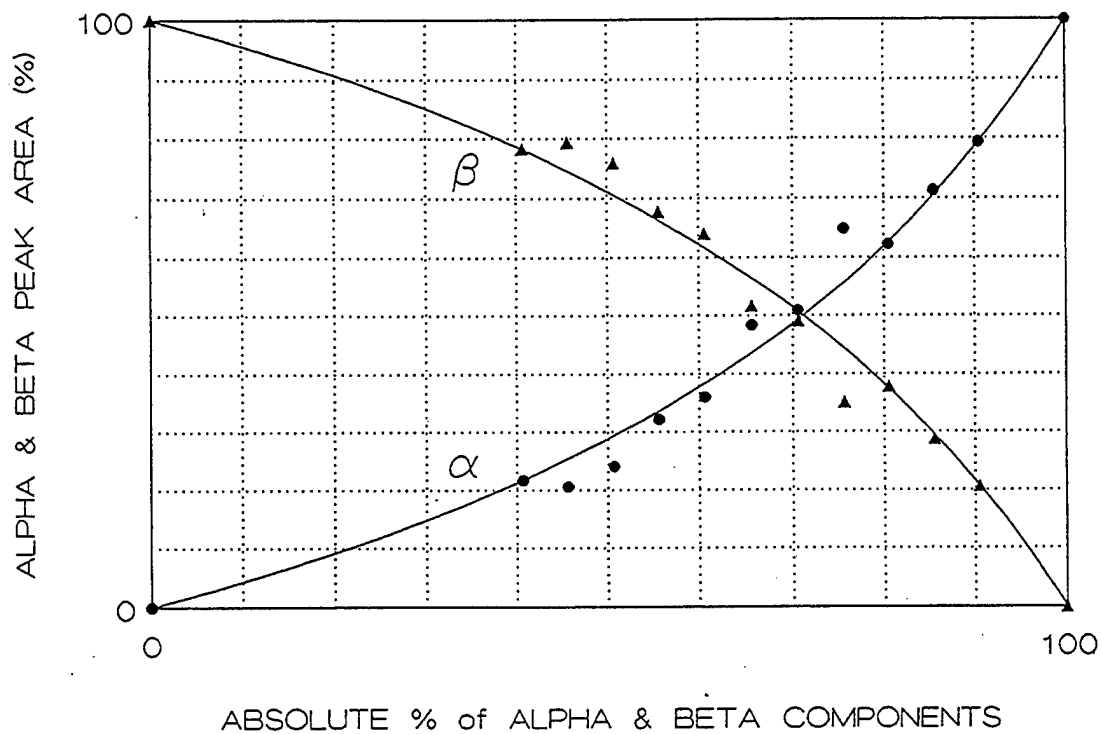
Figure 41   The relative peak area for the two phases of silicon nitride as a function of their weight percentage. This graph is used to evaluate the alpha and beta phase weight percentages in the ceramic bearing balls.
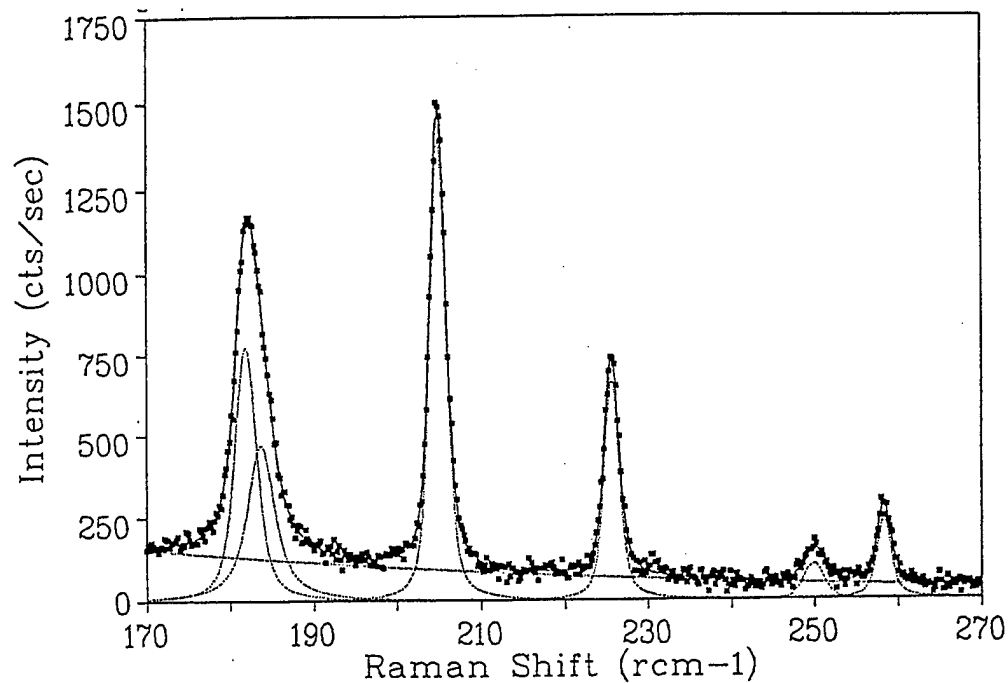
Figure 42   The Raman spectra of a typical silicon nitride ceramic bearing
ball of predominately beta phase material. Peaks due to the
alpha phase and silicon oxynitride are present as well as the
beta phase.

Detailed analysis of the Raman spectra (Figure 42) yielded parameters which were correlated with the results of mechanical fatigue tests performed by Timken Research. A variety of sources were used to supply rolling contact fatigue rods of a silicon nitride ceramic for three-ball wear testing. The wear tests were done with high loads which may not be characteristic of bearing ball operating environments. The RCF rods were examined in detail using Raman scattering. Both virgin material and wear tracts were investigated using a micro-Raman technique which interrogated a small volume about 10 µm in diameter and 2 µm thick. A large number of scans were done at random positions on the virgin material to evaluate the homogeneity of the RCF rods. Little variation in the spectra was noted within any given material. There was considerable difference between rods in both their compositions and properties and their wear resistance.

Particular features of the Raman spectra were correlated with the wear evaluation results. This included the peak position and peak width of the silicon nitride beta phase spectra. Since Raman scattering is a result of the incident laser light interacting with the vibration of the crystalline unit cell, the peak positions are sensitive to the symmetry of the crystalline unit cell. Distortions of crystal symmetry due to strains in the ceramic were detected as a shift in the beta phase peak positions. If the strain were an extension, the peak shifted to a lower energy, while a compression yielded a higher energy shift.

The strains occurred in the ceramics due to defects such as vacancies, grain boundaries, and fluxing materials. All of these features can potentially affect the wear properties of the ceramic. The peak positions of the Raman spectra were altered by internal strain through the distortion of the crystalline unit cell due to strain. This distortion was a local effect the magnitude of which can vary at different locations in the ceramic due to a heterogeneous distribution of defects and phases in the volume of interrogation. The heterogeneous defect distribution lead to Raman peaks different from the ceramic within the volume excited by an incident laser beam. The net result was a broadening of the overall Raman peak obtained from this volume. The increase in peak width is known as inhomogeneous broadening. Thus the

positions of the Raman peaks were affected by the average strain while their width were determined by the local heterogeneous strain distribution.

The width of the Raman beta phase spectra was verified as directly related to the damaged region by observing micro-Raman spectra from a pyramidal indentation on a bearing ball (Norton Advanced Ceramic NBD200). The peak width was determined for five sites approximately 10 μm in diameter from the center of the indentation to a region of virgin material. A cartoon of the indentation shows the position of the laser beam as letters the size of which is much larger than the interrogated spot. The beta spectra were evaluated and the peak width plotted as a function of position (Figure 43). The largest values of peak width were in the indented region where the maximum mechanical damage occurred while the minimum peak width occurred in the virgin material. This was an empirical connection between the peak width of the Raman spectra and the amount of damage in the ceramic.

The correlation of wear with the position and width of the Raman peaks was done for eleven RCF rods evaluated by Timken Research Center, using a three-ball technique. The rods came from a variety of sources and were rated poor, good, or excellent in wear performance. The correlation of the Raman peak parameters (position and width) are shown in Figure 44 for the RCF rods. Superimposed on the graph are the evaluations determined from the RCF tests.

The rods with the largest internal extension strain and peak width exhibited the poorest wear properties. The lower strain and width values were associated with the "excellent" wear characteristics. Comparison of the spectra for the ceramic with that of the pure powder indicated the strain was extended and of a very small magnitude in the ceramics with the best wear characterization. The empirical relation between the width and indentation damage shown in Figure 43 suggested that the width of the Raman peak was associated with statistical damage in the ceramics. The larger peak shift was associated with more coherent damage mechanisms such as vacancies and grain boundaries. The empirical results of the wear tested materials suggested
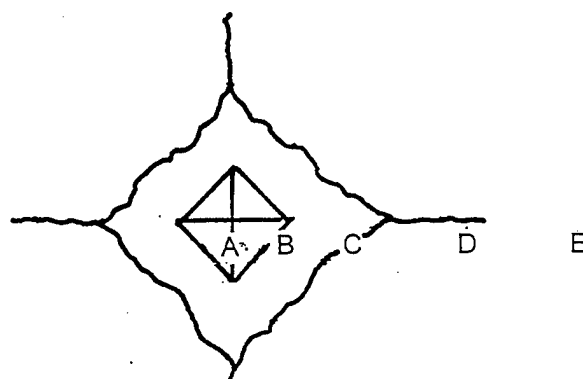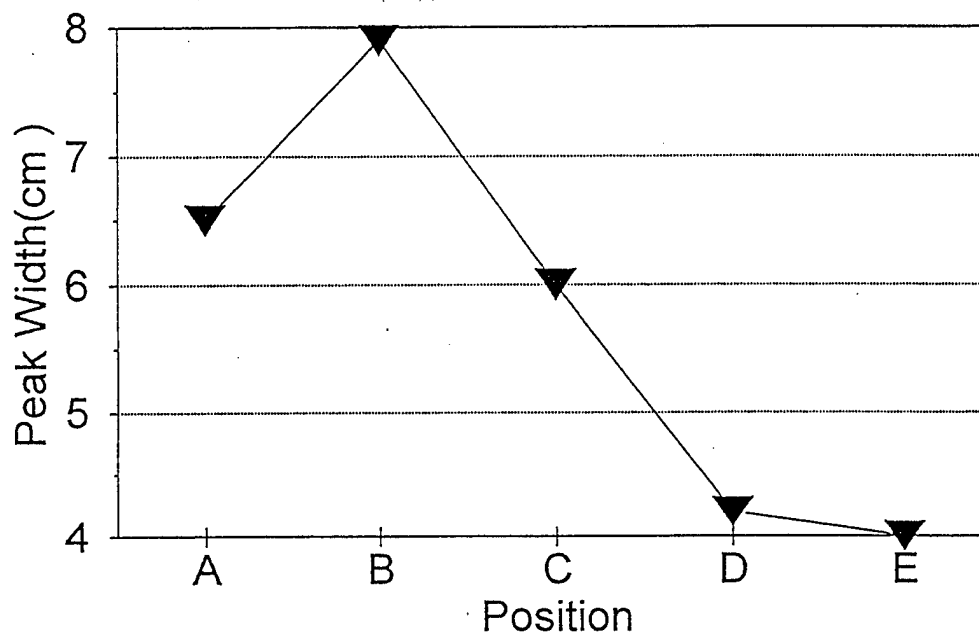
Figure 43   The width of the second beta phase peak as a function of position spanning a pyramidal indentation in a Norton Advanced Ceramics NBD bearing ball. A micro–Raman technique was used to evaluate a region less than 10 μm in diameter.
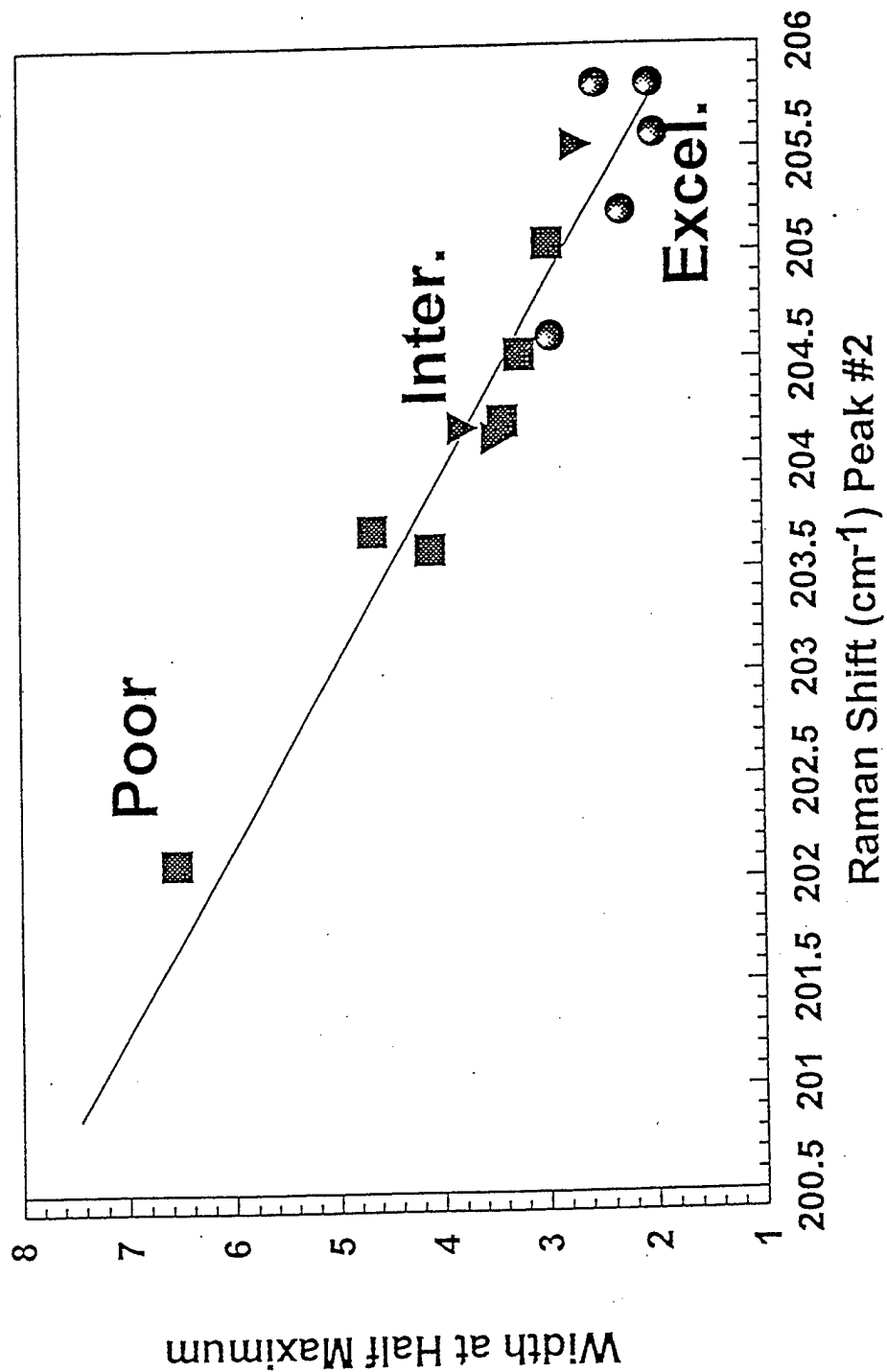
Figure 44   The width as a function of position for a Raman peak due to beta phase silicon nitride ceramic. The points correspond to different ceramic rods used in rolling contact friction wear testing. The wear quality is indicated by a poor (squares), intermediate (triangles), and excellent (dots) designation.

poorer wear was correlated with defect structures detected by the character of Raman spectra.

A specific relationship between strain in the ceramic and its wear properties was obtained by using the micro-Raman probe to evaluate regions in a known natural defect region such as a chipped area in a wear track of a RCF rod. Again the probed region was much smaller than the letters used to designate the central positions in the figure at which the Raman spectra were detected. A scanning electron microscope picture of the chip region along with a cartoon of its elevation are shown with the probe position in Figure 45. The micro-Raman spectrum of the silicon nitride was determined at a number of locations spanning the chip. The shift of the peaks relative to virgin material outside the chip was determined as a function of position. The Raman shift was proportional to the extension strain in the crystalline material sample by the 10 μm probe beam diameter. A large change in the strain was observed to occur in the vicinity of a small (less than 10 μm) discoloration of the ceramic. The strain was anomalously large in this region and was associated with this inclusion. A distinct Raman spectra of the inclusion was not observed so it could not be identified. The similarity in the strain profile and inclusion position suggested the chip resulted from the heterogeneous strain introduced by a foreign body.

The observation of a large heterogeneous strain in the vicinity of a defect demonstrated the value of the Raman scattering technique in evaluating potential regions of failure in ceramics. Structural and compositional features of the ceramic which could not be observed using the visible and electron microscope were detected by Raman scattering and are displayed in Figure 45. Visual and interference microscopy cannot detect and therefore do not offer any warning of potential failure due to heterogeneous strain distributions. Other Raman spectra characteristics such as peak width, offer a means of evaluating defect distribution such as vacancies (Figure 42) that are also not detected by visible and electron microscopy. The Raman technique offers the possibility of imaging structural and compositional distributions in ceramic machine components to display potential failure regions which are not detected using visible or electron microscopy.
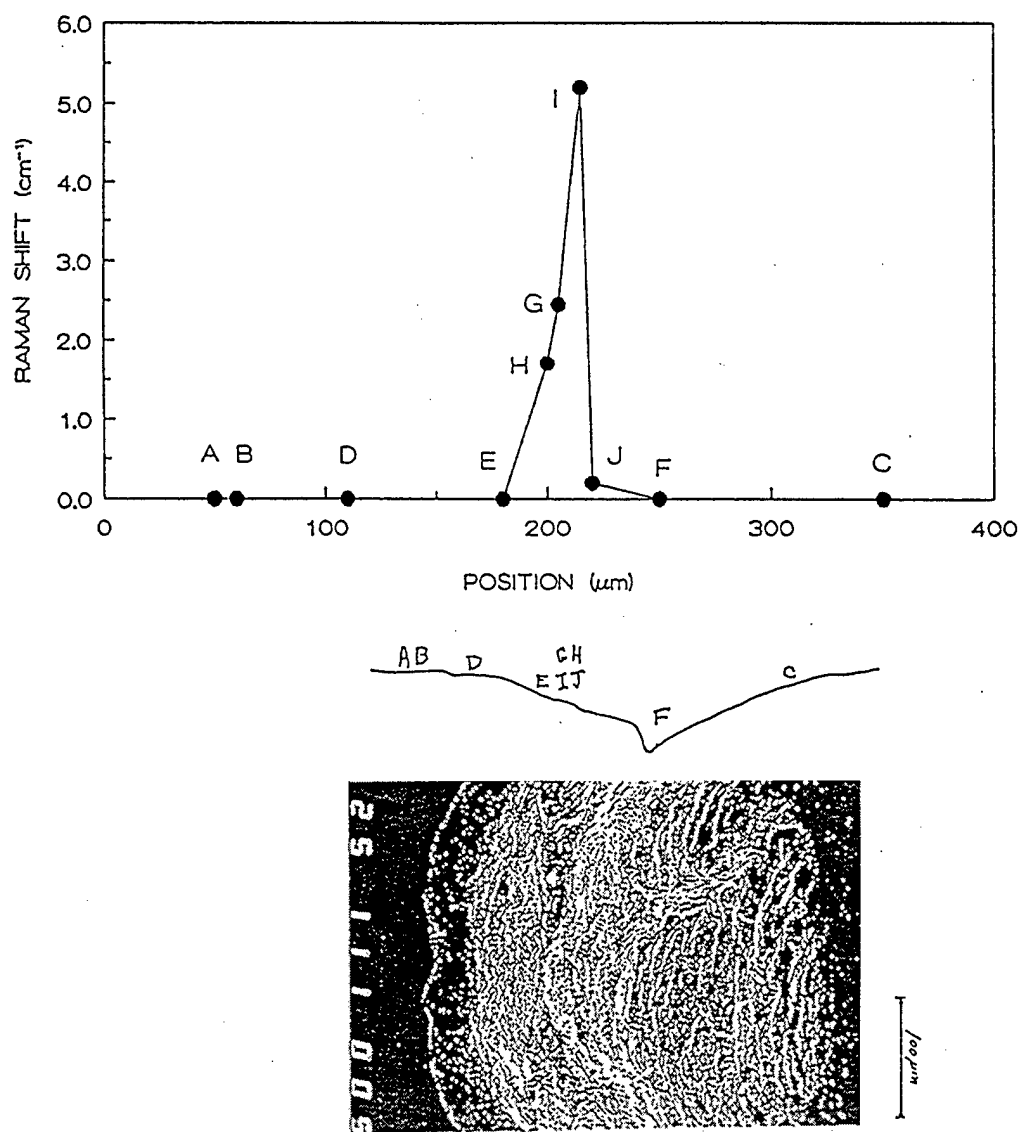
Figure 45   The shift of the second beta phase Raman peak as a function
of position across a chipped region in a RCF rod. A micro-
Raman technique is used to interrogate spots less than 10 μm
in diameter. A depth contour and SEM photograph are
shown below.

Evaluations of a number of commercially produced ceramics were made using the Raman technique. The amount of high and low temperature phase was determined along with the relative amount of silicon oxynitride and strain magnitude. Four manufacturers and seven material varieties were evaluated with the results shown in Table 5. Large variations in the observed parameters indicated the differing approaches taken by these manufacturers to maximize wear resistance. The flux and processing had a significant affect on the phase mixture, composition, and strain in the ceramic, determined quantitatively by analysis of the Raman spectra.

Variations in processing were also observed using the Raman technique, where spectra properties were observed for different lots from the same commercial source. Significant variations in the strain and defect concentration were observed between lots as illustrated in Table 6. Comparison of these properties between lots could be a means of using the Raman technique for quality control.

As illustrated above, the Raman scattering technique provided new and worn specimen pertinent information not available using traditional evaluation techniques. These results can be combined with software to provide rapid imaging to locate potential failure regions even in complicated ceramic machine parts. This information serves as a basis for further development of the application of the Raman technique to ceramic machine parts.

Manufacturer	Material	Alpha Phase (wt%)	Siliconoxynitride	Relative Strain
Cerbec	NBD 100	40	3.3	Extension
	NBD 200	6	3.8	Compression
	RCF ROD	5	3.2	+Compression
ESK	Ekersin 2000	15	4.0	Zero
Cercom	PSG	5	3.0	+Extension
	PSO	20	5.0	++Extension
Toshiba	TSN		5.0	++Extension

Table 5   The Raman scattering technique was used to evaluate structural and compositional variations in commercial beraing balls. The strain was determined relative to the Raman spectra for high purity powders.

112

Manufacturer	Lot #	Peak Position (cm⁻¹)	Peak Width (cm⁻¹)
Cerbec	1	205.6	4.1
	2	205.4	3.6
ESK	1	204.7	3.9
	2	204.6	3.7

Table 6   The average difference between two lots of ceramic bearing balls from two different manufactures. The most probable error evaluated from this suite of measurements using normal distribution statistics is +-0.12 reciprocal centimeters.

4. RAYLEIGH-BRILLOUIN BACKSCATTERING FROM SI3N4 CERAMICS

J. P. Wicksted
Department of Physics
Oklahoma State University
Stillwater, OK

4.1   SUMMARY

We have investigated the effects of wear properties of several Si_3N_4 ceramic materials on Rayleigh-Brillouin backscattered light. The materials were previously wear tested (rolling contact fatigue test) and were classified as excellent, mediocre, and poor. The backscattered signal was measured using a multi-pass tandem Fabry-Perot interferometer. By using calibrated optical density filters and assuring the same solid angle of collection, we were able to clearly differentiate between their respective signals. Experiments performed on two balls that were taken from a lot of identically prepared balls gave similar signals. Our measurements suggest that this is a viable technique to differentiate between ceramics with various wear properties and to check consistency within the same group.

Surfaces which were subjected to different polishing grit sizes were studied, in addition to analyzing both flat and curved surfaces. Two different Fabry-Perot interferometric systems were used to study the Rayleigh-Brillouin scattering from these surfaces. We note that Brillouin modes could not be obtained from any ceramic surface due to the intense, diffuse Rayleigh scattering.

4.2   INTRODUCTION

We have investigated the feasibility of using Rayleigh-Brillouin backscattering to differentiate between Si_3N_4 ceramics that have different wear properties. The tasks of this research were to:

i. develop an optimal configuration of the already existing Brillouin scattering setup;

ii. construct or purchase a tandem Fabry-Perot interferometer and integrate it within our optical setup, resulting in a higher experimental resolution and contrast;

iii. compare the Brillouin peak positions and Rayleigh scattering components between high quality samples (excellent wear tests) containing few imperfections with samples whose surfaces possess many defects (mediocre to poor wear tests), examining several surface regions of all samples studied;

iv. investigate shifts in Brillouin frequencies and changes in Rayleigh components when surfaces of ceramic samples have undergone different polishing techniques; and

v. compare the surface properties of ceramic samples using the Rayleigh-Brillouin backscattering technique with other NDI methods such as Raman scattering.

We have fulfilled each of these tasks during the three year period of this contract. We wish to point out, however, that it was not possible for us to observe a Brillouin pattern consisting of either bulk or surface acoustic modes. The strong elastic (Rayleigh) scattering component precluded our being able to determine these mode positions and intensities. However, the Rayleigh components were very clearly observed and allowed us to undertake each of the goals set forth at the beginning of the project.

4.3 RESULTS

4.3.1 Task 1

At the beginning of the contract, we used our current experimental equipment to construct a Rayleigh-Brillouin backscattering configuration

(System No. 1). This utilized an argon-ion laser and a Burleigh five-pass Fabry-Perot interferometer with a DAS-10 stabilization unit (see Figure 46). An air-spaced etalon was inserted into the laser cavity to get out a single mode which increased the coherence length of the beam and resulted in a clean TEM_{00} mode. The beam was horizontally polarized after passing through a polarizer. All mirrors were broad-band coated from 450-650 nm. An Olympus compound camera lens of effective focal length 50 mm served as the focusing and collecting optics. An achromatic lens of focal length 500 mm focused the collected light through the pinhole of the Fabry-Perot interferometer. A photomultiplier tube (PMT) ITT FW130 was used for detecting the signal. It was cooled to -25 °C, giving a dark count of 1.5 cts/sec and 10% quantum efficiency at 514.5 nm. The voltage supplied to the cathode was -1900 V. It has a circular detection area of diameter 2.5 mm. The data were collected in a multichannel analyzer (Canberra series 35 plus) and then downloaded to a personal computer.

The first measurements were conducted on a silicon [100] crystal. This was our standard when performing backscattering measurements from opaque samples. The laser light was p-polarized (parallel to the scattering plane) with an angle incident at the critical angle for the sample under study. This was the procedure used throughout all our measurements.

In order to conduct the Rayleigh-Brillouin studies on silicon, long scan times were required. Two examples are illustrated. In Figure 47, an unpolished sample of silicon is shown. This spectrum was obtained using 10,000 scans of the Fabry-Perot, each scan lasting one second (overall time 2.8 hours). The laser power was 10 mW and the free spectral range (FSR) of the Fabry-Perot was 4 cm^{-1}. In Figure 48, a polished silicon sample was measured using 100 scans at 100 seconds per scan (overall time 50 minutes, DAS-10 was off). A laser power of 300 mW was used and the FSR was varied. Note that only the Stokes and anti-Stokes longitudinal acoustic mode was observed (small peaks observed in each spectrum). The spectrum from the polished sample required less time than the unpolished one because polishing reduces the amount of diffuse, elastic scattering.   The spectrum also seemed to look the best when the FSR was 6.5 cm^{-1}. The large structure seen on the left and

116
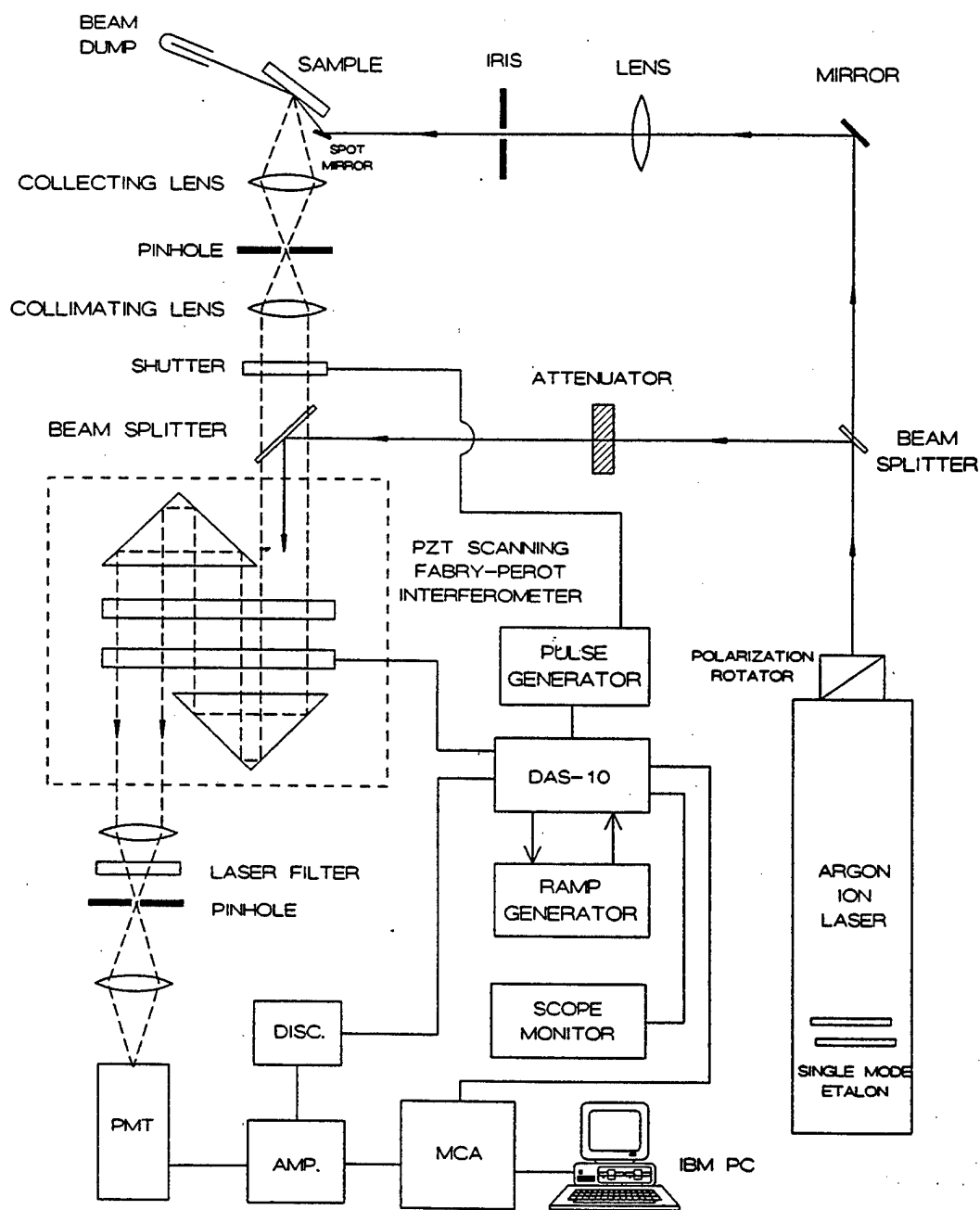
Figure 46   Experimental setup for System No. 1
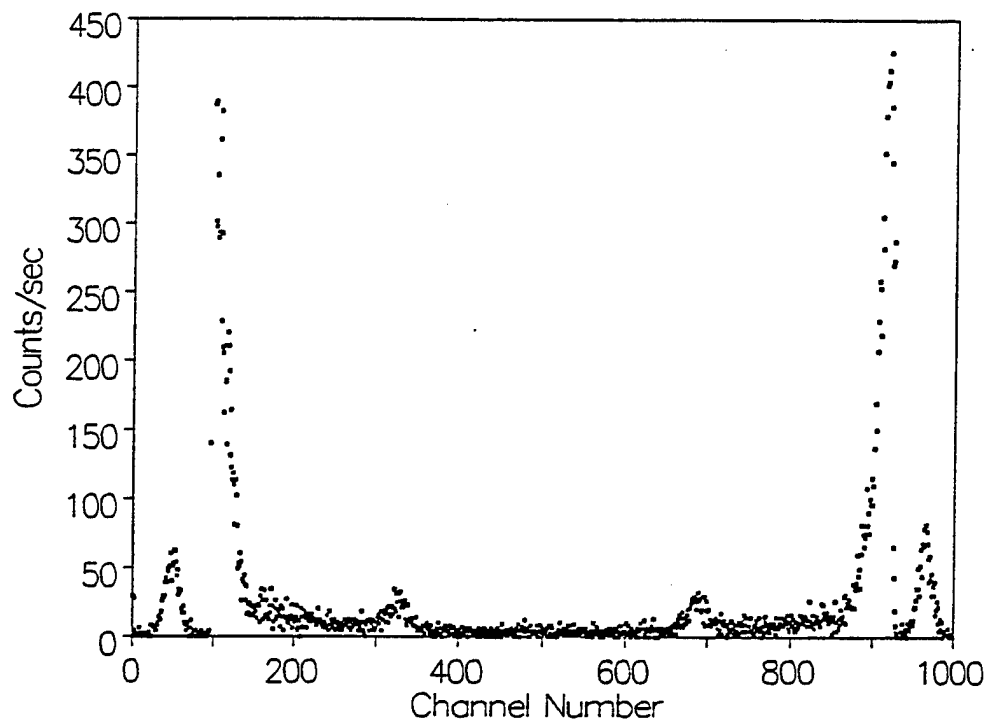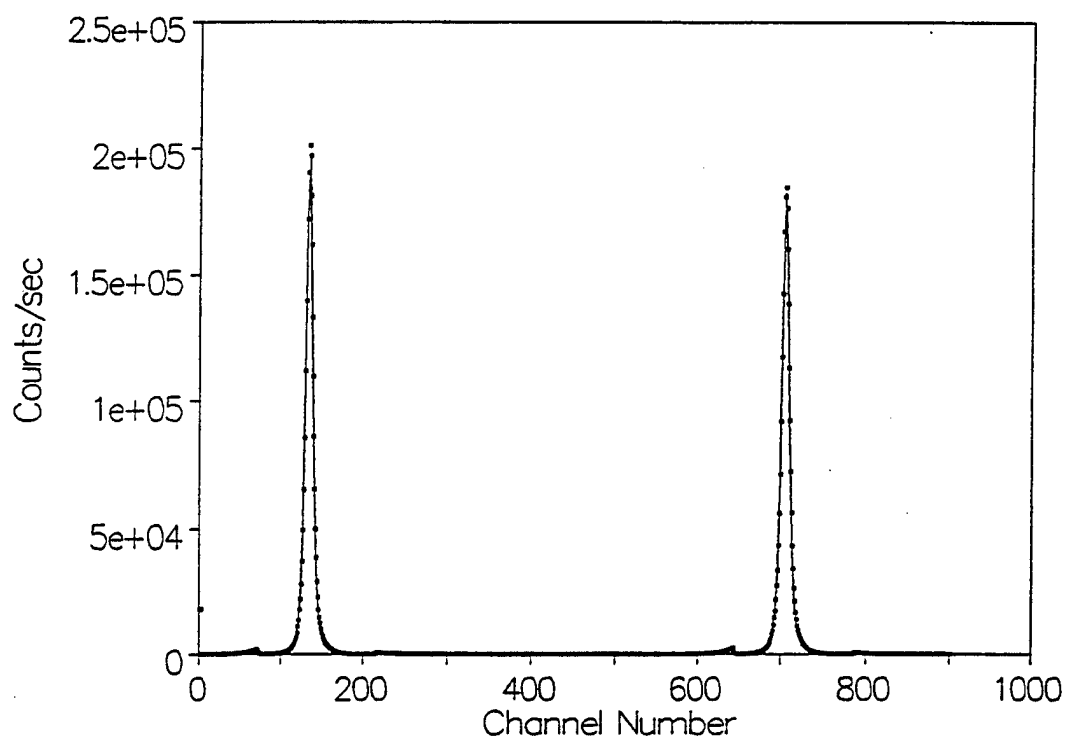
Figure 47   Data from silicon using System No. 1
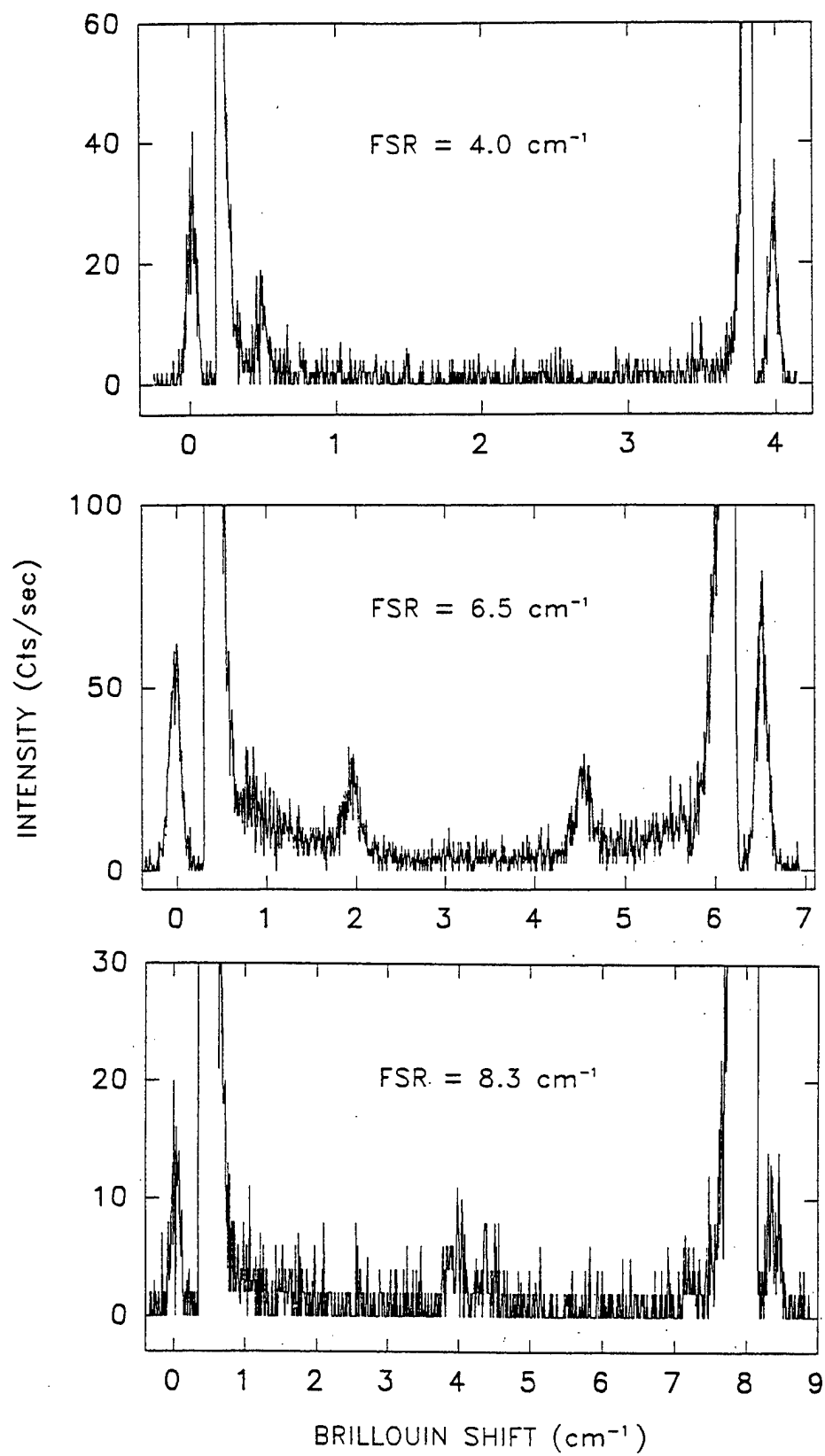
Figure 48   Rayleigh-Brillouin data from silicon using System No. 1 for different FSR

right sides of each spectrum is the Rayleigh scattering from the sample surface.

Our attempts to observe a Rayleigh-Brillouin spectrum from flat, polished surfaces of silicon nitride (Si_3N_4) utilized the FSR of 6.5 cm^{-1} and 100 second scans. Although no Brillouin components were observed from any silicon nitride samples, the strong Rayleigh line allowed us to formulate a correlation between Rayleigh intensity and surface wear (Task 3).

4.3.2 Task 2

The new instrument that was integrated into our setup to spectrally analyze the signal was a multi-pass tandem Fabry-Perot interferometer developed by Dr. J.R. Sandercock (System No. 2, see Figure 49). Traditional Fabry-Perot interferometers suffer from nonlinear scans, mirror tilting during the scan, and stability problems. Changing the mirror spacing is also tedious and it is not suitable for tandem operation. This design uses a deformable parallelogram which is acted upon by a single piezoelectric transducer and mirror spacings are monitored with a capacitor. The previously mentioned difficulties are not present in this design. All instruments necessary for monitoring and stabilizing the Fabry-Perot come with the system. We found this system to be much better in performance and easier to handle than the traditional Fabry-Perot.

The Rayleigh-Brillouin scattered light from the samples were collected in a backscattering geometry as shown in Figure 49. The other equipment is the same as for System No. 1. The PMT voltage used was -2200 V. The overall performance of the system was checked by looking at the Brillouin scattered light from Plexiglas®. In a backscattering geometry, the Brillouin shifts of the LA phonons (TA phonons are not allowed in backscattering) should be at 0.547 cm^{-1}, and should give 5-10 cts/ms/mW (5 is more common). We always got 3-4 cts/ms/mW due to the low quantum efficiency of the PMT. The output of the PMT was connected to a fast discriminator that produced 50 ns TTL pulses. The output from the discriminator was then split for monitoring and stabilization purposes, as well as data acquisition. The data were collected in a multichannel analyzer (Canberra series 35 plus) and

Conventional Backscattering Setup
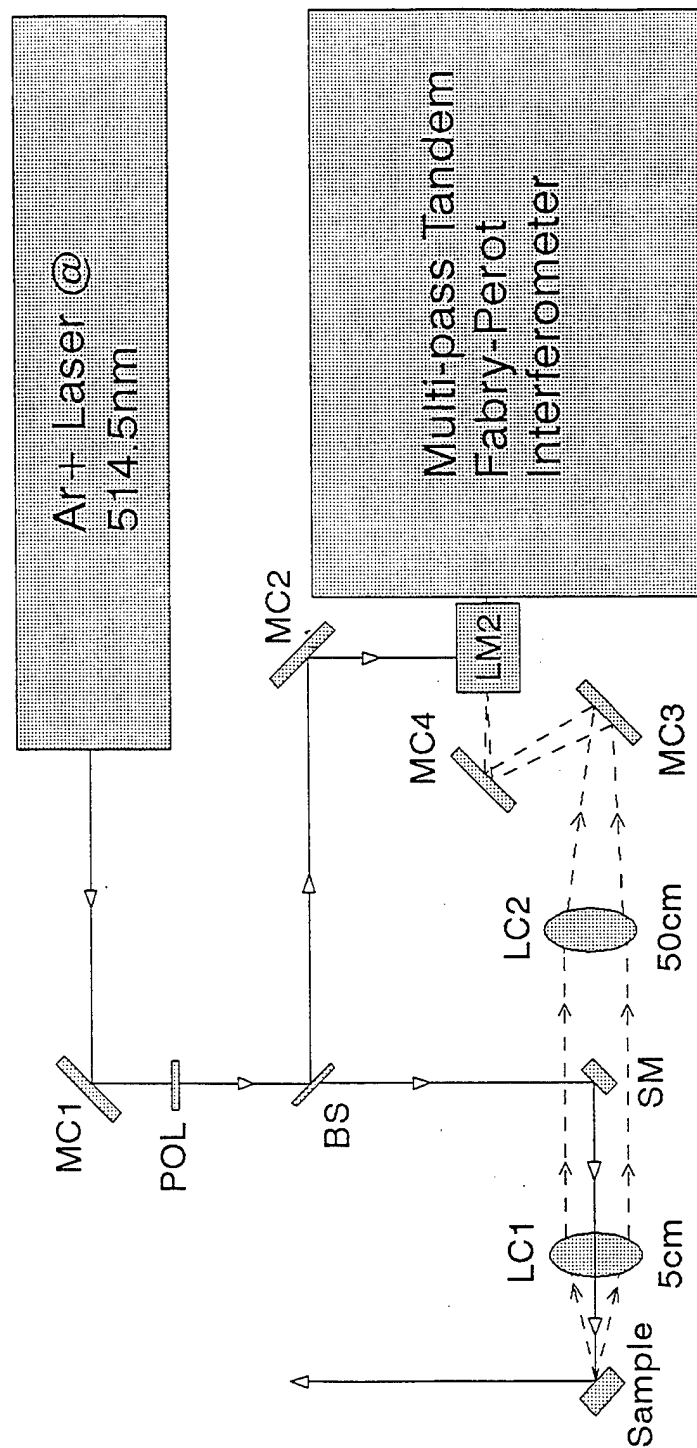
Figure 49   Rayleigh-Brillouin setup for System No. 2

then downloaded to a personal computer. In order to get good quality data, we always checked the alignment of our overall system. The input and output pinholes were set at 450 mm and 700 mm, respectively.

An example of the Rayleigh-Brillouin spectrum from a silicon sample using System No. 2 is illustrated in Figure 50. This scan used a FSR of 8 cm^{-1} with a scan time of 0.512 seconds for 500 scans (43 minutes). In addition to a strong Rayleigh component at 0, Stokes (negative values) and anti-Stokes surface acoustic modes (sharp peaks at 0.5 cm^{-1}), small transverse bulk modes at 3.3 cm^{-1}, and strong longitudinal bulk modes at 4.6 cm^{-1} are clearly observed. The results shown in Figure 50 should be compared to Figures 47 and 48 which were obtained using System No. 1. As with System No. 1 no Brillouin components were observed from the Si_3N_4 samples, although the strong Rayleigh line allowed us to formulate a correlation between Rayleigh intensity and surface wear using System No. 2 (Task 4).

4.3.3 Task 3

We utilized System No. 1 to determine wear properties of silicon nitride surfaces using the strong Rayleigh signal observed. The three samples that were available to us were already wear tested using rolling contact fatigue tests. They were cylindrical rods and were classified as excellent, mediocre, and poor. To the eye, the excellent sample appeared gray, mediocre black, and poor light gray. In all cases, there was a clear difference in the Rayleigh scattered signal (Gaussian distribution). The peak height was determined to be the important differentiating parameter.

Table 7 shows the results using System No. 1. Eleven spots on each of the flat surfaces of the three cylindrical samples were studied. Fused quartz was used as a reference. An ND filter of 4.45 was used to attenuate the signal coming from all ceramic samples. Each scan was 0.5 seconds in duration and 1000 scans were taken from each spot on the surface. Most samples with peak intensities below 70,000 counts are either excellent or mediocre in surface quality. In addition, samples with full-width at half-maxima (FWHM) greater than 6.5 were generally of poor quality, however, the FWHM was not as reliable as the peak intensity for correlating surface wear.

Silicon (100)

Si–12S.DAT

d=0.625mm
FSR=8cm^{-1}
dwell time=0.5ms
scan time=0.512s
5000 scans
θ=75°
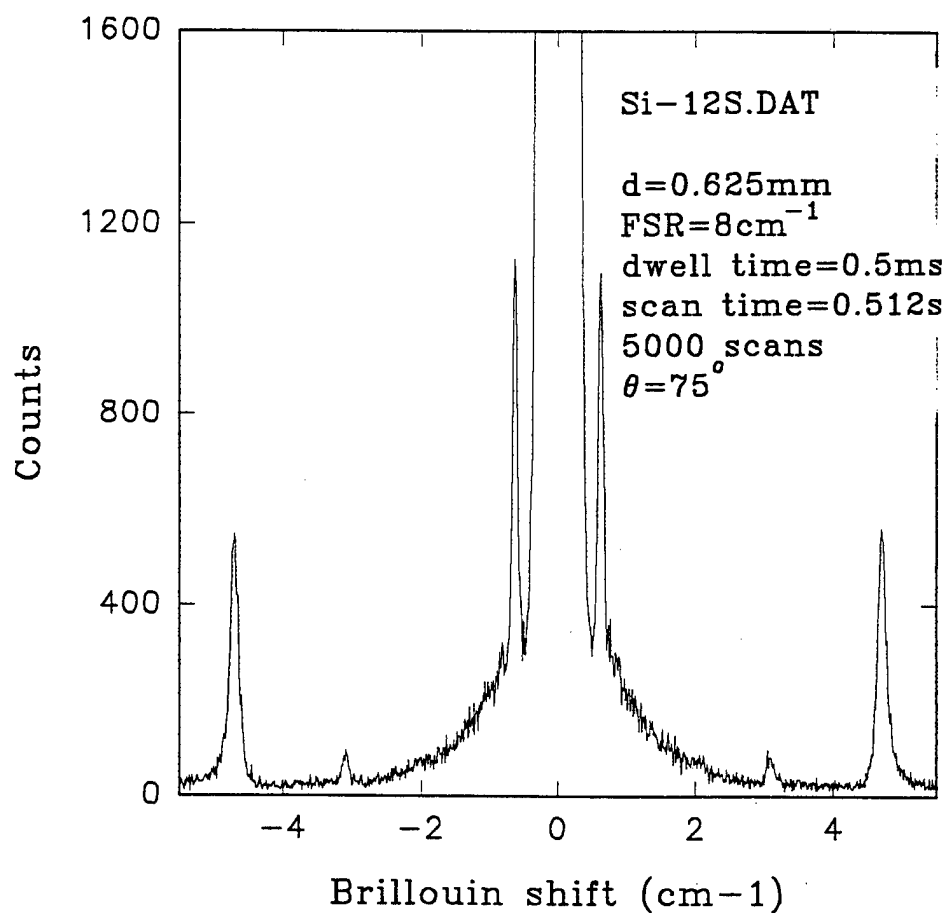
Figure 50   Rayleigh-Brillouin spectrum for silicon using System No. 2

Table 7. Peak intensities and FWHM results from excellent, mediocre, and poor cylindrical rods (flat surfaces) using System No. 1

Peak	Excellent	Quartz	Mediocre	Quartz	Poor	Quartz
Mean	71030	73576	67584	76297	74836	74665
St. Dev.	6970	4760	7945	2956	3119	2219
St. Err.	1643	1943	1873	1206	735	906
Max/Min	1.46	1.15	1.47	1.09	1.18	1.09

FWHM	Excellent	Quartz	Mediocre	Quartz	Poor	Quartz
Mean	5.76	6.08	5.79	6.55	6.75	7.01
St. Dev.	0.74	0.58	0.41	0.38	0.52	0.53
St. Err.	0.17	0.24	0.10	0.16	0.12	0.22
Max/Min	1.62	1.27	1.29	1.20	1.42	1.25

4.3.4 Task 4

This task utilized System No. 2; the tandem Fabry-Perot system was operated using a FSR of 2 cm^{-1}. The contrast was about 10^8 and the overall finesse approximately 120. The scan time was set for 500 ms per scan and 200 scans were taken for each data file giving a total data accumulation time of 100 s. The laser power at the sample was about 38 mW.

The same wear tested ceramic samples that were available in Task 3 were also used in Task 4. Each sample was mechanically polished on its flat surface from which Rayleigh-Brillouin backscattering measurements were taken. Data were obtained from 6 μm, 1 μm, and masterpolished surfaces. First, the samples were roughly polished using a 15 μm diamond grit wheel to smooth out any wedges that may have occurred in cutting the samples. They were then polished using a 6 μm Metadi® diamond paste lubricated with Metadi® fluid on a Texmet® polishing pad, all from Bhueler Ltd., for about 16 hours each. They were repolished for 8 hours using a smaller 1 μm Metadi® diamond paste with the same type of lubricating fluid and pad as before. Finally, we polished the samples one hour each using a Masterpolish®2 on a

Chemomet® pad from the same company. The master polish is a liquid media that polishes better than 0.25 μm and is in addition a chemical etch.

The samples were placed on a holder that was itself mounted on translation and rotary stages that allowed micro-positioning in three dimensions as well as micro-rotation about the vertical. It should be noted that the samples were not removed from their polishing stubs until they were master polished. This was done so that the surface being polished was parallel to the base of the stub which would not be the case if we were to glue and unglue the samples between each measuring and polishing process. Also, a wedge would inadvertently be introduced thus increasing the polishing time and making the surface have several polished planes. We also took measurements from two bearing balls which were taken from a lot of identically prepared samples. They each had a diameter of 9.695 mm and were polished to 10-50 nm but were not wear tested. The materials appeared black to the eye. Both flat and curved surfaces were investigated.

When the samples were placed at the focus of the collecting lens, the diffuse scattered light was very intense. Calibrated optical density (OD) filters were used to attenuate the collected beam going into the Fabry-Perot and where placed in between LC2 and MC3. The reflected light was carefully guided at 90° with respect to the incident beam. This was done by making the scattering volume align with the holes of the optical table by using alignment spikes. The alignment of the spikes and the overall beam position were monitored several feet away. To insure that we collect the same solid angle of light from the various points on the sample and with other samples, we placed a card just behind LC2 and micropositioned the sample such that LC2 was flooded while the reflected beam maintained 90° with the incident light. The scattering volume was about 38 mm away from the first lens (of the compound lens) which had a diameter of 35 mm. The OD filters were changed such that the signal remained above 1 V but below 5 V.

We looked at 11 different spots on each of the three cylindrical samples for each of the three polishing sizes. The data taken from the flat surfaces of the cylindrical samples with the same polishing are shown in Figures 51 (a) - 53 (b). They are plotted with peak height measured in counts and channel

Rayleigh scattering
Ceramic (6μm polish)

Figure 51 (a)   Rayleigh scattering from excellent, mediocre, and poor cylindrical rods (flat surfaces) using System No. 2

126

Ceramic (6 μm polish)

Figure 51 (b)   Rayleigh scattering results from excellent, mediocre, and poor cylindrical rods (flat surfaces) after 6 μm polish using System No. 2

Rayleigh scattering
Ceramic (1μm polish)
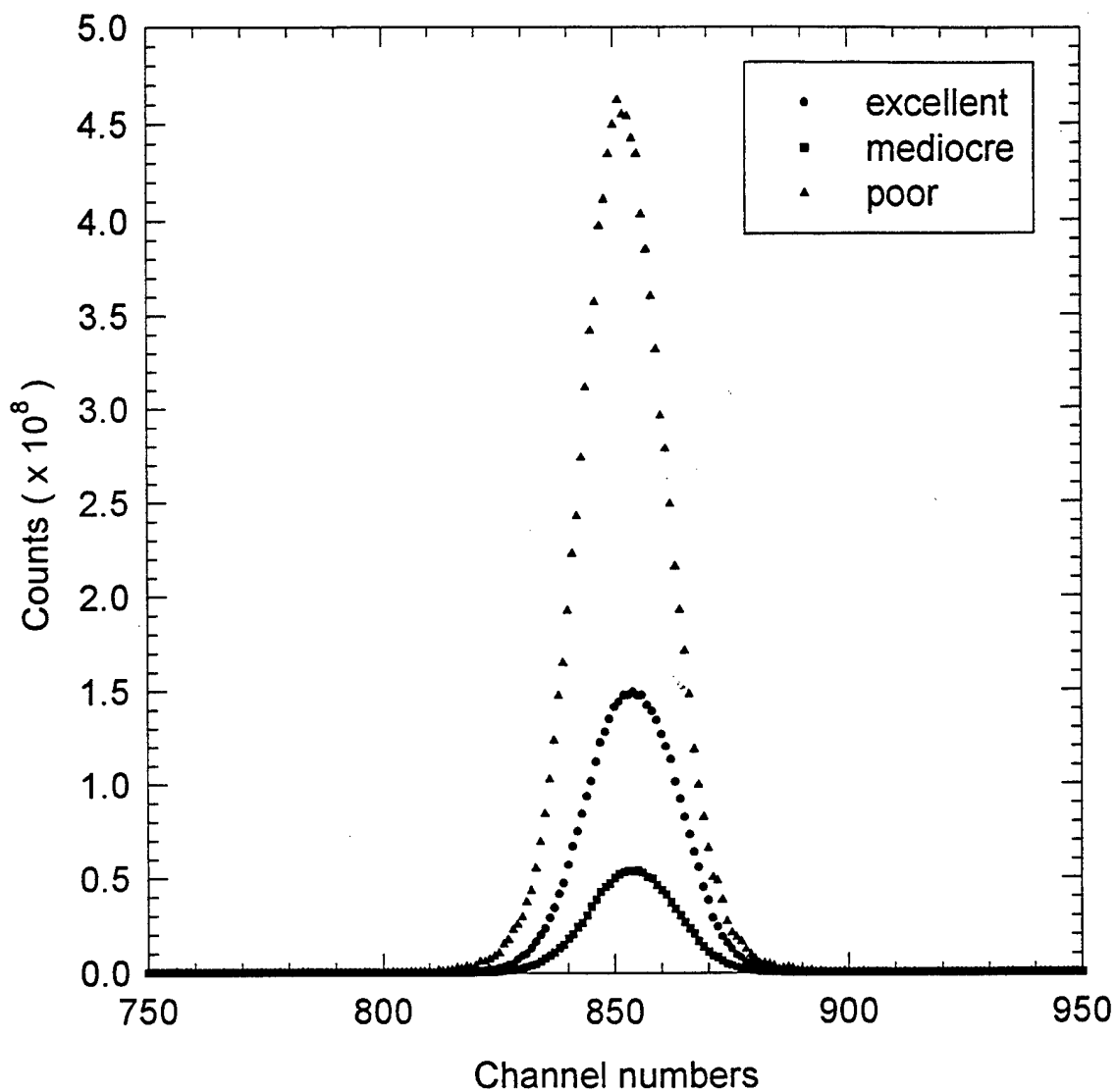
Figure 52 (a)   Rayleigh scattering from excellent, mediocre, and poor cylindrical rods (flat surfaces) after 1 μm polish using System No. 2

Ceramic (1 μm polish)
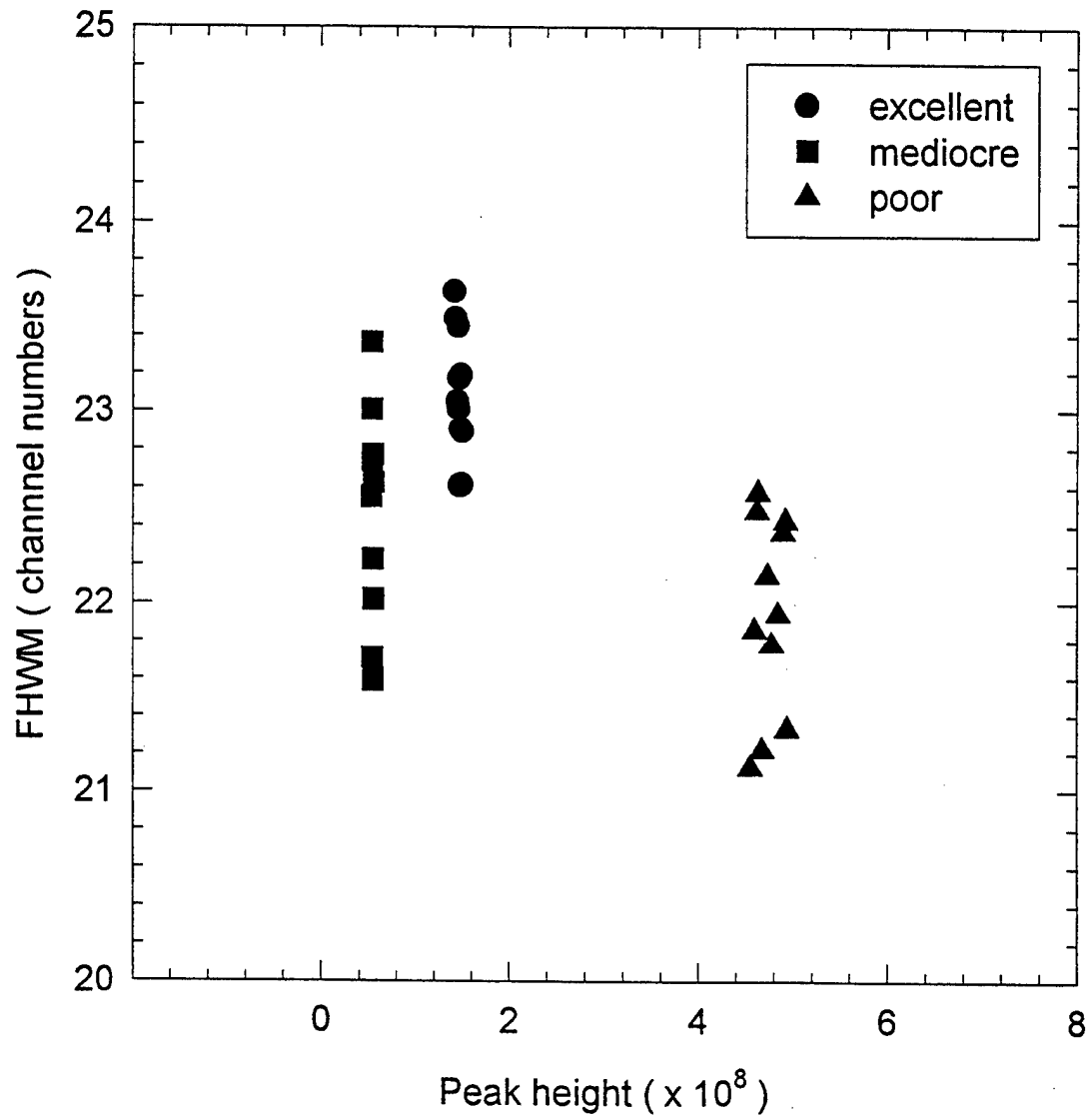
Figure 52 (b)   Rayleigh scattering results from excellent, mediocre, and poor cylindrical rods (flat surfaces) after 1 μm polish using System No. 2

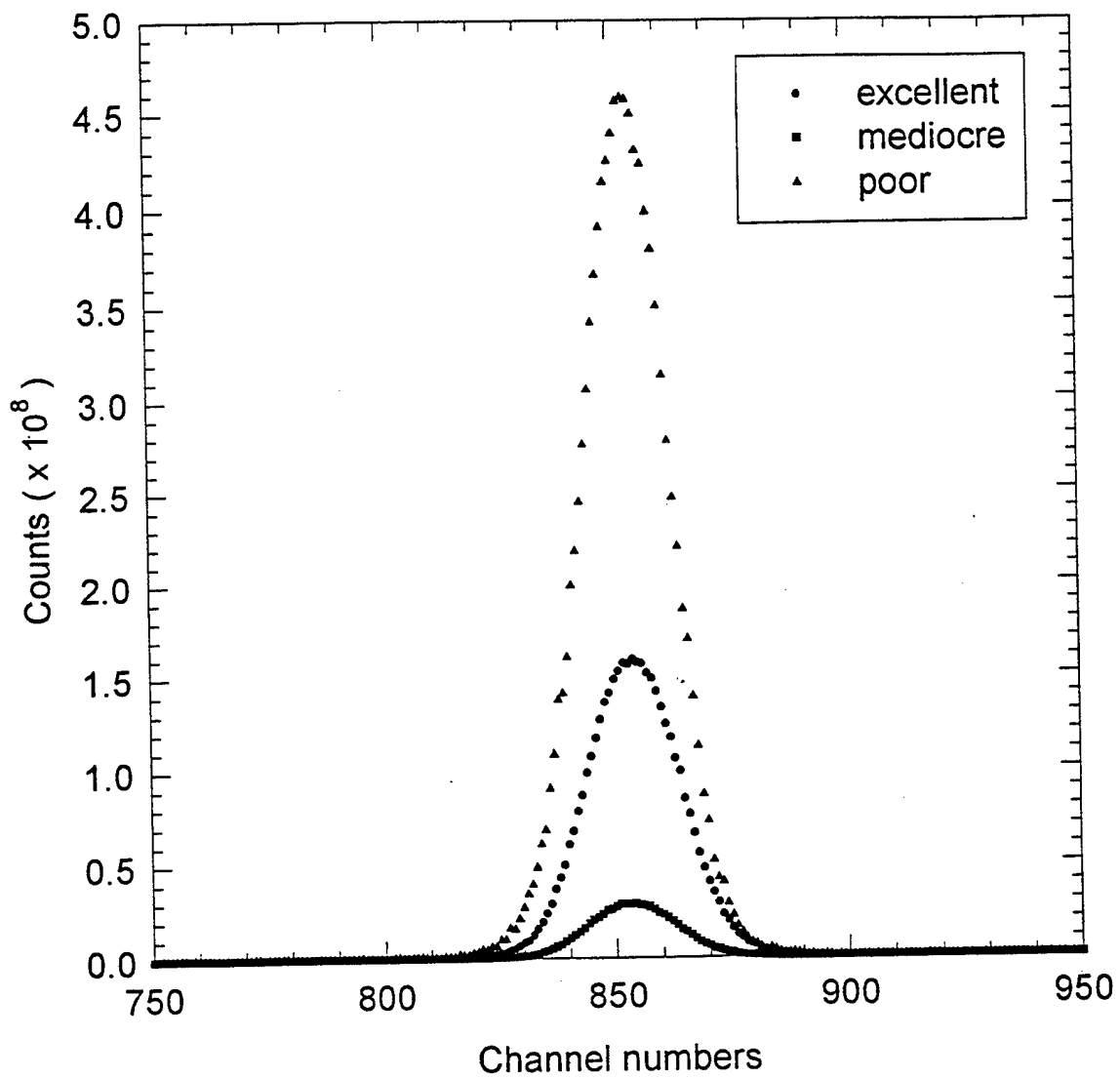# Rayleigh scattering
Ceramic (master polish)

Figure 53 (a)   Rayleigh scattering from excellent, mediocre, and poor cylindrical rods (flat surfaces) after masterpolish using System No. 2
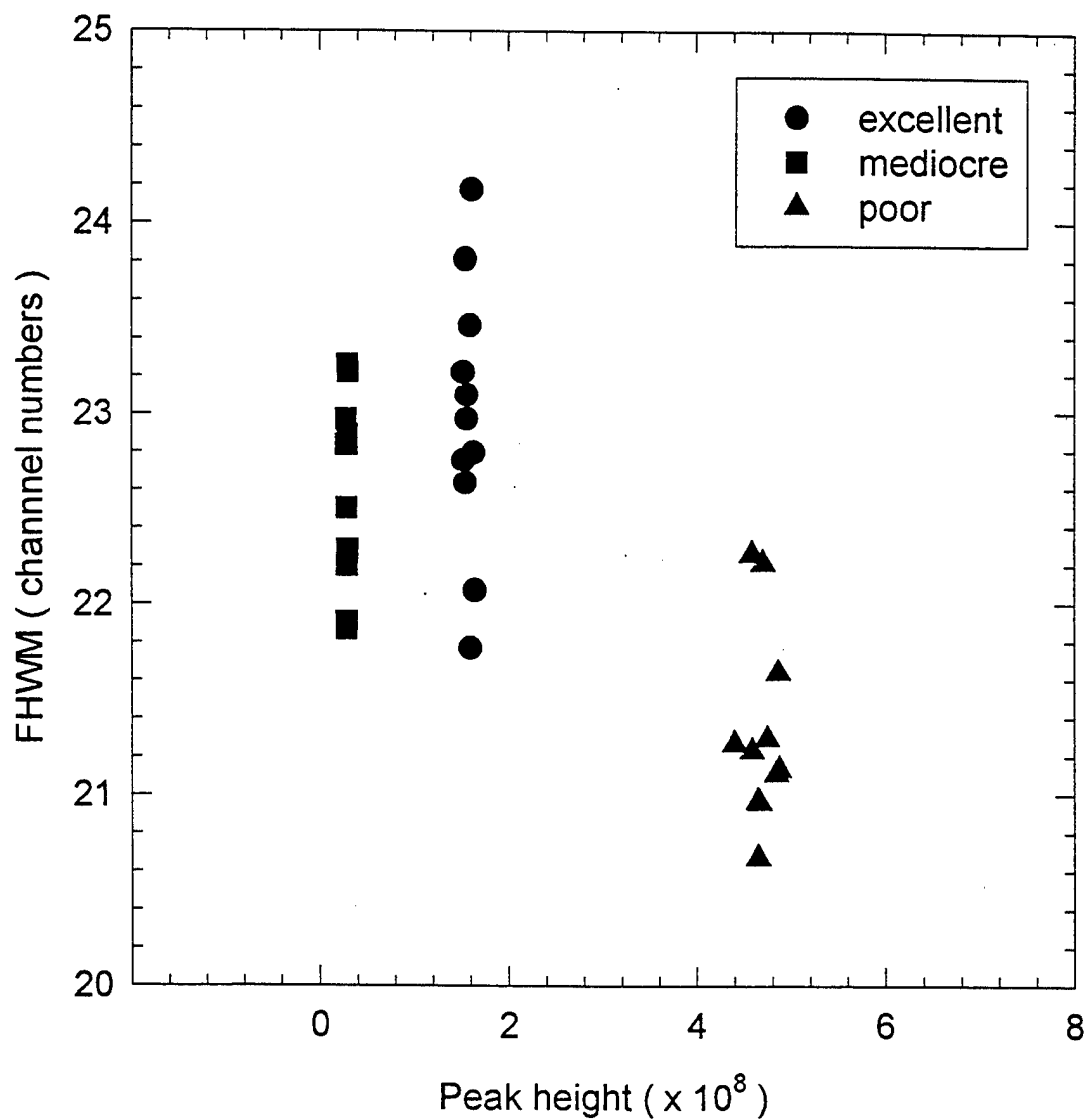
Ceramic (master polish)

Figure 53 (b)   Rayleigh scattering results from excellent, mediocre, and poor cylindrical rods (flat surfaces) after masterpolish using System No. 2

number taken directly from the Canberra. We detected a clear difference in signal from the various samples with the peak height being the differentiating parameter. The peak height definitely follows the trend poor > excellent > mediocre, with the poor giving a signal much greater than the others. The correlation to the full width at half maximum (FWHM) is not clear and is probably not a good differentiating parameter. To convert to wavenumbers, multiply the channel numbers by 0.0013 (2 cm^{-1}/1542 ch).

In Figures 54 - 56, we compare the signals from the same samples but different polishing sizes. For the excellent sample, the polishing did not change the signal appreciably. Although the 1 mm signal is slightly lower than the 6 mm signal and the masterpolish seems to be in the middle, we can not conclude that there is a definite correlation since we must also consider laser fluctuations. For the mediocre sample, there is an improvement in signal from 6 mm to 1 mm, but the masterpolish signal is almost identical to that of the 1 mm. Finally, the poor sample has indistinguishable signals for the 1 mm and the 6 mm but a huge increase for the masterpolish. It is unclear as to why there is big change. A compilation of Figures 54 - 56 are shown in Figure 57. Again, the differences in the three ceramics are marked. Interestingly, the FWHM of the poor sample does not have as large a spread as the others.

We also looked at 11 different spots on the curved surfaces of the cylinders and the results are shown in Figure 58 (a) and (b). It is difficult to interpret this set of data as the glue and chemical etch had definitely affected their surfaces. The poor sample had a particularly bad curved surface that was previously there before the polishing. The chemical etch and glue may have deteriorated it further. The signal from the excellent and mediocre are similar to their flat surfaces but that of the poor sample is considerably reduced. Nevertheless, the difference between the samples still remains. Finally, we looked at two bearing balls that were taken from a lot of identically prepared balls that were made of the same material. Their data are shown in Figure 59 (a) and (b). Again, we looked at 11 different spots and found that the signal remains very similar. This is encouraging since one can quickly check consistency within a certain lot of balls.

Ceramic (excellent)

Figure 54   Rayleigh scattering comparison from an excellent cylindrical rod (flat surface) after different polishes of 1 μm, 6 μm, and masterpolish
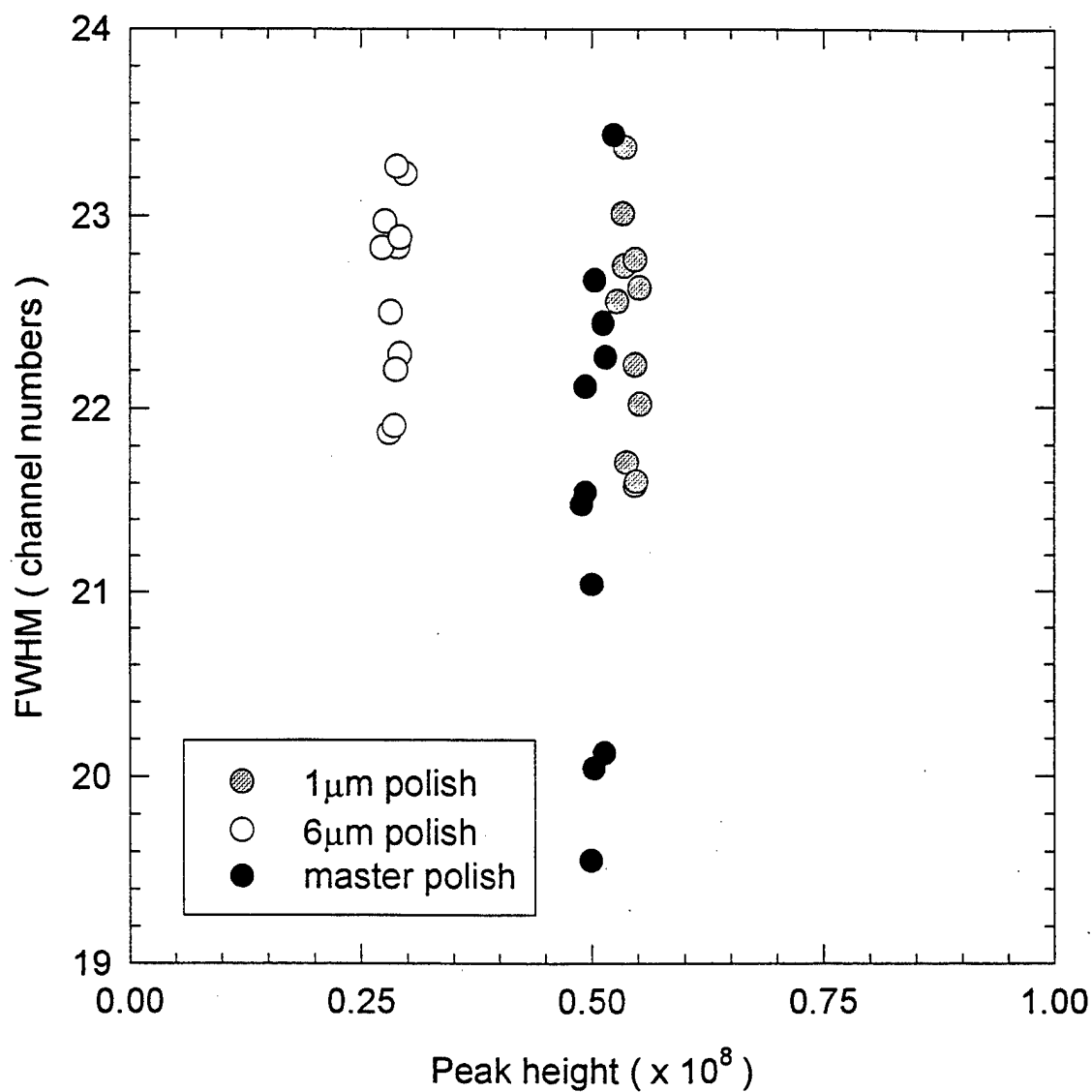
Ceramic (mediocre)

Figure 55   Rayleigh scattering comparison from a mediocre cylindrical rod (flat surface) after different polishes of 1 μm, 6 μm, and masterpolish

Ceramic (poor)
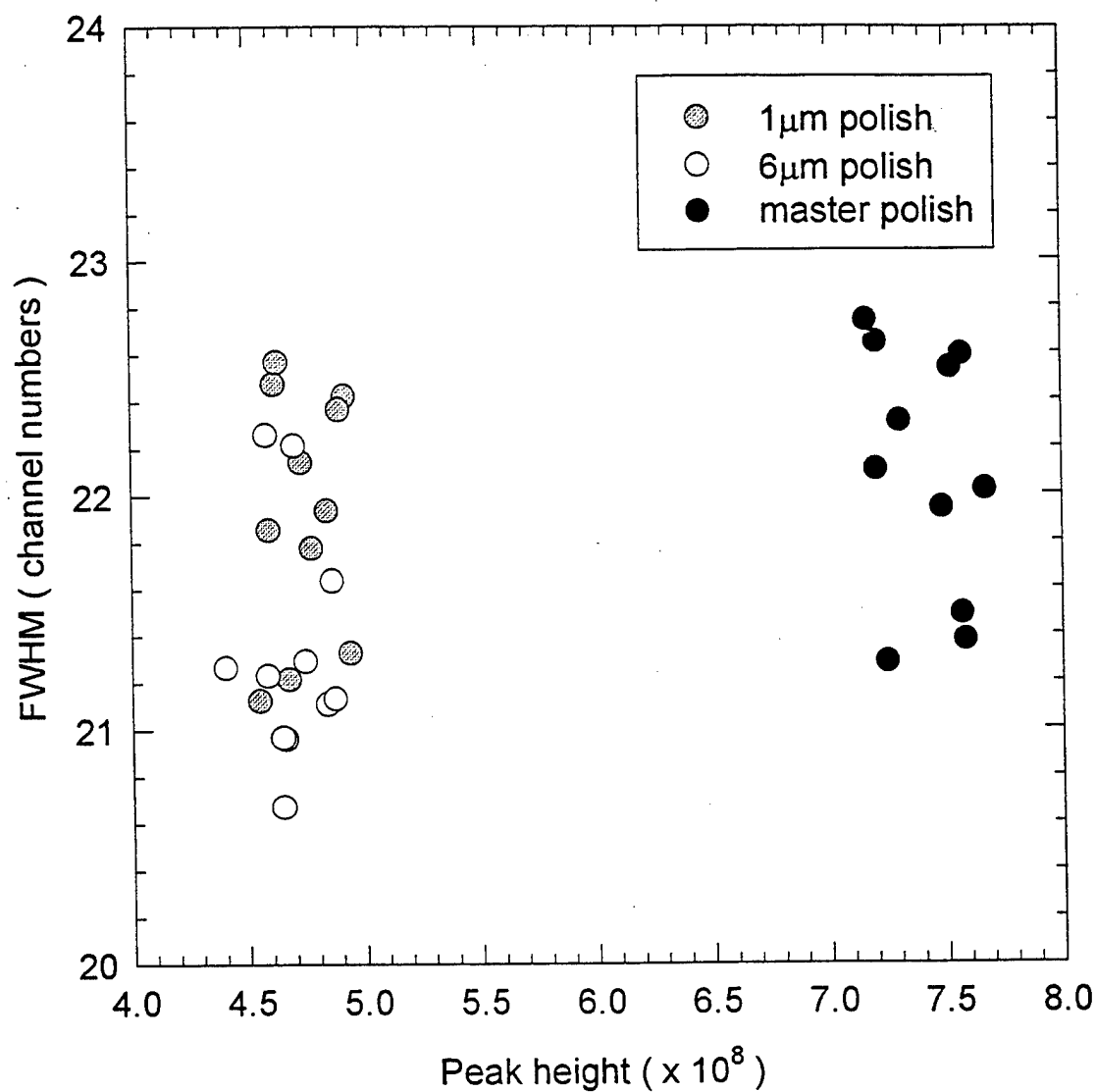
Figure 56   Rayleigh scattering comparison from a poor cylindrical rod
(flat surface) after different polishes of 1 μm, 6 μm, and
masterpolish

Ceramic
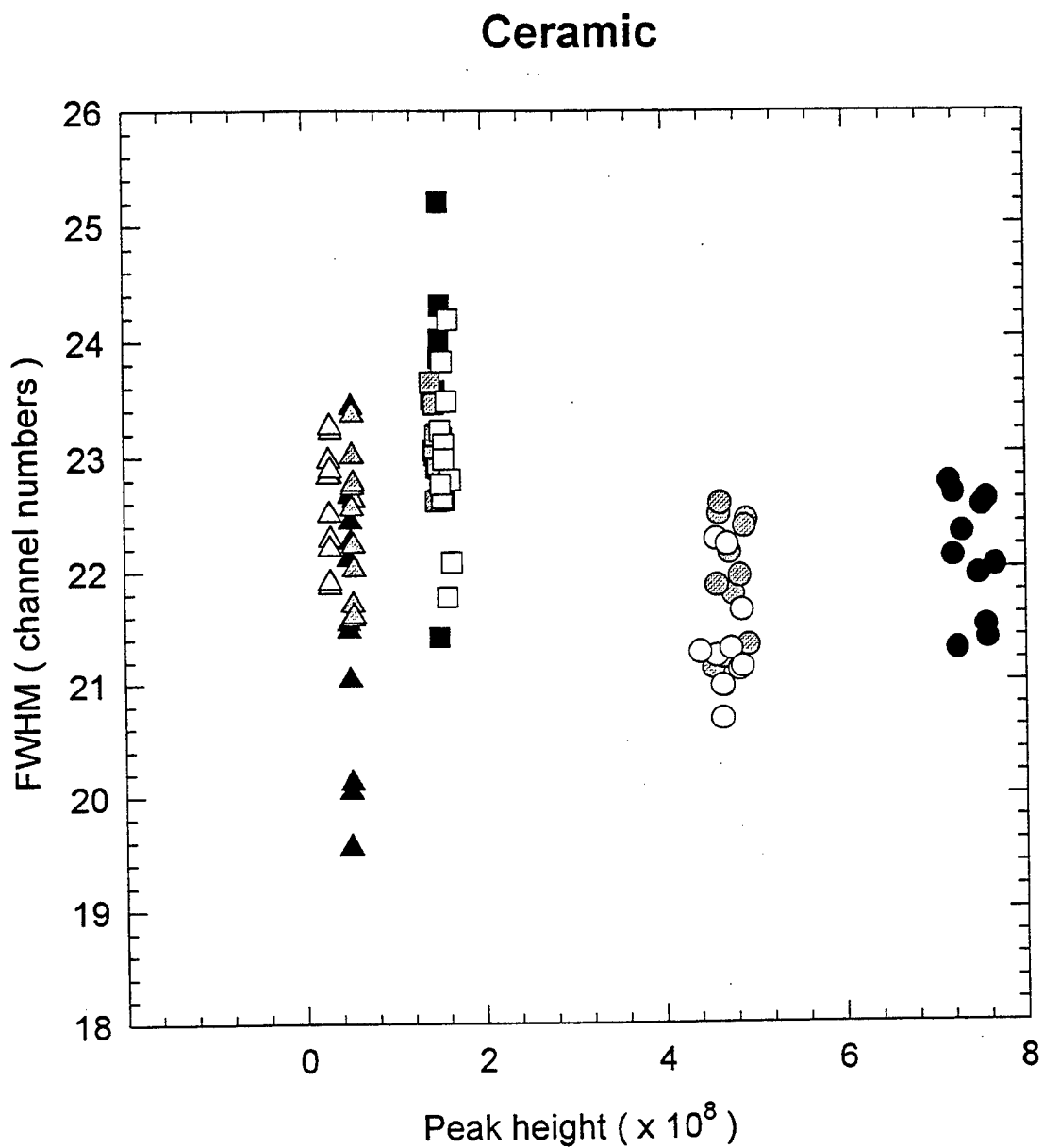
Figure 57   Rayleigh comparison from excellent, mediocre, and poor cylindrical rods after different polishes of 1 μm, 6 μm, and masterpolish

● poor - master
■ excellent - master
▲ mediocre - master
◎ poor - 1μm
▨ excellent - 1μm
△ mediocre - 1μm
○ poor - 6μm
□ excellent - 6μm
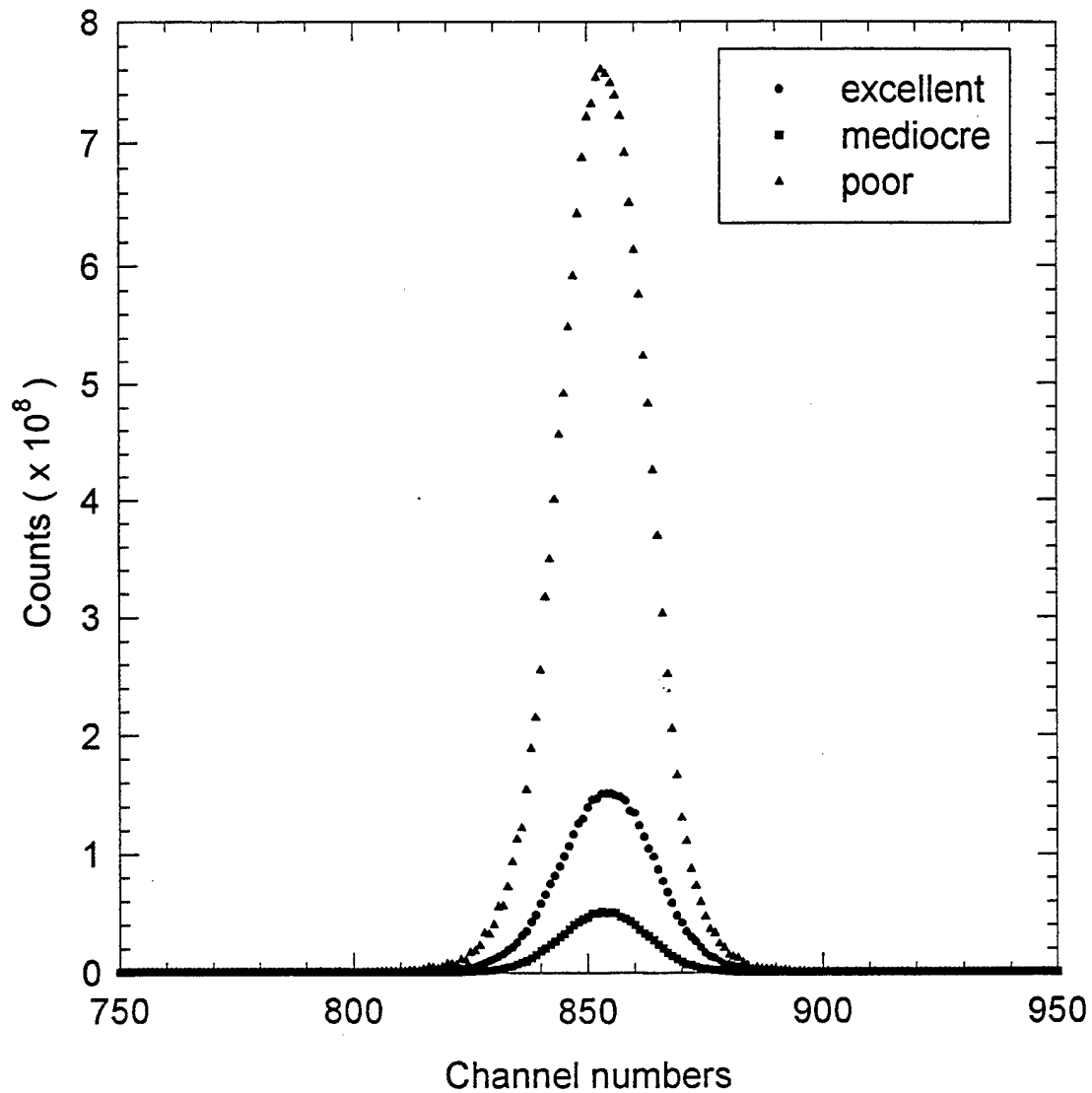△ mediocre - 6μm

Rayleigh scattering
Ceramic (curved side)
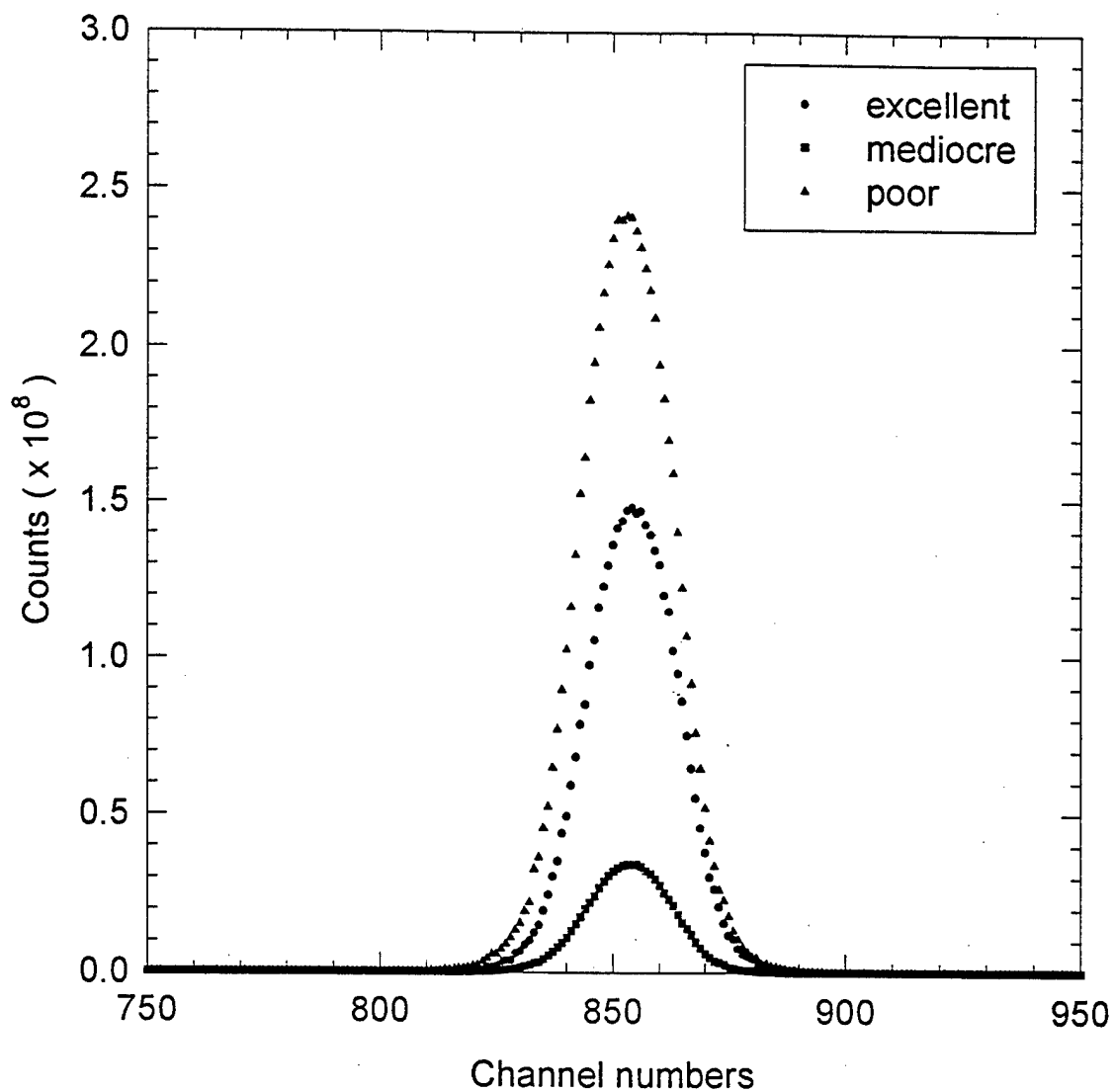
Figure 58 (a)   Rayleigh scattering from excellent, mediocre, and poor
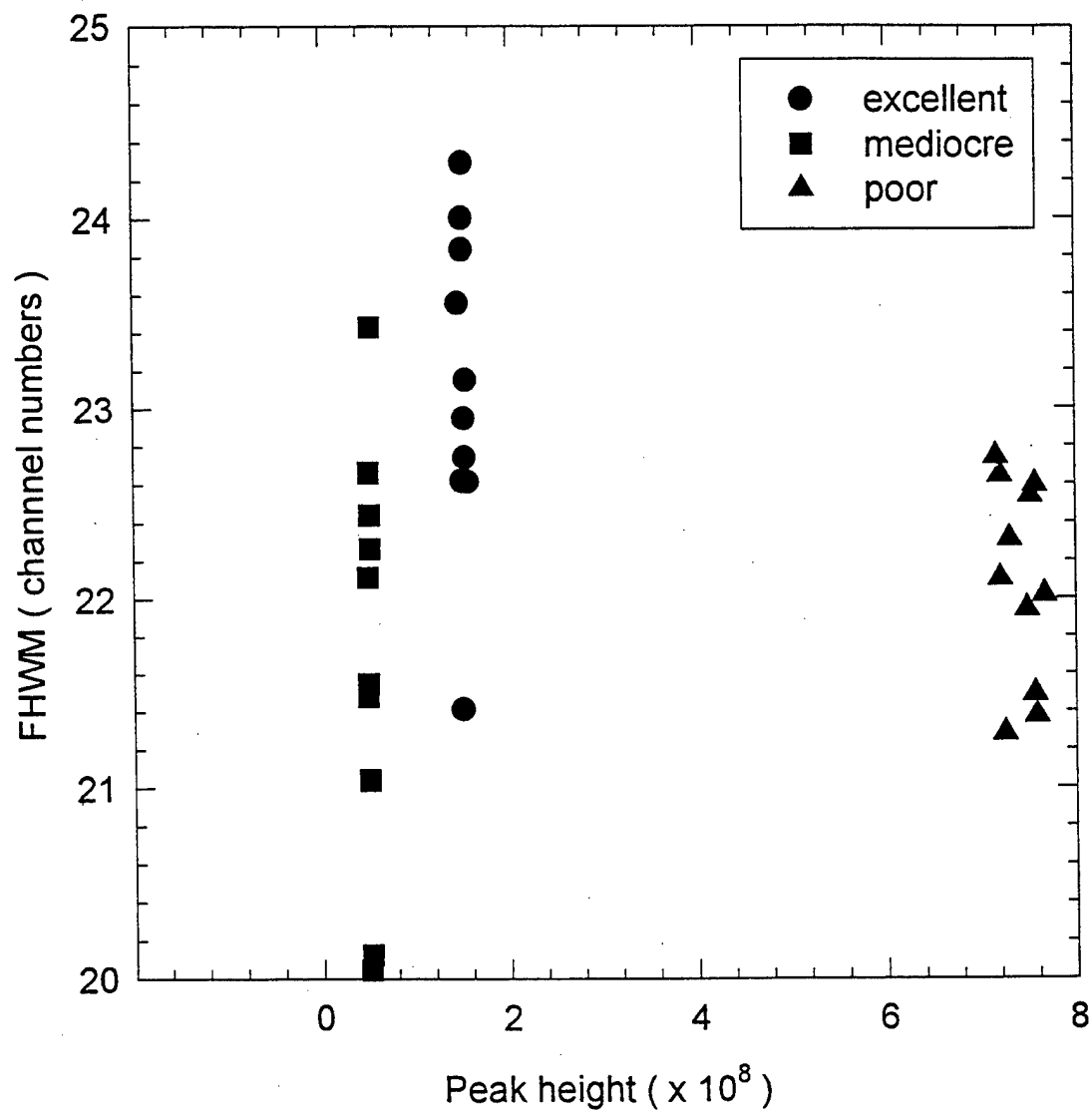cylindrical rods (curved surfaces) using System No. 2

137

Ceramic (curved side)
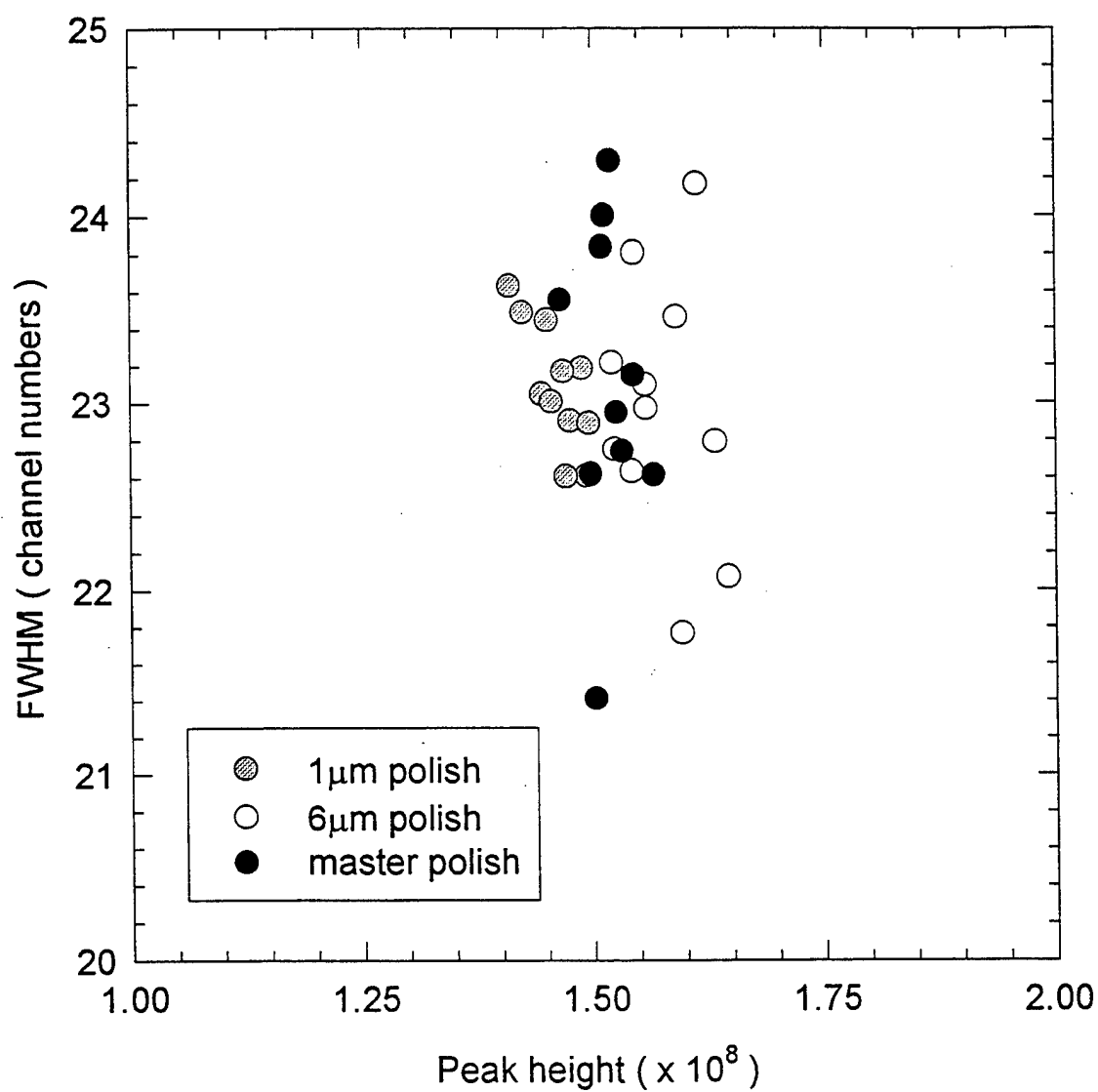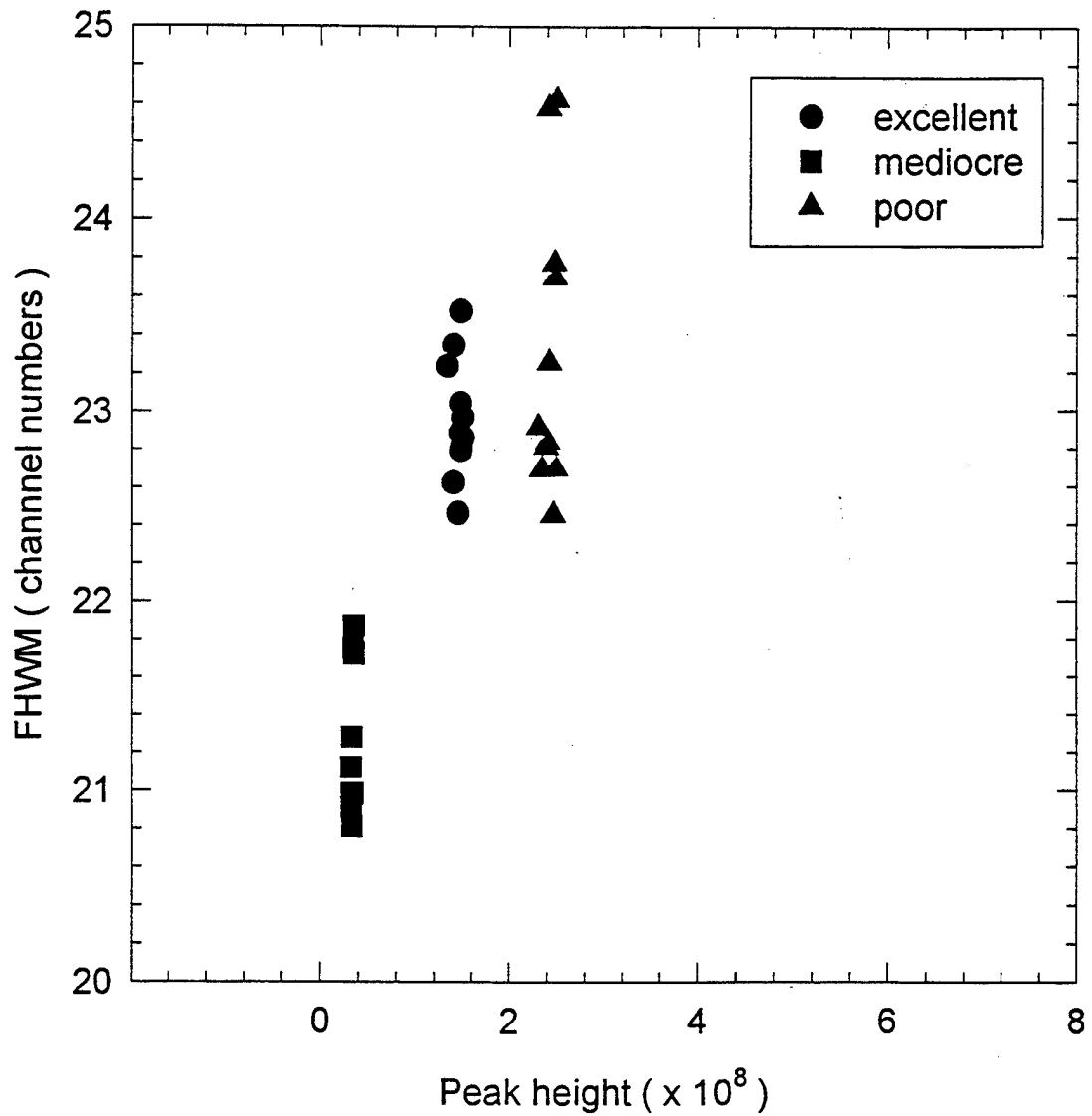

Figure 58 (b)   Rayleigh scattering results from excellent, mediocre, and poor
cylindrical rods (curved surfaces) using System No. 2

Rayleigh scattering
Ceramic balls
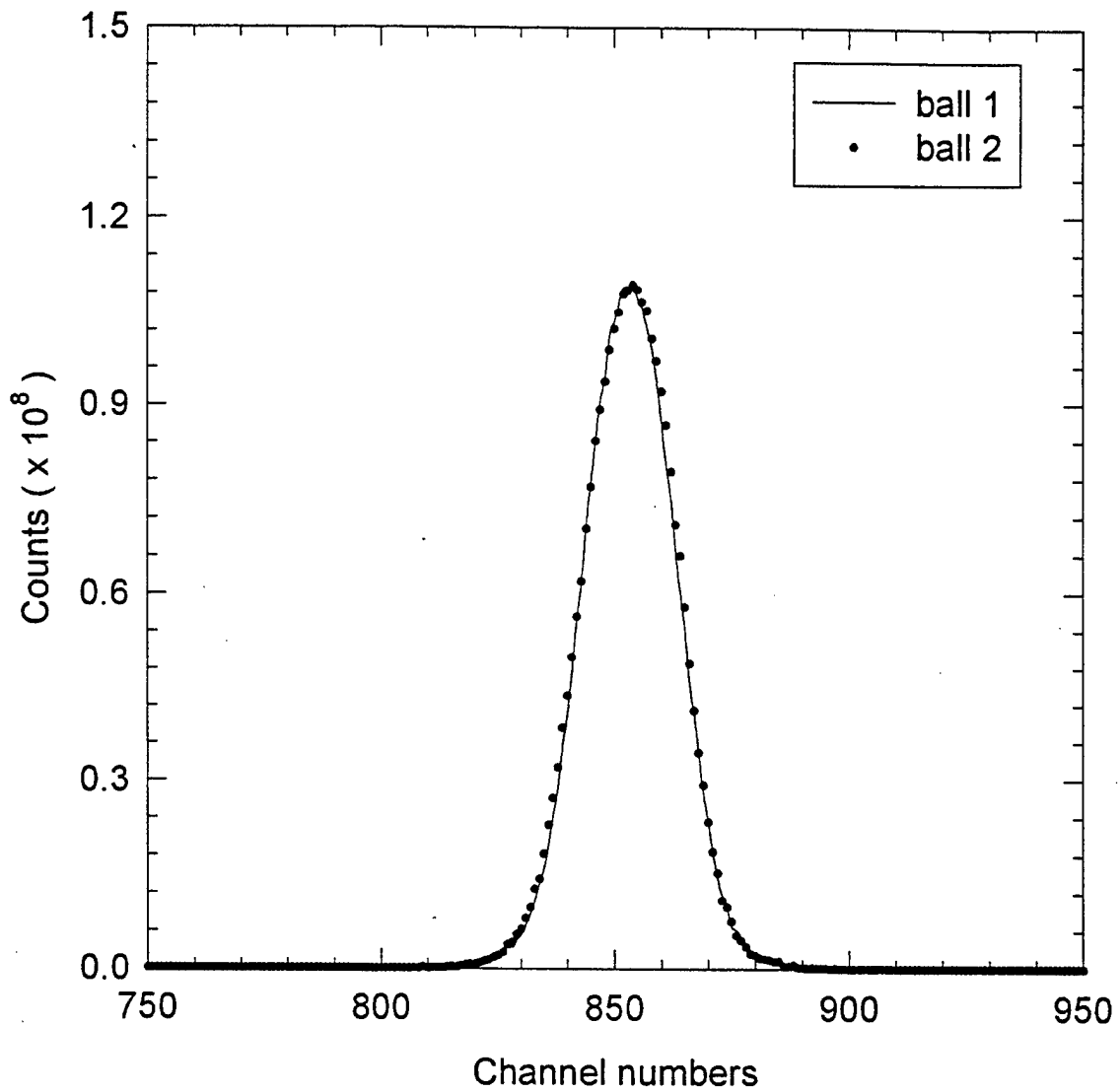
Figure 59 (a)   Comparison of Rayleigh scattering spectra from two ceramic
bearing balls obtained from the same lot

Ceramic balls
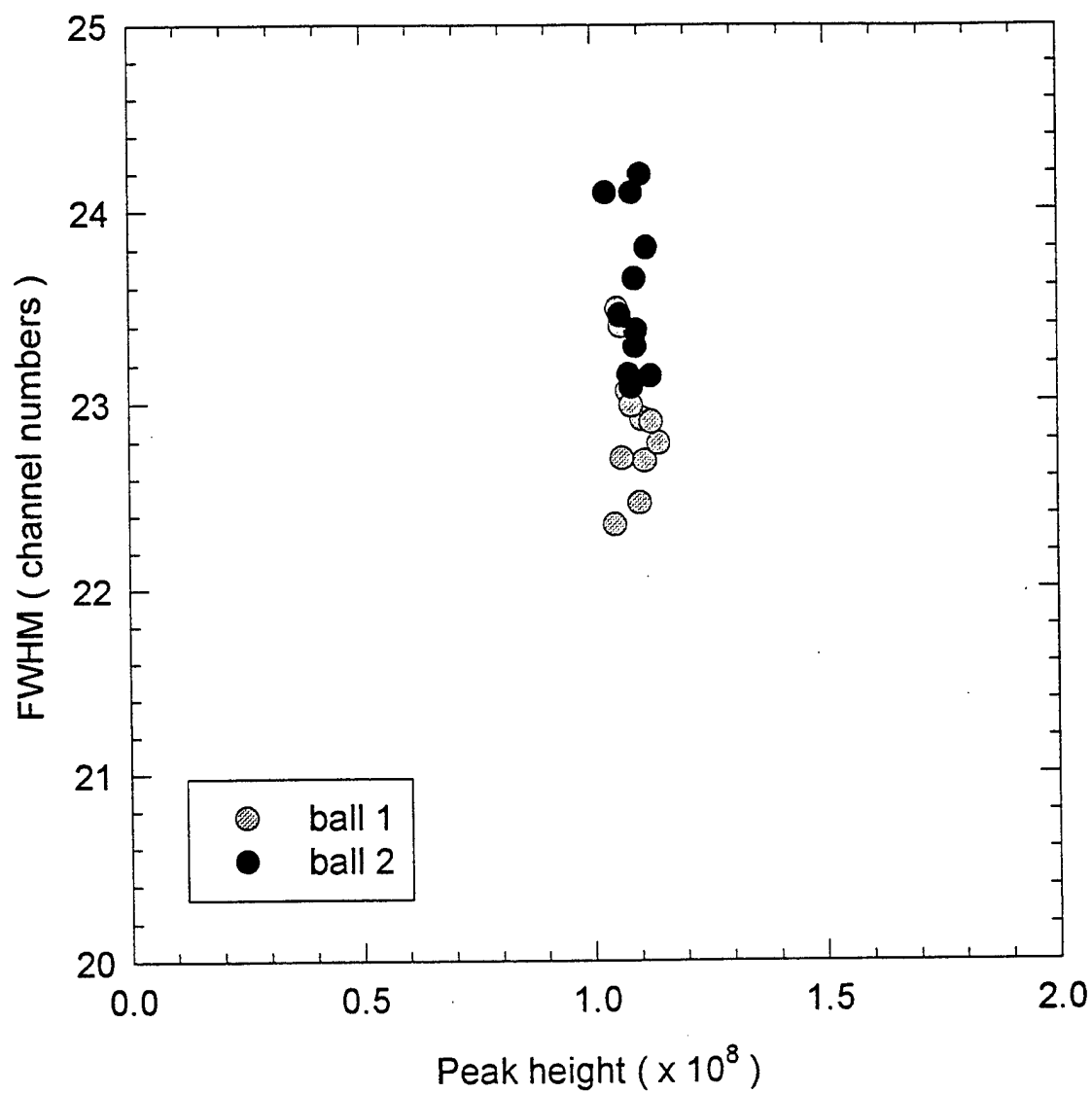
Figure 59 (b)   Comparison of Rayleigh scattering results from two ceramic
bearing balls obtained from the same lot

4.3.5 Task 5

Raman scattering on the three ceramics showed that although they were all Si_3N_4 materials, they each had different quantities of α phase and/or β phase Si_3N_4. This was one of the underlying reasons for their difference along with the various fluxing agents. The Raman scattering technique distinguished the three ceramics by simply monitoring the FWHM and peak shift of the second of the three Raman peaks.

The technique of Rayleigh-Brillouin backscattering also allows us to make that distinction rather clearly, simply by monitoring the peak height of the Rayleigh signal. Although this was a difficult experiment to do because of the care involved in micro-positioning the samples, it should be possible to computer control the positioning process. In a commercial application, it should be much easier to have greater quality control. All the necessary optics could be fixed, samples could be micro-positioned with a computer, variable optical density filters with much finer attenuation intervals could be used, faster discrimination and collection devices could be integrated into the configuration, data acquisition time could be minimized to several seconds by using a charged coupled device (CCD) instead of a PMT to detect the Rayleigh signal. The incident and reflected light could always be made to have to same preset angle while maintaining the same solid angle of collection. Since laser fluctuations could really hinder accurate differentiation, it should be possible to monitor the average laser output during the scans and keep only those data that fall within a preset norm (or tolerance) for the laser power. The whole process could be automated.

4.4 CONCLUSIONS

In conclusion, we find the technique of Rayleigh-Brillouin backscattering to be a viable means of differentiating between Si_3N_4 ceramic materials that have been shown to have different wear properties. Since there is a definite correlation between wear and Rayleigh signal, it should be possible to make a large database from extensive Rayleigh and wear measurements after which one should be able to determine the wear

properties from simple optical measurements. It can also be used to check consistency of balls from the same lot.

4.5 INFRASTRUCTURE DEVELOPMENT

The funds provided by ARPA for this project on non-destructive and non-invasive probing of silicon nitride ceramic materials has aided in the purchase of a state-of-the-art tandem Fabry-Perot interferometer system. This is the optimal system in performing Rayleigh-Brillouin scattering studies. The funds have also been used to help formulate a research project for a Ph.D. student.

4.6 TECHNOLOGY TRANSFER/COMMERCIALIZATION PLANS

A preliminary data bank has been constructed based on the Rayleigh-Brillouin backscattering studies in order to assess the surface quality of the silicon nitride ceramic bearing balls. In addition, the Rayleigh-Brillouin backscattering results are currently being prepared to be presented at conferences and in publications.

5. PHOTOACOUSTIC METHOD FOR NONDESTRUCTIVE TESTING OF Si3N4 CERAMICS

J. S. Krasinski and G. H. Miller
School of Electrical & Computer Engineering
Oklahoma State University
Stillwater, OK

5.1 SUMMARY

The goal of this study was to show the feasibility of using the Photo-Acoustic (PA) technique operating at the resonance frequency of the detector/sample structure. A review of the current literature on using thermal PA microscopy as a nondestructive testing technique for ceramic material has been made. An experimental apparatus for the study of this effect has been constructed and testing has been done.

Photoacoustic signals have been detected with a very high signal to noise ratio. It was found that imaging is rather slow using this technique. Shorter path methods of temperature measurement were proposed including interferometric measurement of thermal expansion and thermal radiation measurements. Lack of funding made progress very difficult. Some preliminary tests of the thermal radiation method were done using funds from the Laser Center. It was found that the method is very sensitive.

The thermal radiation method is orders of magnitude faster than the photoacoustic method. A few high quality maps of thermal conductivity with submicron resolution were recorded. A correlation between the technology of the sample, its strength and the thermal images was found on a few available samples provided by Allied Signal Inc.

5.2 INTRODUCTION

Photoacoustic Microscopy, sometimes called thermoacoustic imaging or PA microscopy, is based on the photoacoustic effect when the light beam has been focused down to a few µm in diameter and scanned across an area of the sample. There are three mechanisms which interact in the formation of a PA signal on a microscopic scale. Typically, one of the three mechanisms dominates, depending on the characteristics of the sample and of the experiment being performed. The three mechanisms are [1]

- absorption of light by the sample,
- generation and propagation of heat waves,
- production and propagation of acoustic waves.

Optical PA microscopy can be performed on optically nonuniform materials that have low absorption coefficient. An increase in the amplitude of the PA signal is caused by the light being absorbed more in some areas, for example by an iron filing inside a quartz crystal.

Thermally inhomogeneous materials possess sites that have thermal properties different from the rest of the material. Because the sites react differently to heat than the bulk of the sample, there is a change in the magnitude of the PA signal when the light is focused within one thermal diffusion length of the anomaly. The resolution of this technique is determined by the thermal diffusion length which, in turn, is determined by the thermodynamic characteristic of the sample and the modulation frequency of the light beam.

Acoustic PA microscopy requires ultrasonic frequencies because the resolution of the technique is determined by the acoustic wavelength. In most solid materials the acoustic frequency must be on the order of GHz to achieve a resolution of several µm.

PA microscopy (PAM) performed at frequencies in the 10 Hz to 10 KHz range is based on thermal waves which, due to slow propagation velocity, have very short wavelength and possess the required resolution to detect

144

flaws that can affect structural integrity of Si3N4 ceramics. These subsurface structures lead to catastrophic failure of the bearing balls. Due to the opaque nature of the ceramic material, optical inspection is inadequate for detecting the voids and cracks that are produced during the manufacturing of the ball bearings. Radiography requires thin samples for μm resolution and is not useful for objects greater than a couple of millimeters in thickness. Curved surfaces such as bearing balls make analysis by ultrasonic techniques difficult [2].

The PA effect was first reported by A. G. Bell in 1880. Bell used sunlight radiation and a carbon microphone as a detector. The resulting signal was very weak and interest in the effect quickly died away. The effect is weak since less than one ppm of the absorbed optical energy is converted to acoustic energy [3]. The recent increase of interest in the PA effect is derived from the advent of intense light sources (e.g. lasers and arc lamps), sensitive acoustic detectors (e.g. microphones, hydrophones, and piezo elements), the unique applications (e.g. spectroscopic studies of opaque materials) of PA, and the sensitivity of PA spectroscopy [4].

Absorption of intensity-modulated radiation anywhere on the sample results in a periodic, localized heating of the sample. Two mechanisms transmit this energy to the surrounding media. The first type of energy transfer is the heating of the immediate area by means of heat diffusion and conduction. The rate of heat transfer via this mechanism depends on the thermal diffusivity, α, of the material. The thermal diffusivity is described as:

$$\alpha = k \,/\, C\,\rho \qquad\qquad (1)$$

where k is the thermal conductivity, ρ is the density of the material, and C is the specific heat.

When the heating is periodic at frequency ω, then the distance of appreciable heat transfer into the sample medium is given by:

$$\mu = (2\,\alpha/\omega)^{1/2} \qquad\qquad (2)$$

Where μ is the thermal diffusion length [5]. The thermal diffusion length determines the resolution of PA microscopy (PAM) for subsurface flaws in opaque samples at modulation less than ultrasonic. Experimental results have indicated resolution for surface flaws to be on the order of the spot size of the focused laser beam [6].

The second type of energy transfer is a coupling of localized heat energy and the vibrational modes of the material itself. This is generally a nondissipative, thermoelastic process. Below ultrasonic frequencies, the distance over which the thermoelastic energy is transferred is limited solely by the dimensions of the sample or by some boundary conditions, and the speed of the transfer is determined by the speed of sound in the material [5]. The effect of sound-wave generation within solids under laser radiation was first observed by White [7] in 1963.

This effect, when coupled with methods to detect the sound wave and produce a well-focused intense beam of light, is utilized to produce PAM. The PAM technique is useful when utilized as a scanning technique. The two methods of generating a scanning PAM device are to move the sample under the laser beam or scan the laser beam over the sample.

The absorption of radiation which produces the generation and propagation of heat waves results in the production and propagation of acoustic waves. In principle, all three processes provide information about the microstructure of the sample being scanned due to nonuniformities of the material's optical, thermal and acoustic properties. In practice, the interaction between the sample, the light, and the acoustic frequency at which the light is modulated determines which process is dominant [8].

Thermally inhomogeneous samples can be opaque and the thermal diffusion length determines the resolution of the PAM as well as the sampling depth. The inhomogeneity of the material produce nonuniform heating of the sample within the volume determined by the thermal diffusivity (see equation 1), even though the optical power absorbed remains constant. These variations are transferred to the acoustic waves which are detected by an attached piezo audio pick-up or by a gas coupled microphone.

146

For analysis of condensed media the thermal diffusion length varies from about 1 mm to about 1 μm as the modulation frequency varies from 10 Hz to 1 MHz [9].

Ultrasonic waves can be used to detect anomalies within certain materials. Acoustic nonuniformities are spatial variations that alter the formation and/or propagation of sound (e.g. altered heat expansion coefficient, elasticity constants, velocity of sound, etc.). Such anomalies produce nonuniform excitation of acoustic waves in the volume of light/material interaction and alter the amplitude and phase of the acoustic wave once it has formed. When the effect depends on the formation of the acoustic wave, the thermal diffusion length is an important consideration in determination of the resolution. However, propagation of the sound through the sample media is affected by structures larger than the wavelength of the acoustic wave. The resolution of a 1 MHz acoustic wave is on the order of 3 to 6 mm. The upper limit of the acoustic frequency is a few GHz and is determined by the attenuation of the wave by the medium. An acoustic wave with a frequency of a few GHz has a resolution of several μm [10].

For Si_3N_4 ceramic material, thermal wave microscopy produces the most informative PA scan. The grain structure of the ceramic attenuates ultrasonic waves of frequencies high enough to detect voids of a few μm. The material is opaque, thus optical penetration is small when compared to the thermal diffusion length. For these reasons the amplitude modulation frequency of the laser beam is on the order of 50 Hz to 1 KHz and the thermal characteristics of the material are utilized in detection of flaws.

5.3 EXPERIMENTAL CONSIDERATIONS

Excitation Source

Consideration of the absorbance characteristics of the material being tested is of importance when selecting a laser source to induce the PA effect. The greater the absorbance of the exciting light by the test material, the greater the strength of the acoustic wave. The Si_3N_4 ceramic is a dark, opaque

147

material that absorbs light of blue as well as red wavelengths. The power that can be introduced to the samples is limited by the Curie point of the piezo detector which is attached to the sample. If the temperature of the piezo exceeds the Curie point, the microscopic polarized ferroelectric domains in the polycrystalline piezoceramic randomize their polarization, which ruins the detector. The laser is limited to operating at power levels below those that overheat the piezo.

Detector

Commonly, the PA signal is detected by either of two methods: the gas-coupled microphone or the piezo element detector attached directly to a condensed sample [10]. For condensed material such as metals and ceramics, the piezo element offers advantages over gas-coupled microphones. The mismatch in acoustic impedance that results in poor transfer of acoustic energy from a solid to a gas and then to a microphone is overcome by attaching a piezo element directly to the solid sample. Piezo elements offer superior frequency response over microphones, which is important when utilizing a pulsed excitation of the sample where the pulse widths may be small and result in a high frequency acoustic signal [11].

Depth of Observation and Resolution

The depth of observation and the resolution of the thermal wave imaging is determined by the thermal diffusion length. The thermal diffusion length is set by selection of the modulation frequency of the laser beam and is about 100 μm at 100 Hz [12]. The thermal diffusion length is found by equation 2. Figure 60 illustrates the change of the thermal diffusion length vs. modulation frequency, assuming thermal conductivity of Si_3N_4 equal to 0.072 [cal/cm s degC], density of 3.18 [g/cm^3], and specific heat of 0.17 [cal/g degC].

Optical Resolution

A well-focused laser beam of a known diameter has its size defined by the equation:
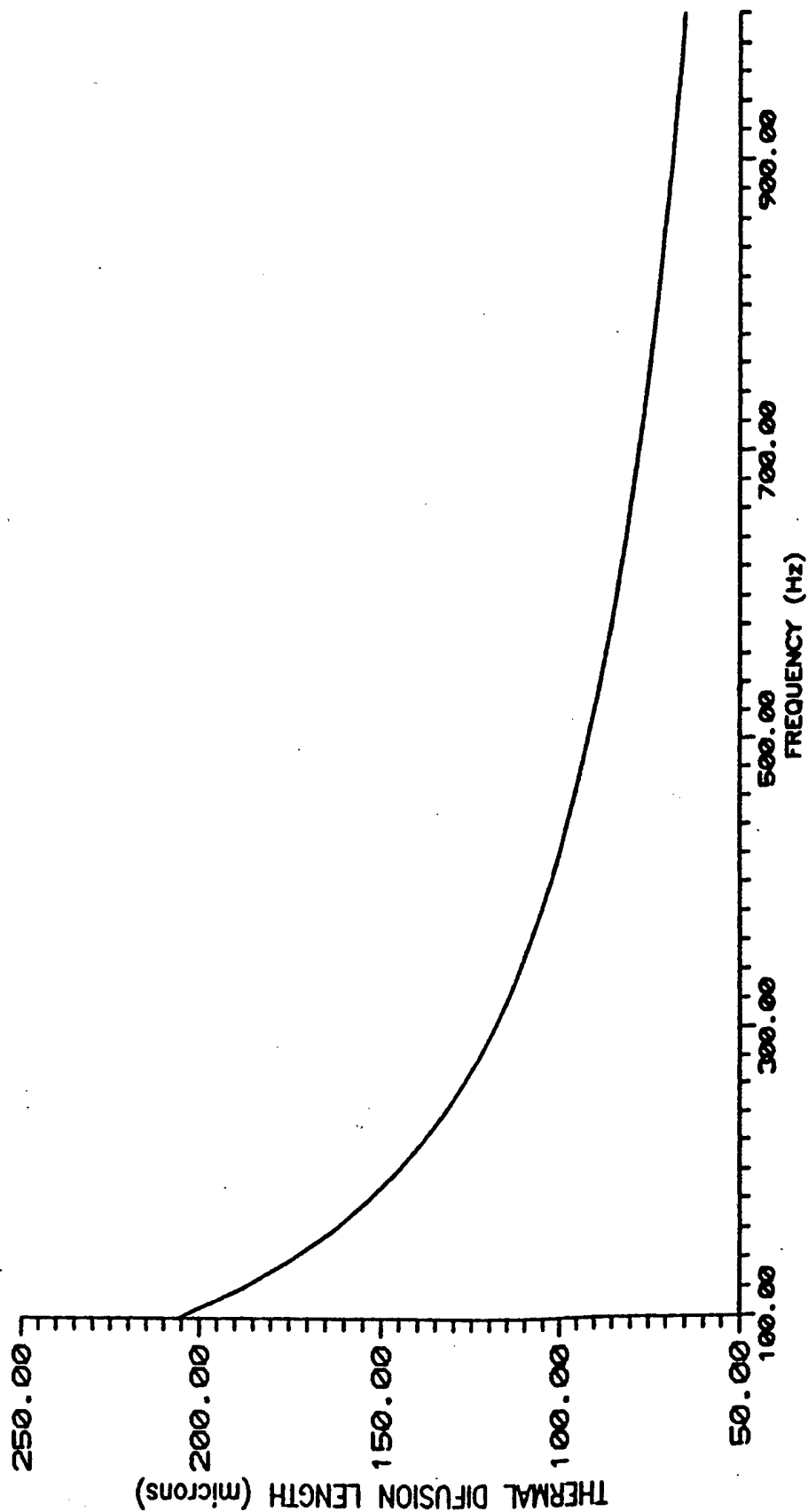
Figure 60   Variation of thermal diffusion length with modulation frequency for Si3N4 ceramics

149

$$ss = 2[1.68 \, \lambda/NA]$$
<div align="right">(3)</div>

In this approximation, the spot size, ss, is directly proportional to the wavelength, λ, and indirectly proportional to the numerical aperture of the lens, NA.

Adhesive

Matching the acoustical impedance of the sample and the piezo detector results in maximizing the transfer of the acoustic energy. The interface between these two elements should consist of a hard, brittle epoxy to optimize acoustic transfer. This can be achieved by adding extra resin to the epoxy mix and warming the adhesive as it hardens. Some experimentation is required with a particular epoxy to optimize the desired results.

Resonance

Once the sample/detector element is formed, the resonance of the device can be determined. A function generator used with an oscilloscope and a frequency counter provide the means of determining the frequency response of the element. The resonance of the element is useful as a preliminary filter for the PA signal. The detector/sample element can be considered as a damped harmonic oscillator acted on by a harmonic, external driving force. As a damped harmonic oscillator, the element's motion is a result of the interplay of a restoring force and a frictional force. The Q of the system is a measure of the degree of dampening in the system. A high Q system is slightly damped and the friction force is much smaller than the restoring force. Q is defined as:

$$Q = \frac{m\omega_o}{f} = \frac{\sqrt{mk}}{f}$$
<div align="right">(4)</div>

where m is the mass of the oscillator, ω_0 the natural frequency of the oscillator, k the force constant of the restoring force and f the friction factor for the retarding force. The amplitude of the steady state motion of the oscillator acted upon by a harmonic external force is given by:

<div align="center">150</div>

$$B = \frac{F}{if\omega[1 + iQ(\frac{\omega}{\omega_o} - \frac{\omega_o}{\omega})]} \tag{5}$$

Under conditions where the external force's frequency $\omega \ll \omega_0$ then B is approximately:

$$B = F/k \tag{6}$$

At the other extreme where $\omega \gg \omega_0$, B is approximated by:

$$B = F/m\omega^2 = F/k \tag{7}$$

At the resonance frequency, the steady state amplitude of the displacement of the oscillator is described by:

$$B = QF/k \tag{8}$$

At the peak of the resonance curve, the signal generated by the piezo, directly proportional to its displacement, is increased by a factor of Q. The noise in the system is approximated by a white noise model and has the same magnitude at resonance as at other frequencies. For this reason the signal to noise ratio at ω_0 increases by the factor Q and the resonance of the system acts as a bandpass filter centered on ω_0.

The PA signal is rather small compared to the noise produced in a photoacoustic microscope system; therefore, the signal must be extracted from the noise. The lock-in amplifier performs this task and is capable of measuring nanovolt signals. The amplifier has differential input for the signal source and a reference input to synchronize it with the modulator of the excitation source. The reference frequency, supplied by the modulator, determines the frequency and phase of the detected signal. The amplifier is equipped with electronics that allow phase shifting of the signal. This feature compensates for time differences produced by a delay time between the stimulus arriving to the sample and the arrival of the signal to the lock-in amplifier. To optimize the filtration, the lock-in has a mixer that shifts the

input signal to O Hz (DC). This allows for minimizing the width of the bandpass of the filter and optimizing the signal to noise ratio.

5.4 THE PHOTOACOUSTIC MICROSCOPE SYSTEM

Excitation Source

Figure 61 illustrates the experimental setup used to detect the PA signal. The Ar-ion laser was a Spectra Physics 171 operating in multiline mode (457.9 - 514.5 nm). Typically, the laser was operated at an output power level of 100 mW, in continuous current mode. Operating at this power level assures not overheating the piezo detector. Diffraction rings were eliminated from the laser beam by using an appropriate negative lens and an aperture. The microscope's focusing objective input pupil's diameter was measured and the aperture allowed the laser beam to just fill the lens. The 50x lens (NA of 0.75) focused the laser beam to about a 2 mm spot size.

The chopper (Standford Research System, Model SR540) was adjusted to maximize the output of the resonance peak, between 320 to 380 Hz.   Phase was then checked and selected for maximum output and then the chopper was reset until frequency and phase were determined to where output was maximized at the resonance peak. The chopper was acoustically isolated from the table by placing it on a brick resting on bubble wrap packaging material. The resulting vibrational mismatch between the materials effectively isolated the chopper.

Sample Preparation

A diamond saw was used to slice off a section of the Si_3N_4 bearing ball. Epoxy was used to attach the section to a piezo ceramic transducer (Piezo Systems, Inc. G-1195 ceramic material). The piezo transducer measured 0.75" x 1.5" x 0.020" and was poled for operation. The piezo ceramic material has a density of 7.5 g/cm3 and sound velocity of 0.325 cm/ms which produces an acoustic impedance of 2.438×10^6 g/cm^2 s. The Si_3N_4 material has a density
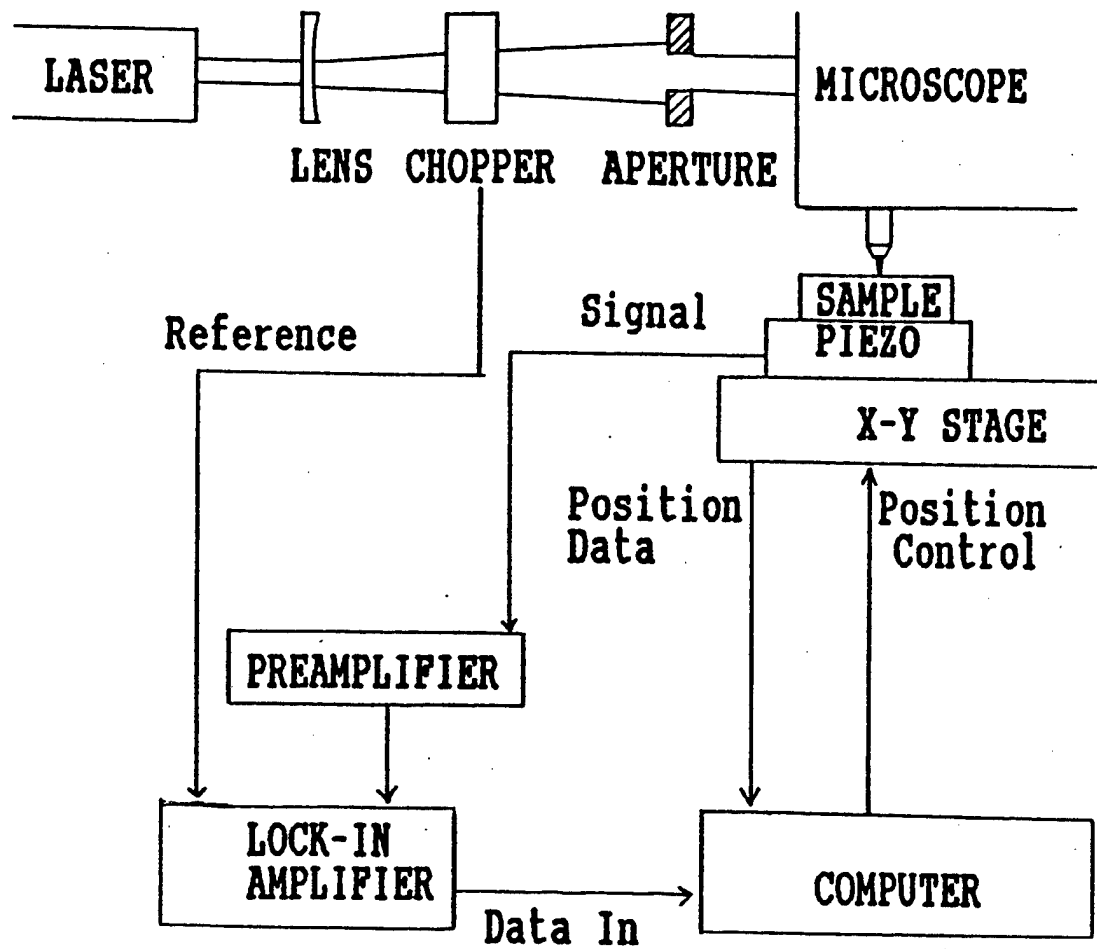
Experimental Apparatus

Figure 61   Bloack diagram of photoacoustic microscope

of 3.3 g/cm^3 and a sound velocity of 1.18 cm/ms [11, 12] which gives an acoustic impedance of 3.894 X 10^6 g/cm^{2}s.

Signal Generation and Data Collection

The voltage generated by the detector/sample element was picked up by two electrodes between which the detector was clamped. The lock-in amplifier (Stanford Research Systems, Model SR510) detected the preamplified (Stanford Research Systems, Model SR550) signal at the frequency set by the chopper and delivered an output to the computer (Everex 486-33) proportional to the voltage generated by the detector. The computer controlled the X-Y stage (Physik Instrumente, Model M-016.00) and received position data from the DC-Mike drives (Physik Instrumente, Model M-224.00). The computer program used to gather the data sampled the analog/digital (A/D) converter once every 100 ms so the time constant on the lock-in amplifier was set to 100 ms. The control board for the DC motor mikes also contained the A/D converter which simplified data collection. The data file generated contained X-position, Y-position, and the PA signal from the lock-amplifier.

Reduction of Noise

The detector/sample element must be acoustically isolated to reduce the noise to an acceptable level. The vibrational noise present coupled into the detector by two routes: direct coupling and air coupling. Air-coupled noise resulted from sound occurring at the same frequency as the chopping frequency. The detector showed sensitivity to sound such as closing doors, clapping hands, and a variety of others. Although the acoustic impedance mismatch between air and the piezo was high, there was enough energy transferred into the piezo to warrant a sound dampening enclosure to be built about the detector/sample element. When the sample was firmly fixed to the optical table in order to optimize optical alignment, vibrations were picked up by the table and coupled directly into the detector. The optical table was floated on air-filled pistons that isolated the table from vibrations in the floor, but the table was not anchored in any manner that dampened vibrations present in the air and so acted as a vibrational antenna, channeling

vibrations into the detector. Floating the table reduced the noise level by more than two orders of magnitude, but the detector needed to be acoustically isolated, using a sound barrier composite sheet between the table and the microscope on which the detector was mounted to reduce the noise to an acceptable level.

Sensitivity of the detector was enhanced by operating at the resonance frequency of the sample/detector element. To determine where the resonance frequency occurred, a function generator (Hewlett Packard, Model 3311Al) was attached to the element through a 430 pF capacitor. The frequency was measured by a Tektronix 2236 100-MHz oscilloscope operating as a frequency counter. The voltage generated by the piezo was measured by the oscilloscope referenced to the function generator. Figure 62 shows a typical frequency response curve generated using this method.

5.5 OPTIMIZATION OF PHOTOACOUSTIC MICROSCOPE

Data Collection

The optimization of detection of the PA signal required testing the experimental system under various conditions. The noise was determined by observing fluctuations of the signal at one location on the sample. The laser beam was blocked to generate a zero reference level and then was allowed to stimulate the sample to generate a signal when testing for noise contribution from some variable. The sample was not scanned so that the signal would be free of additional vibrations and so that there would be a constant absorption of the laser beam by remaining on one particular grain of the material. Each data point in any given experiment represents the average of 50 - 10,000 individual samples and there are forty data points. The number of individual samples varies from experiment to experiment but is constant for a given experiment. By increasing the number of samples by a factor of ten the noise improved by the square root of ten.

The lock-in is equipped with three electronic filters which, when tested, showed that a reduction in noise occurred when all three were
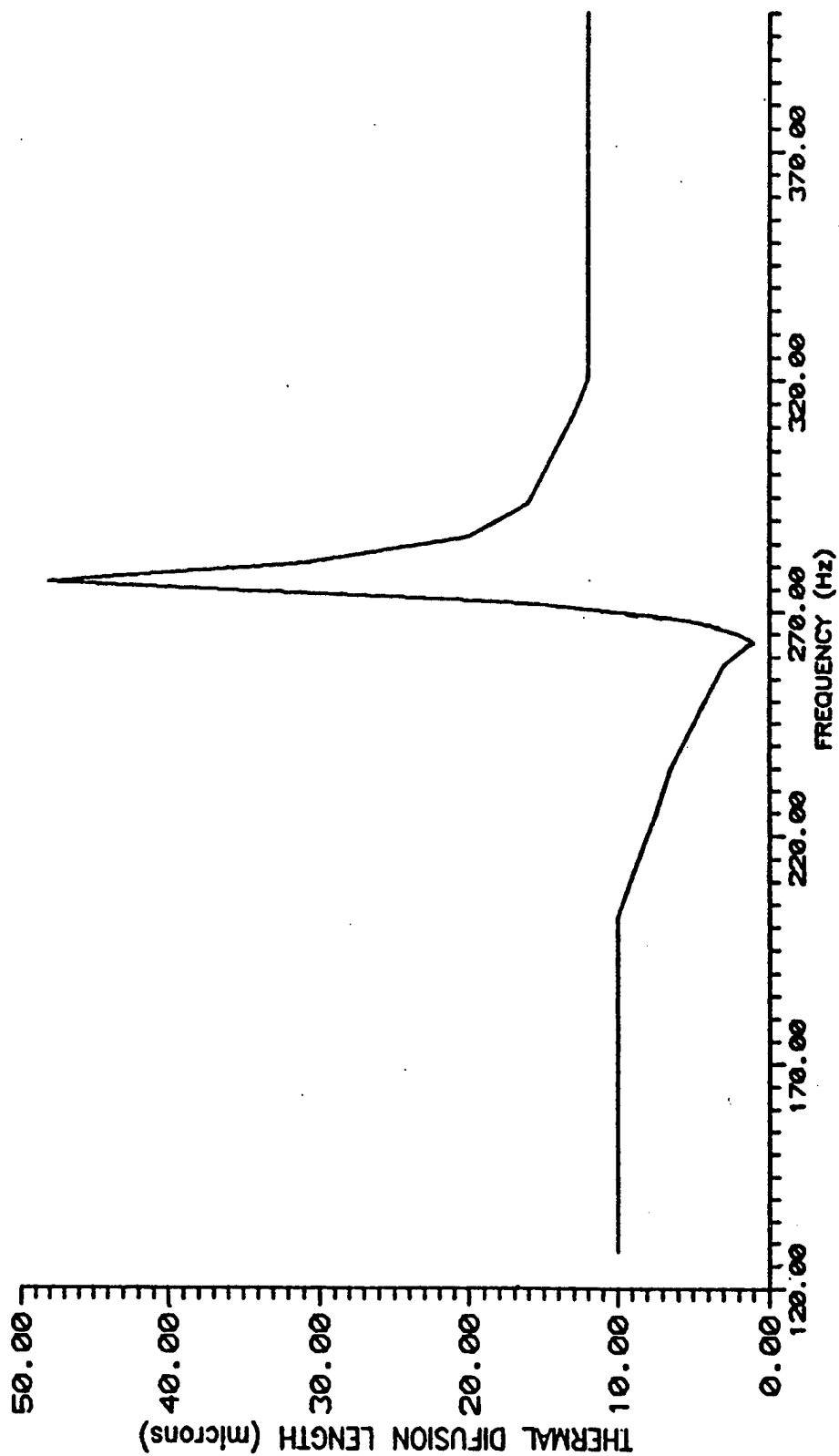
Figure 62   Frequency response of the piezoelectric resonator showing parallel and serial resonances. FWHM=7.2Hz, with peak at 276.4 Hz and Q=38.4

engaged. The dynamic resolution was found to have very small effects on the noise generated in the PA signal, but the best results were obtained when the dynamic resolution was set to low. Another technique for reducing the noise in data collection was altering the time between the motor coming to a stop and the start of sampling the PA signal. A comparison of the scans recorded with a 10 s pause and a 15 s pause between a motor halting and the computer beginning sampling the signal showed a large drop in noise level with the longer pause of 15 s. The lock-in was equipped with an option that allowed the noise to be monitored. This option was used to measure the noise as the pause time was varied from 5 - 120 s. The results of this experiment show that the noise decays to a constant value after about a 45 s pause time. We did not manage to find what was responsible for this type of noise.

Optical Effects

Optical absorption of the laser beam determines the intensity of the resulting PA signal. The surface of the Si_3N_4 material has dark areas on a light background when observed under a reflective microscope. The laser beam was focused onto a dark grain and the resulting signal was recorded. Similar measurements were done again except the laser beam is focused onto the reflective background material of the Si_3N_4. Comparison of signals shows that the intensity of the acoustic signal is 10 to 15% stronger for the darker, more absorptive grain. The variations in output of the laser which would affect the output signal is of concern and the laser power can be monitored and the data can be used in normalization to compensate for the laser fluctuations.

The experimenter must be aware of nonuniform optical absorption in the sample when searching for flaws. Optical inspection of the sample surface where a suspected flaw has been located will reveal if the effect being measured is due to thermal inhomogeneity, and therefore a flaw, or if there is an optical inhomogeneity influencing the PA signal.

Electrical Effects

A significant stabilization of the PA signal was realized when a 330 KΩ resistor was placed across the electrodes of the piezo element. This resistor allows for the dissipation of the static charge collected on the capacitive piezo element. The alternating charging and discharging of the piezo resulted in a drifting baseline. To test for signal distortion the 330 KΩ resistor was attached in parallel with a piezo element identical to the detector. This structure was attached to a square wave generator and the resulting wave form was observed using an oscilloscope. There was little distortion in the wave form, even with a 200 KΩ resistor. The stability of the PA signal was greatly improved with the addition of the resistor. Various cables were tested by placing them between the detector/sample element and the preamplifier. The double shielded cable transferred the signal with the least noise and was used throughout from detector to lock-in amplifier. Although most of the cables produced little noise, the double shielded cable showed a less erratic behavior over several test scans than the other cables. A reduction in the electrical noise occurred when line filters were placed on the power cords of the computer and the lock-in amplifier. By using the noise level output of the lock-in, sources of noise could be traced. It was found that prior to placing the line filter on the computer the noise measured by the lock-in increased from 25 mV to 52 mV upon activating the computer. After several improvements were made, including attaching the line filter to the computer (the lock-in amplifier already had one installed), the noise would change from 2.6 mV to 2.8 mV by turning on the computer.

Vibrational Isolation of the Detector

The noise introduced into the system by external vibrational sources has been detrimental to the observation of small changes in the PA signal. Floating the table and isolating the table from other sources of noise reduced the noise signal by more than two orders of magnitude. However, the table and the detector were affected by sound transmitted through the air; the system reacted to closing doors, sounds from adjoining rooms, and music played over the radio. Any vibrations, no matter how generated, showed up in the scan. All movable and unnecessary items in the room that were

sources of noise, like the recirculating pumps and the heat exchanger, were moved to an adjacent room. Water hoses were acoustically isolated from the table. The detector was enclosed in a box with sound dampening material. These changes resulted in further reduction of noise coupled into the detector.

5.6 RESULTS

Noise Levels

Once the isolation of the system from sources of noise had been improved, the PA signal generated had a signal to noise ratio (S/N) of about 125. Figure 63 illustrates an experiment performed after isolation was optimized.

To determine whether the source of the remaining noise was electrical or vibrational in nature the following experiment was done. The piezo transducer was removed and the electrodes were terminated with a 50 Ω resistor. The chopper and the lock-in amplifier were on and the noise, as measured by the lock-in amplifier, was recorded as 164 nV. Activating the computer and the monitor increased the noise to 170 nV. The measurements were repeated with the piezo transducer in place. There was some increase in the noise which indicated further acoustical dampening would be beneficial.

Reproducibility

Reproducibility of multiple scans over the same region of ceramic material has been enhanced. Figure 64 depicts the results of three scans repeated over the same area of the bearing ball. All three scans show the same general profile but the noise in the signal is still excessive, overshadowing details that would indicate the presence of a flaw. While it is not conclusive, there is some promise of positive correlation in the results which encourages further investigation. We found that the acoustic method would require a rather expensive sound isolation system. While a
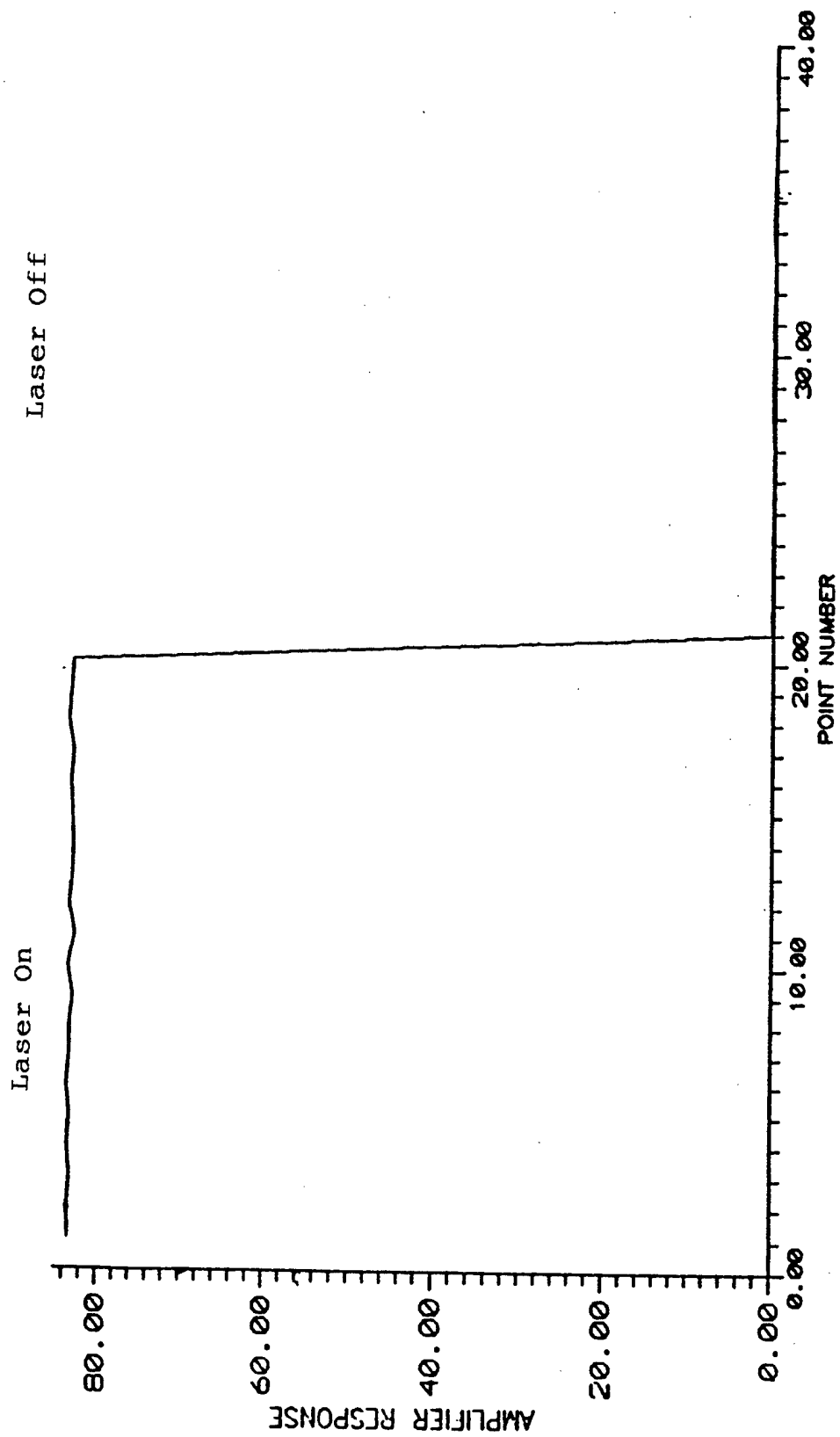
159

Figure 63   Experimental signals after optimizing isolation of the photoacoustic system
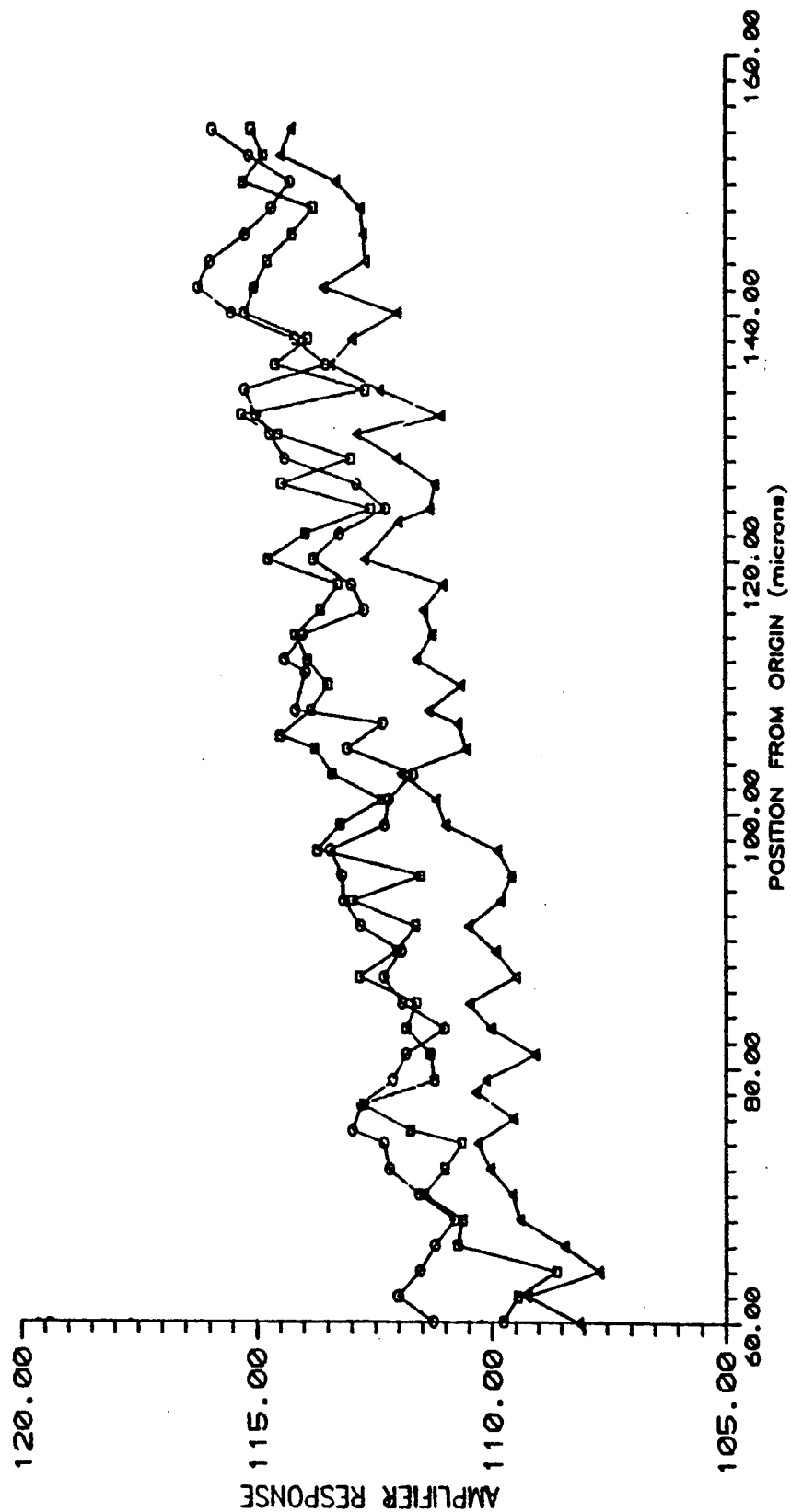
Figure 64   Three scans over a region of Si$_3$N$_4$ sample to verify
reproducibility of photoacoustic scans

161

system like this could be constructed, our limited funds made this approach impossible. We started to look for alternative methods of detection of the thermal waves.

5.7 ALTERNATIVE DETECTION METHODS

Introduction

While the signal to noise ratio equal to 125 would be considered very good for many measurements it has not been adequate for detection of the small variations in the acoustic signal brought about by surface or subsurface flaws.   Alternate methods of measuring the surface deformations of the material could potentially be free of acoustic noise.

Michelson Interferometer

The alternate heating and cooling of the ceramic surface produces periodic expansion and contraction of the material. Thermal diffusivity and chopping frequency determine the size of the area that bulges outward upon heating and the depth of heat penetration prior to a cooling phase. The degree of bulging and contraction is determined by the thermal expansion, specific heat, thermal conductivity, and density of the material. If a particular volume has a flaw within it, the material's thermal properties are altered and there is a change in the magnitude the surfaces bulges. Optical interferometry can measure changes in a surface position on the order of a fraction of an optical wavelength. It is anticipated that the bulging would be large enough to monitor using a Michelson interferometer.

Mounting the sample on a rigid platform firmly affixed to the optical table that the small probe laser is on results in a substantial reduction of the acoustical noise. The periodic heating of the sample would be done by a high power excitation laser operating at a different wavelength than the weak continuous wave probe laser.   Using two lasers provides continual observation of the surface by the probe laser while exciting the surface in a periodic manner with the strong laser.   In addition, due to direct, high

sensitivity interferometric observation of surface deformation, detection of the flaws is enhanced. In the proposed system, the exciting laser is chopped while the probe laser, operating at a different wavelength, is continuous and is used as a light source for the interferometer. Since the probe laser operates continuously, there is no problem with losing the image of the fringes. It is worth noting that such methods are already accepted as the most sensitive arrangement for gravitational wave detectors, and there is a lot of literature on the properties and optimization of such systems [13].

The optical interferometry system allows use of a feedback control system to eliminate the effects of temperature and other slow vibrational fluctuations. The setup (Figure 65) utilizes two lasers operating at different wavelengths, one at l1 and the other at l2. The excitation beam at wavelength l1 is amplitude modulated by the chopper. Mirror M1, being highly transparent to λ1 and highly reflective to λ2, mixes the beams of the two lasers. The Michelson interferometer is created from splitter S1 (highly transparent to λ1 and is a 50% beam splitter for λ2), mirror M2 (highly reflective for λ2), and the specimen (acting as a reflector). To maximize sensitivity, the lengths of the interferometer's arm should be adjusted to where measurements are made at half the maximum value of the fringe intensity. The reference beam is compared to the sample beam using a differential amplifier, and the output is passed through a low-pass filter. The feedback for the control system is provided by PD1 and PD2 photo diodes monitoring the intensity of the laser beam at M3 and M4. These two mirrors are 90% reflective, thus the original beam (reference) and the interferometer's beam (sample) are monitored. The difference between the signals of PD1 and PD2 is amplified and determines the adjustment of the length of the Michelson interferometer to a position corresponding to equal input signals. The low-pass filter of the control system allows for data collection without interference from the control system and prevents the control system from responding to the changes induced by the excitation laser. The lock-in amplifier samples the fringes at a rate set by the chopper. The use of optical interferometry provides a direct measure of the PA effect. Sensitivity of this direct method should be much greater than using an attached piezo.
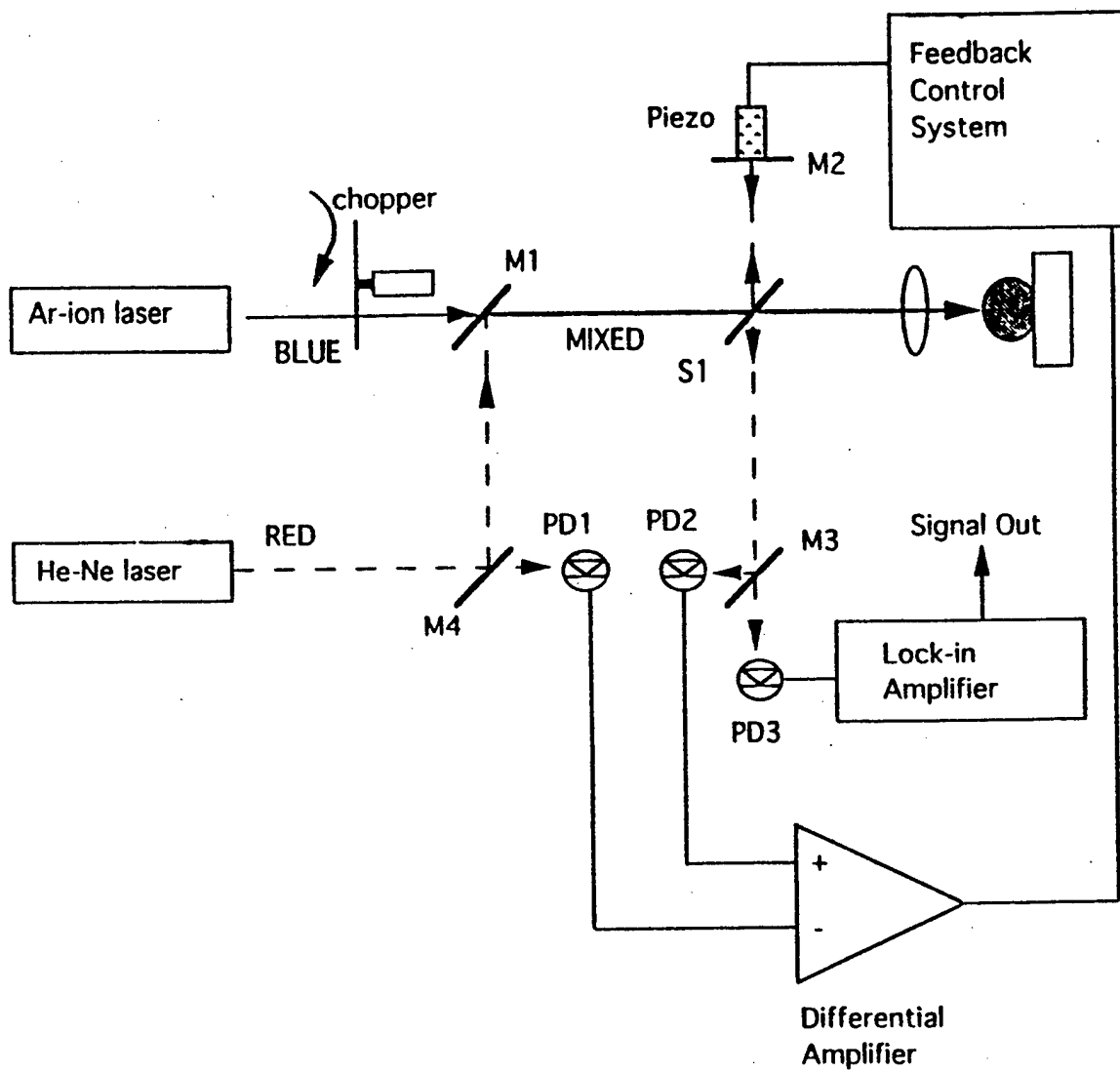
Figure 65   Block diagram of Michelson interferometer system

164

Infrared detection of thermal waves

The temperature changes of the area heated by the exciting laser can be directly detected by an IR detector in a system as presented in Figure 65. Ideally one would use an IR detector sensitive in the several micrometers range corresponding to maximum emissivity range of black body at a temperature of few hundred Kelvins. Detection of 5 μm radiation requires different optics than the microscope optics used to focus the laser beam on the sample since glass lenses strongly absorb the infrared radiation. A good compromise wavelength that the microscope is transparent to and that allows for observation in the anticipated temperature range is about 1.5 μm. Flaws present in the bearing ball would produce changes in the thermal characteristics of the material and the amplitude of the thermal wave of the area being observed.

Experimental effort on alternative methods of thermal wave detection

A new experimental interferometer based system was made and ready for use but lack of funding made continuation of these experiments not possible. We managed to get the OSU Laser Center interested in this type of research and with limited funds transferred from the Laser Center were used to make some experiments with IR detection. Therefore, the experimental system was rebuilt according to the infrared detection scheme. We used a low noise liquid nitrogen cooled Ge detector to monitor IR radiation from the ceramic, illuminated by a focused argon laser beam. Power up to 100 mW was used. The detector produced a very strong and clean signal. Using the translation of the sample by the computer controlled x/y translation stage we obtained high quality images of the samples as presented in Figure 66 (a) and (b). As one can see, non-annealed sample shows large areas of homogeneous, and rather low signal, with small isolated areas of a very large signal (up to 100x more than average). Optical microscopic examination of the samples did not reveal anything visible at these areas. The annealed samples show much smaller relative amplitude of the peaks suggesting that the annealed material is far more homogeneous. It is worth noting that these experiments were made with a non optimal Ge detector, with cut off wavelength of approximately 1.6 μm. An InSb detector with sensitivity extending beyond
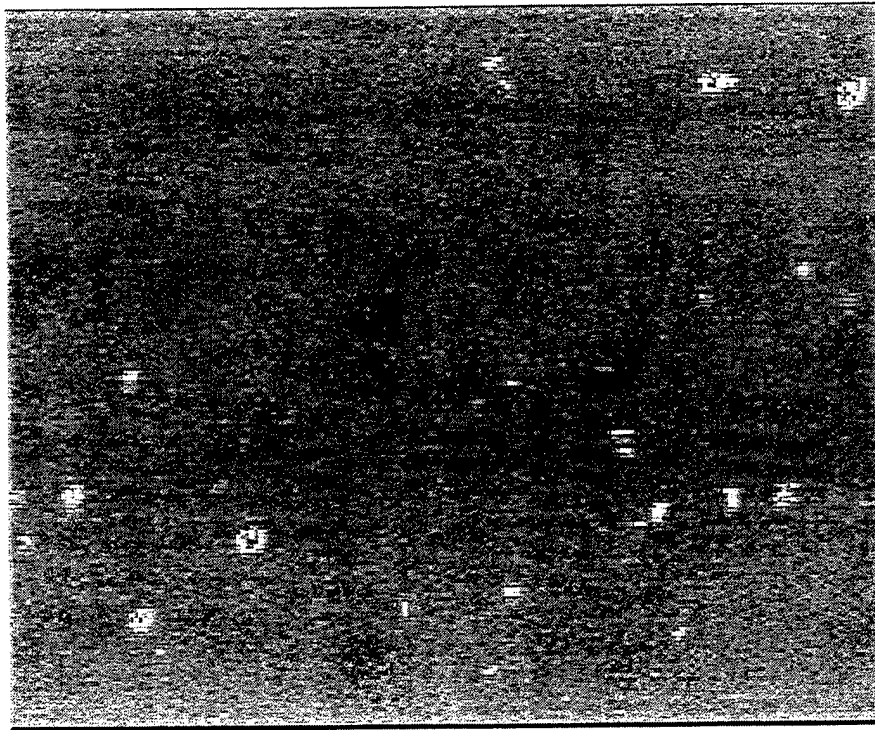
Figure 66 (a)   Thermal wave image of non-annealed ceramic

Figure 66 (b)   Thermal wave   image of annealed ceramic. Sensitivity
during this scan   was increased by a factor of 10 resulting in
more visible background signal changes. Relative amplitude
of signals from the peaks is substantially   decreased after
annealing.

5 μm would offer much better performance. Unfortunately, the experiments were terminated at this point due to lack of funding.

5.8   CONCLUSIONS

The photoacoustic method was proven to be sensitive enough to be used for quality control of silicon nitride ceramics. However, it was very difficult to shield extremely sensitive acoustic detector from external sources of noise. Relatively large level of external noise required long averaging time and data collection was slow. The long scanning time made impossible to acquire acoustic images of the samples, and only several of line scans were made.

The system based on infrared detection of thermal waves was found to be several orders of magnitude more sensitive than the photoacoustic system. Thermal wave linear scans as well as two-dimensional images of ceramic samples were made. These images have a very high signal to noise ratio and they demonstrated several μm resolution. We found that non annealed ceramics shows many small but very strong local inhomogeneities of thermal conductivity.

Data collected during the project demonstrated that infrared detection of thermal waves has many advantages over photoacoustic method. This includes simplicity, high sensitivity, low noise and high spatial resolution. The method is able to detect subsurface cracks with arbitrary orientation in respect to the surface, i.e. cracks which are parallel or perpendicular to the surface.

5.9   BIBLIOGRAPHY

1.   Zharov, V. P. and V. S. Letokhov, "Laser Optoacoustic Spectroscopy," Springer-Verlag, NY (1986) ibid p. 266.

2.   Solomon Musikant, "What Every Engineer Should Know About Ceramics," Marcel Dekker, NY (1991) ibid p. 133.

3.   Tam, A. C., "Ultrasensitive Laser Spectroscopy," edited by David S. Kliger, Academic Press, NY (1983) ibid p. 2.

4.   Tam, A C., "Ultrasensitive Laser Spectroscopy," edited by David S. Kliger, Academic Press, NY (1983) ibid p. 22.

5.   Rosencwaig, A., "Photoacoustics and Photoacoustic Spectroscopy," John Wiley and Sons, NY (1980) ibid p. 125.

6.   Pouch, J. J., R. L. Thomas, and Y. H. Wong, "Scanning optoacoustic microscopy for nondestructive evaluations," J. Opt. Soc. Am., 1980, 70, 562.

7.   White, R. M., "Generation of elastic waves by transient surface heating," J. Appl.8 Phys. (1963) 34, 3559

8.   Zharov, V. P., and V. S. Letokhov, "Laser Optoacoustic Spectroscopy," Springer-Verlag, NY (1986) ibid p. 267.

9.   Zharov, V. P., and V. S. Letokhov, "Laser Optoacoustic Spectroscopy," Springer-Verlag, NY (1986) ibid p. 268.

10.   Tam, A. C., "Ultrasensitive Laser Spectroscopy," edited by David S. Kliger, Academic Press, NY (1983) ibid p. 33-34.

11.   Patel, C. K. N., and A. C. Tam, "Optoacoustic spectroscopy of liquids", Appl. Phys. Lett., 34 (1979) 467.

12.   Wong, Y. H., R. L. Thomas, and J. J. Pouch, "Subsurface structures of solids by scanning photoacoustic microscopy," Appl. Phys. Lett., 35 (1979) 368.

13.   Waldrop, M. M, " Of politics, pulsars, death spirals, and LIGO," Science, 249 (1990) 1106.